Title
Collisions and Mergers in Dense Star Clusters

Author
Rose, Sanaea Cooper

Publication Date
2023

Peer reviewed|Thesis/dissertation

UNIVERSITY OF CALIFORNIA

Los Angeles

Collisions and Mergers in Dense Star Clusters

A dissertation submitted in partial satisfaction

of the requirements for the degree

Doctor of Philosophy in Astronomy & Astrophysics

by

Sanaea Cooper Rose

2023

ABSTRACT OF THE DISSERTATION

Collisions and Mergers in Dense Star Clusters

by

Sanaea Cooper Rose
Doctor of Philosophy in Astronomy & Astrophysics
University of California, Los Angeles, 2023
Professor Smadar Naoz, Chair

Almost every galaxy, including the Milky Way, has a supermassive black hole (SMBH) at its center. Surrounding these SMBHs are dense environments of stars and stellar relics. One consequence of this dense environment is that stars and stellar remnants frequently interact with one another. This dissertation examines how these interactions lead to unique populations of stars, binaries, and black holes. This work is undertaken in four studies, the first of which focuses on binary systems in the presence of a distant perturber. Most massive stars reside in triple systems or higher order multiples. Similarly, any binary system in the Galactic Center forms a triple system with the central SMBH. Any binary system that resides in the nuclear star cluster will be gravitationally perturbed by the SMBH, just as the tertiary star in a stellar triple will gravitationally perturb the two inner stars. These perturbations can alter the orbital parameters. In Rose et al. (2019), I examine the observational signatures of these gravitational interactions. Specifically, I show that the binary birth configurations are an excellent predictor of the final orbits; we can use observations of older stellar populations to learn about their birth conditions. Additionally, my work predicts that perturbations from the third body will cause many binaries to merge. However, binary

evolution in a star cluster is further complicated by the densely populated surroundings. In particular, interactions and collisions with surrounding objects can destroy binary systems. A surviving binary can therefore place a density constraint on its environment. I illustrate this procedure in Rose et al. (2020), showing that an observed binary has implications for the number of compact objects in its vicinity. Generally, the dynamics of a galactic nucleus means that binary systems become fewer over time, either due to third-body induced mergers or interactions with stars in the surrounding cluster, and singles should dominate an older population. Collisions, however, will continue to shape the population of singles, in particular by making more massive objects. Collisions between black holes (BHs) and stars, for example, represent a promising channel to form intermediate-mass BHs (Rose et al. 2022), while main-sequence stellar collisions can produce more massive, rejuvenated stars (Rose et al. 2023). The former may explain the origins of black holes above the maximum mass predicted by stellar evolution models: over many collisions with stars, the BH accretes enough material to grow appreciably in size.

The dissertation of Sanaea Cooper Rose is approved.

Tuan H. Do

Bradley M. Hansen

Tommaso L. Treu

Smadar Naoz, Committee Chair

University of California, Los Angeles

2023

To my parents

TABLE OF CONTENTS

LIST OF FIGURES

LIST OF TABLES

ACKNOWLEDGMENTS

Chapter 2 is a version of Rose et al. (2019), co-authored with Smadar Naoz and Aaron Geller and reproduced in this thesis with permission from MNRAS. Chapter 3 is a version of Rose et al. (2020), co-authored with Smadar Naoz, Abhimat Gautam, Andrea Ghez, Tuan Do, Devin Chu, and Eric Becklin and reproduced with the permission of the AAS and ApJ. Also included here with permission from the AAS, Chapters 4 and 5 are versions of Rose et al. (2022) and Rose et al. (2023), co-authored by Smadar Naoz, Re'em Sari, and Itai Linial.

My most heartfelt thanks to my advisor, Smadar Naoz, for her unwavering support, her patience, and her guidance. I could not have asked for a better advisor, or mentor. She represents to me the very best of her profession.

I am grateful to my thesis committee, Brad Hansen, Tuan Do, and Tommaso Treu, for their support and guidance. I am also grateful to Re'em Sari, Aaron Geller, Enrico Ramirez-Ruiz, and Alice Shapley for supporting the advancement of my career and for modeling scientific excellence and integrity.

I would never have made it this far without the support of my parents, Nazneen Cooper and Ronald Rose, who have been there for the best and worst days of my academic journey.

Charlie, thank you for your support, steadying presence, and all the crispy "smashed" potatoes.

To my classmates, Kelly, Ronald, Tony, and Veronica, there is no finer cohort, no group of friends I would have rather had at my side during six years of graduate school (and a pandemic). Bao Minh and Zhuo, thank you for your friendship and guidance over the years.

I am indebted to the many wonderful colleagues in my research group, including but not limited to Bao Minh Hoang, Isabel Angelo, Denyz Melchor, Alexander Stephan, Jesus Salas,

Yeou Chiou, Santiago Torres, Erez Michaely, and Brenna Mockler.

And lastly, to Licorice and Krystal, thank you for being the most wonderful feline companions a human could wish for. Licorice, wherever you may be, I hope it is filled with warm blankets and cans of tuna.

VITA

2017 **B.A., Astrophysics**, Wellesley College, MA

2019 **M.S., Astronomy**, UCLA, Los Angeles, CA

PUBLICATIONS

Tidal Disruption Events from the Combined Effects of Two-Body Relaxation and the Eccentric Kozai-Lidov Mechanism

Melchor, D., Mockler, B., Naoz, S., Rose, S.C., and Ramirez-Ruiz, E. Submitted to the Astrophysical Journal, 2023. arXiv:2306.05472

Stellar Collisions in the Galactic Center: Massive Stars, Collision Remnants, and Missing Red Giants

Rose, S.C., Naoz, S., Sari, R., and Linial, I. Accepted by the Astrophysical Journal, 2023. arXiv:2304.10569

Raining Rocks: An analytical formulation for collision timescales in planetary systems

Torres, S., Naoz, S., Li, G., and Rose, S.C. Accepted by the Monthly Notices of the Royal Astronomical Society, 2022, arXiv:2110.02269

Tidal disruption events from eccentric orbits and lessons learned from the noteworthy ASASSN-14ko

Liu, C., Mockler, B., Ramirez-Ruiz, E., Yarza, R., Law-Smith, J. A. P., Naoz, S., Melchor, D., and Rose, S.C. Astrophysical Journal, 2022, 944, 184-198.

The Formation of Intermediate Mass Black Holes in Galactic Nuclei

Rose, S.C., Naoz, S., Re'em, S., and Linial, I. Astrophysical Journal Letters, 2022, 929, L22, 1-9.

The Combined Effects of Two-Body Relaxation Processes and the Eccentric Kozai-Lidov Mechanism on the EMRI Rate

Naoz, S., Rose, S.C., Michaely, E., Melchor, D., Ramirez-Ruiz, E., and Mockler, B. Astrophysical Journal Letters, 2022, 927, L18, 1-11.

On Socially Distant Neighbors: Using Binaries to Constrain the Density of Objects in the Galactic Center

Rose, S.C., Naoz, S., Gautam, A.K., Ghez, A.M., Do, T., Chu, D., and Becklin, E. Astrophysical Journal, 2020, 904, 113-129.

Companion-driven Evolution of Massive Stellar Binaries

Rose, S.C., Naoz, S., and Geller, A.M. Monthly Notices of the Royal Astronomical Society, 2019, 488, 2480-2492.

A Three-Dimensional View of Turbulence: Constraints on Turbulent Motions in the HD 163296 Protoplanetary Disk Using DCO+

Flaherty, K.M., Hughes, A.M., Rose, S.C., et al. Astrophysical Journal, 2017, 843, 150-170.

CHAPTER 1

Introduction

Almost every galaxy harbors a 10^{6-9} $M_\odot$ supermassive black hole (SMBH) at its center (e.g., Ferrarese & Ford, 2005; Kormendy & Ho, 2013). The closest SMBH to Earth is the 4×10^6 $M_\odot$ Sagittarius A* at the center of the Milky Way Galaxy (e.g., Ghez et al., 2005; Gillessen et al., 2009). Surrounding the SMBH is a dense environment called the nuclear star cluster (e.g., Schödel et al., 2003; Ghez et al., 2005, 2008; Gillessen et al., 2009, 2017). One consequence of this dense environment is that stars and compact objects frequently interact with one another, particularly in the inner parsec region (e.g., Rose et al., 2020, 2022). The proximity of the Milky Way's galactic nucleus (GN) presents a unique opportunity to study the effects of these interactions on the cluster's population of stars and stellar remnants.

While the nuclear star cluster largely consists of older > 1 Gyr stars (Nogueras-Lara et al., 2019; Schödel et al., 2020; Chen et al., 2023), it also contains a younger $4 - 6$ Myr-old population (e.g., Lu et al., 2009; Bartko et al., 2010; Do et al., 2013a,b; Feldmeier-Krause et al., 2015). This population of young stars includes the S-star cluster, whose members have eccentric orbits that are distributed isotropically within ~ 0.04 pc of the SMBH (e.g., Schödel et al., 2003; Ghez et al., 2005, 2008; Gillessen et al., 2009, 2017). Additionally, this region contains a stellar disk structure (e.g., Levin & Beloborodov, 2003; Paumard et al., 2006; Lu et al., 2009; Bartko et al., 2009; Yelda et al., 2014). This unique environment, a stellar cluster embedded in the gravitational potential of a SMBH, leads to a number of interesting phenomena such as hypervelocity stars (e.g., Hills, 1988; Yu & Tremaine, 2003;

Ginsburg & Loeb, 2007), stellar binary mergers (e.g., Antonini et al., 2010, 2011; Prodan et al., 2015; Stephan et al., 2016, 2019), and compact object mergers (Hoang et al., 2018; Wang et al., 2021), phenomena which require the existence of a binary population in the GN.

Stars often reside in a binary configuration (e.g., Raghavan et al., 2010). Already, three confirmed binaries have been observed in the GN. With a period of 19.5 days and a total mass of $100\,M_{\odot}$, the binary IRS 16SW resides at approximately 0.05 pc from the SMBH (Ott et al., 1999; Martins et al., 2006). The other confirmed binaries, presented by Pfuhl et al. (2014), are a short-period (2.3 days) eclipsing Wolf-Rayet system and a long-period (224 days) low eccentricity ($e = 0.3$) system at 0.1 pc from the SMBH. Additionally, Dong et al. (2017a) and Dong et al. (2017b) find 10 binaries in the inner pc region of the GN, with other studies suggest the GN's OB binary fraction is comparable to that in young massive stellar clusters (e.g., Ott et al., 1999; Rafelski et al., 2007; Gautam et al., 2019). The theoretical study Stephan et al. (2016) suggests that the binary fraction of the 6 Myr-old stellar population may be as high as 70%. Other indirect forms of evidence for a binary population include X-ray sources in inner parsec (Muno et al., 2005, 2006, 2009; Heinke et al., 2008; Cheng et al., 2018; Zhu et al., 2018; Hailey et al., 2018); hypervelocity stars from binaries disrupted by the SMBH (e.g., Hills, 1988; Yu & Tremaine, 2003; Ginsburg & Loeb, 2007; Perets, 2009a,b); and peculiar properties of the stellar disk (Naoz et al., 2018). Altogether, these observational and theoretical studies provide strong evidence for the presence of binaries in the GN. The evolution of these systems will be influenced by the surrounding environment, a dense star cluster with a massive central object.

Any binary system in the GN forms a triple system with the resident SMBH. These triples are hierarchical in nature: the outer orbit, defined to include the SMBH and the binary system, is much wider than the orbit of the stellar binary, referred to as the inner orbit. In this configuration, coherent gravitational perturbations from the outer body influence

the long-term evolution of the inner orbit. In particular, these perturbations cause the orbital eccentricity and inclination to oscillate in time, a dynamical process known as the Eccentric Kozai-Lidov (EKL) Mechanism (e.g., Naoz, 2016). This secular process, the EKL Mechanism, has three possible outcomes.

Firstly, perturbations from the third body can drive the inner binary eccentricity to large values, decreasing the periapsis. During this close approach, tides can act to tighten and circularize the inner binary orbit (e.g., Naoz & Fabrycky, 2014; Rose et al., 2019). On the other hand, the perturbations may drive the eccentricity to extreme values before tides can act, causing the inner binary to merge (e.g., Antonini & Perets, 2012; Naoz & Fabrycky, 2014; Stephan et al., 2016; Hoang et al., 2018; Rose et al., 2019; Fragione & Antonini, 2019). In the final case, the system may simply undergo weak eccentricity oscillations (e.g., Rose et al., 2019).

Hierarchically configured triples have a variety of applications to astrophysical phenomena. Triple dynamics provide a key formation channel for blue-stragglers (e.g., Perets & Fabrycky, 2009; Naoz & Fabrycky, 2014; Fragione, 2019). Furthermore, hierarchical triple dynamics leads to many short period compact object binaries, including black hole, neutron star, and white dwarf binaries (Thompson, 2011; Katz & Dong, 2012; Antonini & Perets, 2012; Naoz et al., 2016; Toonen et al., 2018; Hoang et al., 2018; Fragione & Loeb, 2019). The evolution of binaries with a distant companion is essential to understanding compact object mergers, via gravitational wave (GW) emission, within a GN (Antonini & Perets, 2012; Prodan et al., 2015; Fragione et al., 2018; Fragione, 2019; Stephan et al., 2016, 2019; Hoang et al., 2018, 2019). In Rose et al. (2019), adapted in Chapter 2 of this thesis, I examine the dynamical evolution of binary systems in the presence of a distant perturber, relevant to both triple systems in young stellar clusters and binaries in a GN. The presence of a nuclear star cluster, however, further complicates the dynamical evolution of binaries in the vicinity of a SMBH.

A binary system in the nuclear star cluster experiences frequent weak perturbations from

passing objects. Generally, the long-term effects of these interactions depend on the gravitational binding energy of the binary compared to the energy of its environment. The term soft binary refers to a system that is loosely bound compared to the average kinetic energy of the neighboring objects. Soft binaries widen over time due to weak interactions with passing objects (e.g., Heggie, 1975; Hills, 1975). Over the so-called evaporation timescale, these interactions eventually unbind the binary (see the derivation in Binney & Tremaine, 2008). This timescale depends on several parameters, including the velocity dispersion, density of objects, and binary semimajor axis. Additionally, a star in the binary can collide with a passing object (e.g., Sigurdsson & Phinney, 1993; Fregeau et al., 2004). The timescale for a direct collision also depends on the density of the system's environment (e.g., Binney & Tremaine, 2008; Kocsis & Tremaine, 2011). A direct collision merges the two objects involved, and it may also unbind the binary system if the incoming object has sufficient kinetic energy (e.g., Sigurdsson & Phinney, 1993; Fregeau et al., 2004). Rose et al. (2020) explore the implications of these processes for the binary population. I show that certain binary configurations are favored in an old population because of these destructive processes. I also demonstrate that a confirmed binary can be used to probe the density of objects in its vicinity.

The dynamical processes discussed above reduce the cluster's binary population over time, either by merging the systems or unbinding them. As a result, single objects should dominate an old population. However, dynamical processes will continue to shape the population of singles. In one such process, any object orbiting the SMBH will experience frequent weak gravitational interactions with other passing objects. Over time, the effects of these interactions accumulate, changing the orbit of the object about the SMBH. Known as two-body relaxation, this process occurs over an associated timescale, which is the time needed for the orbital energy to change by order of itself (e.g., Binney & Tremaine, 2008). Crucially, by changing the orbital semimajor axis and eccentricity, relaxation processes can cause objects to wander too close to the SMBH (e.g., Hopman & Alexander, 2005, 2006b; Alexander & Hopman, 2009; Preto & Amaro-Seoane, 2010; Amaro-Seoane & Preto, 2011; Aharon &

Perets, 2016; Amaro-Seoane, 2018; Chen & Han, 2018; Sari & Fragione, 2019; Naoz et al., 2022). If the object in question is a star, it will be tidally disrupted by the SMBH, producing an electromagnetic signature (e.g., Rees, 1988). If the object is instead a compact object, GW emission will cause it to spiral into the SMBH, an event detectable by future space-based GW observatories (e.g., Amaro-Seoane et al., 2017; Robson et al., 2019; Baker et al., 2019; Mei et al., 2020). The relaxation process, along with SMBH-induced compact object binary mergers, makes the GN a factory for extreme events.

Recent technological advances have launched us into a new era of GW detection. The Laser Interferometer Gravitational-wave Observatory (LIGO) and Virgo Interferometer have already detected a number of compact object mergers. These early observations are challenging our previous understanding of compact object formation. Above a certain mass, a star is expected to end its life in such a violent supernova that no compact object remains. Therefore, most stellar evolution models predict a gap in black hole (BH) masses from approximately 50 to 150 $M_\odot$, known as the pair-instability or upper mass gap (e.g., Heger et al., 2003; Woosley, 2017) . GW detections, however, indicate the existence of BHs in this mass range (e.g., Fishbach et al., 2020). Most notably, LIGO detected GWs from a BH-BH merger with 85 $M_\odot$ and 66 $M_\odot$ progenitors, yielding an intermediate mass black hole (IMBH) of approximately 142 $M_\odot$ (The LIGO Scientific Collaboration et al., 2020a,b). The origins of these BHs remain uncertain. The dynamic environment at the center of our galaxy offers possible explanations for their formation. I propose one such formation channel in Rose et al. (2022), in which I explore whether repeated collisions between stellar mass BHs and stars can produce IMBHs.

The stellar density in the GN, specifically within 0.1 pc of the SMBH, is high enough that direct collisions can occur between objects. Collisions have been invoked to explain the observed deficit of red giants in the GN (e.g. Bailey & Davies, 1999; Dale et al., 2009; Mastrobuono-Battisti et al., 2021), and they may also produce blue stragglers (e.g., Sills

et al., 2001, 1997; Lombardi et al., 2002) and drive AGN variability (e.g., Murphy et al., 1991; Freitag & Benz, 2002). Leveraging the models developed by Rose et al. (2022), I undertake a study of main-sequence stellar collisions in Rose et al. (2023) and comment on their outcomes and implications for various observational puzzles in the Milky Way's GN. Additionally, I show that collisions can change the masses and demographics of the stellar population within 0.1 pc of the SMBH.

This thesis is organized as follows. Chapter 2 presents Rose et al. (2019), a study on companion-driven evolution of binary systems. In Chapter 3, I reproduce my paper, Rose et al. (2020), which considers the effects of a stellar cluster on binary outcomes. In Chapters 4 and 5, I present results from Rose et al. (2022) and Rose et al. (2023) on BH-star collisions and main-sequence stellar collisions, respectively, and their implications for GN populations. Chapter 6 summarizes my results.

CHAPTER 2

Companion-Driven Evolution of Massive Stellar Binaries

At least 70% of massive OBA-type stars reside in binary or higher-order systems. The dynamical evolution of these systems can lend insight into the origins of extreme phenomena such as X-ray binaries and gravitational wave sources. In one such dynamical process, the Eccentric Kozai-Lidov Mechanism, a third companion star alters the secular evolution of a binary system. For dynamical stability, these triple systems must have a hierarchical configuration. We explore the effects of a distant third companion's gravitational perturbations on a massive binary's orbital configuration before significant stellar evolution has taken place ($\leq$ 10 Myr). We include tidal dissipation and general relativistic precession. With large ($38,000$ total) Monte-Carlo realizations of massive hierarchical triples, we characterize imprints of the birth conditions on the final orbital distributions. Specifically, we find that the final eccentricity distribution over the range $0.1 - 0.7$ is an excellent indicator of its birth distribution. Furthermore, we find that the period distributions have a similar mapping for wide orbits. Finally, we demonstrate that the observed period distribution for approximately 10 Myr-old massive stars is consistent with EKL evolution.

2.1 Introduction

Recent observations suggest that massive stellar binaries are prevalent in our Galaxy. In fact, more than 70% of OBA and 50% of KGF spectral type stars likely exist in binaries (e.g., Tokovinin, 2008; Raghavan et al., 2010; Sana et al., 2012). Observations of massive binaries

suggest unique orbital parameter distributions compared to KGF binaries. For example, Duchêne & Kraus (2013) estimate that 30% of massive stellar binaries have periods less than ten days, while some power law can represent the slow decline in the number of systems out to about 10^4 AU. Sana et al. (2012) also find that the period distribution of OBA stars increases dramatically toward smaller periods. These findings contrast with those for KGF stars, which populate a log-normal period distribution peaked around 10^5 days (Raghavan et al., 2010). While the period distributions for these spectral types differ, the eccentricity distribution of OBA stars may be closer to that of the KGF stars. See Section 2.3.5 for a more detailed discussion.

Many short period KGF binaries may in fact occur in a triple configuration (Tokovinin, 1997; Pribulla & Rucinski, 2006; Tokovinin, 2008; Moe & Di Stefano, 2017; Eggleton et al., 2007; Griffin, 2012). Similarly, massive binaries may often reside in triple configurations (Raghavan et al., 2010; Zinnecker & Yorke, 2007). While the fraction of massive stars in triples is not well known, the average number of companions per OB primary may be at least three times higher than that of low-mass stars, which have 0.5 companions on average (Preibisch et al., 2001; Grellmann et al., 2013).

Dynamical stability arguments imply that these triple systems must have a hierarchical configuration: the third body orbits the inner binary on a much wider outer orbit. In this configuration, coherent gravitational perturbations from the outer body influence the long-term evolution of the inner orbit. The orbits can be treated as massive wires that torque each other, where the line-density of each wire is inversely proportional to the orbital velocity. In this orbit-averaged, or secular, approximation, the semi-major axis ratio remains constant. The gravitational potential can be expanded in terms of this ratio a_1/a_2, where a_1 ($a2$) is the semi-major axis of the inner (outer) orbit (Kozai, 1962; Lidov, 1962). The hierarchical configuration makes this expansion possible by ensuring that a_1/a_2 is a small parameter. The lowest order, or quadrupole level, of approximation is proportional to $(a_1/a_2)^2$. The

next level of approximation is called the octupole level (see Naoz, 2016, a recent review).

The applications of hierarchically configured stellar triples have been explored extensively in the literature (Naoz & Fabrycky, 2014; Harrington, 1969; Mazeh & Shaham, 1979; Kiseleva et al., 1998; Fabrycky & Tremaine, 2007; Perets & Fabrycky, 2009; Thompson, 2011; Naoz et al., 2013a; Shappee & Thompson, 2013; Pejcha et al., 2013; Michaely & Perets, 2014; Prodan et al., 2015; Stephan et al., 2016; Moe & Kratter, 2018; Bataille et al., 2018). Furthermore, many studies suggest that short period compact object binaries, including black hole, neutron star, and white dwarf binaries, may result from hierarchical triple dynamics (Thompson, 2011; Katz & Dong, 2012; Antonini & Perets, 2012; Naoz et al., 2016; Toonen et al., 2018; Hoang et al., 2018). We examine the impact of EKL-driven dynamical evolution on the properties of massive binaries embedded in triples. The birth orbital configurations of massive binaries are not well constrained. We therefore explore different possibilities for the period and eccentricity birth distributions with the objective of discerning the birth properties from the final results. We test a broad range of initial distributions, tidal recipes, and efficiencies to identify the manner in which observed period and eccentricity distributions map back onto the initial distributions. We focus on 10 Myr old systems, i.e., before significant stellar evolution has taken place. Our simulations include tidal dissipation and general relativistic precession.

We run 38 sets of Monte-Carlo numerical simulations with a variety of initial conditions and tidal recipes. Each simulation has 1000 systems, bringing the total number of realizations to $38,000$. Section 2.2 reviews our methods and initial conditions. In Section 2.3, we present our results and analyze the statistical distributions of the inner orbital periods and eccentricities. Section 2.3.4 investigates traces of the initial conditions in the final distributions, traces which persist even after 10 Myr of EKL-driven evolution. Finally, we consider our simulated results in the context of observations and discuss the implications in Section 2.3.5. Our simulations suggest that the EKL mechanism can re-distribute the orbital periods to match observed

distributions, while the eccentricity distribution retains its original shape.

2.2 Methodology, Numerical Setup and Initial Conditions

2.2.1 Point mass dynamics

We solve the secular equations of motion for the hierarchical triple to the octupole-level of approximation, as described in Naoz et al. (2013a). Stars with masses m_1 and m_2 compose the inner binary, while the tertiary body with mass m_3 and the inner binary form an outer binary. The inner (outer) orbit has the following parameters: a_1 (a_2), e_1 (e_2), ω_1 (ω_2) and i_1 (i_2) for the semimajor axis, eccentricity, argument of periapsis, and inclination with respect to the total angular momentum, respectively. We define i_{tot} as $i_1 + i_2$. We include general relativistic precession following Naoz et al. (2013b), who demonstrate that GR precession can suppress or facilitate eccentricity excitations in different parts of phase space.

We limit our simulations to 10 million years to allow for comparisons with observed massive stars in young stellar clusters (e.g., Sana et al., 2012). We treat the mass and radius of each star as constant. Over ten million years, a 20 $M_\odot$ star, the largest mass allowed in these simulations, will lose about three percent of its mass, and the semi-major axis of its orbit will expand by three percent. Thus, while the interplay between the point-mass dynamics and stellar evolution has interesting consequences (e.g., Stephan et al., 2016), it has negligible effect on our calculations.

2.2.2 Tidal models

We include tidal dissipation, which acts to circularize and tighten the inner binary. Following Naoz & Fabrycky (2014), we adopt the tidal evolution equations of Eggleton & Kiseleva-Eggleton (2001). These equations follow the equilibrium (E) tide model of Eggleton et al. (1998). Eggleton & Kiseleva-Eggleton (2001) relate the viscous timescale t_v of a star to the tidal dissipation timescale t_F using the Love parameter $k_{L,j}$, where $j = 1, 2$ for masses m_1

and m_2, respectively. The Love parameter quantifies the quadrupolar deformability of a star. For the primary star with mass m_1,

$$t_{F,1} = t_{v,1} \left(\frac{a_1}{R_1} \right)^8 \frac{m_1^2}{m_2(m_1 + m_2)} \frac{1}{9(1 + 2k_{L1})^2} \ . \tag{2.1}$$

We use $k_{L,j} = 0.014$ for an $n = 3$ polytrope (Eggleton & Kiseleva-Eggleton, 2001). Both the primary and secondary stars have spin periods of four days. Based on Bouvier (2013), the spin period of a massive star is approximately two days. A factor of two has minimal impact in these tidal prescriptions: The system in the right-hand panel of Figure 2.4 exhibits the same behavior if we set the stellar spins to two days instead of four.

We also implement a prescription for radiatively-damped dynamical (RDD) tides (Zahn, 1977) for stars of mass greater than 1.5 $M_\odot$. Following Hurley et al. (2002) and Zahn (1977), we express the tidal dissipation timescale as:

$$\begin{aligned} t_F &= \left(\frac{a_1}{R_1} \right)^9 \sqrt{\frac{a_1^3}{G m_1}} \frac{m_1}{m_2} \left(1 + \frac{m_2}{m_1} \right)^{11/6} \\ &\times \frac{1}{9(1.592 \times 10^{-9})} \left(\frac{m_1}{M_\odot} \right)^{2.84} . \end{aligned} \tag{2.2}$$

We note that in a comparison with numerical calculations, Chernov (2017) suggests that this tidal prescription underpredicts the tidal efficiency in short period binaries. Claret & Cunha (1997) find that Zahn's formalism fails to account for some observed circularized systems. The treatment of stellar tides has invoked much debate (Langer, 2009). Noting this lack of accord, Yoon et al. (2010) include a parameter for the rate of tidal synchronization to test for its effects. Similarly, we opt to use the equilibrium tide model for all stars in select simulations, allowing us to treat the viscous timescale as a free parameter and tune the tidal efficiency.

We label our simulations according to tidal prescription and efficiency as detailed in Table 2.1. Both Hurley et al. (2002) and Zahn (1977) note the inefficient nature of RDD tides compared to E tides. We use E tides with $t_v = 0.005$, an unrealistically small value, in a few simulations for comparative purposes.

Table 2.1: Simulations are named according to tidal prescription and efficiency. In IET and LET simulations, RDD tides are used for stars with masses greater than $1.5M_{\odot}$, while E tides with the specified t_v are used for lower mass stars.

Label: Name	Tidal Prescription
LET: Least Efficient Tides	RDD or E $t_v = 50$ yr
IET: Inefficient Tides	RDD or E $t_v = 0.5$ yr
MET: Moderately Efficient Tides	E $t_v = 50$ yr
SET: Super Efficient Tides	E $t_v = 0.5$ yr
UET: Unrealistically Efficient Tides	E $t_v = 0.005$ yr

2.2.3 Birth Distributions

To explore the influence of initial parameter distributions on the results, we use several different probability distributions to draw initial conditions for the Monte Carlo simulations. We label simulations according to their birth distributions.

The simulations fix the mass of the primary m_1 at 10 $M_{\odot}$. We then draw m_2 and m_3 from uniform distributions of the mass ratios $q_1 = m_2/m_1$ and $q_2 = m_3/(m_1 + m_2)$ where $0.1 < q < 1$. We discuss simulations that use a Kroupa mass function in Appendix 2.5.1. A power law of the form $R \propto M^{\alpha}$ derives the stellar radii from the masses. For most simulations, we use the ZAMS mass-radius relation $R = 1.01M^{0.57}$[1]. In all simulations, we include a spin-orbit misalignment for the primary (secondary) star β_1 (β_2), which we draw from an isotropic distribution.

Observations of young ($\sim$ few Myrs old) massive clusters suggest power law distributions for period and eccentricity (with different indices). The most conservative choice of initial conditions assumes that the final distributions remain unchanged from the birth distributions.

[1]For comparison purposes, below, we also consider larger radii using $R = 1.33M^{0.55}$, an empirical fit to observations, and $R = 1.61M^{0.81}$, the TAMS mass-radius relation (Demircan & Kahraman, 1991).

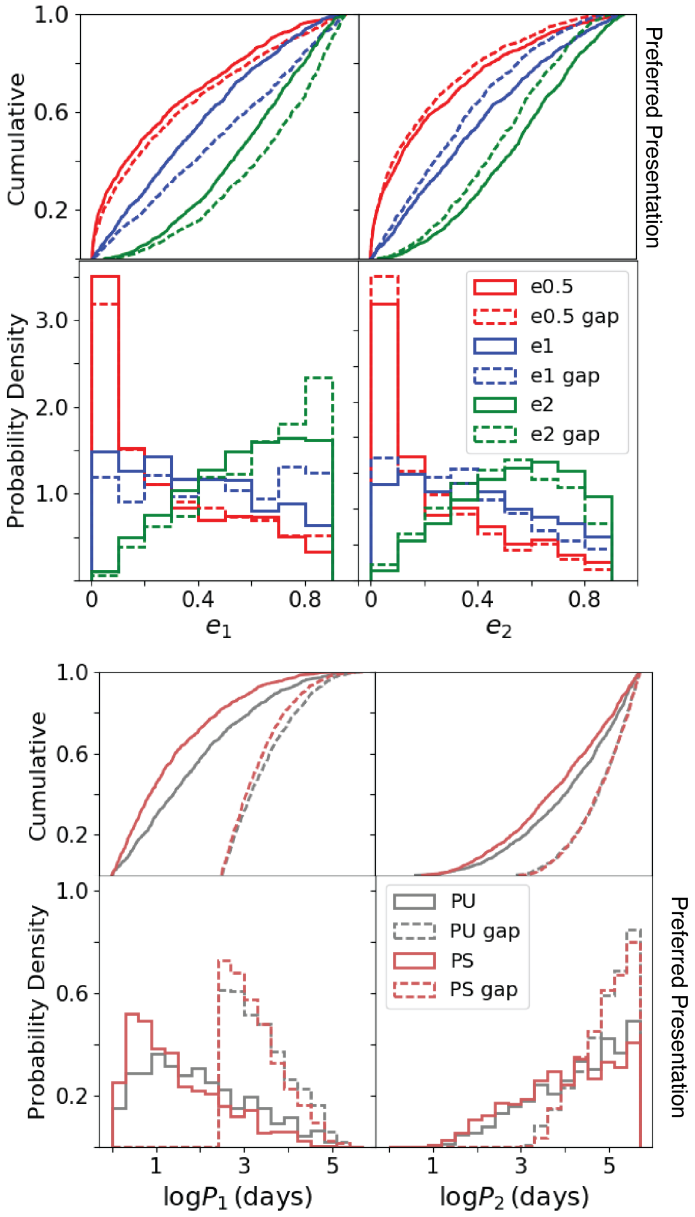

Figure 2.1: The possible initial conditions for period and eccentricity. **Top panel:** Cumulative eccentricity distribution **Second panel:** Eccentricity probability density **Third panel:** Cumulative period distribution **Fourth panel:** Period probability density. We consider the initial distributions after applying stability criteria (see text). Initial conditions with a gap are represented by dashed lines. In the top two panels, thermal, uniform, and $\sim e^{-0.5}$ are shown in green, blue, and red, respectively. Note that those simulations with no gap have fewer high eccentricity systems, a result of having smaller values of a_{1i} while still needing to satisfy the Roche limit criterion. In the bottom panels, we show a uniform distribution in logarithmic period (grey lines) and $f(\log P/\text{days}) \propto (\log P/\text{days})^{-0.5}$ (crimson lines) (Sana et al., 2012, 2013). Since the stability criteria tend to curtail large values of a_1, the PU and PS gap distributions appear similar. We observe a similar albeit less pronounced effect in the distributions without a gap (solid lines).

The most agnostic choice of initial conditions assumes uniform distributions for period and eccentricity. Overall, we test six birth distribution combinations of eccentricity and period. Below, the abbreviation for each initial condition is given in parentheses. We use these abbreviations in the simulation labels.

We use three possible initial distributions for eccentricity. For populations of massive stars, observations indicate that the probability density distribution is either $f(e) \propto e^{-0.5}$ ("e05") (e.g., Sana et al., 2012; Sana & Evans, 2011) or uniform ("e1") (e.g., Almeida et al., 2017). We supplement these simulations with ones that assume a thermal eccentricity distribution ("e2").

For the period distribution, we adopt a probability density of the form $f(\log P/\text{days}) \propto (\log P/\text{days})^{-0.5}$ ("PS") (e.g., Sana et al., 2012). Since this observed probability density does not necessarily represent the birth distribution, we also use a uniform distribution in logarithmic space ("PU") for certain simulations. Additionally, Sana et al. (2017) present observations of eleven young (< 1 Myr) massive binaries in the open cluster M17 with a low radial-velocity dispersion. They offer multiple explanations for the peculiar velocity dispersion. In one of these explanations, the massive binaries form at larger periods, with some minimum birth separation, and later tighten and circularize. Specifically, Sana et al. (2017) suggest that a lower period cutoff of nine months is consistent with the velocity dispersion in M17 within 1σ. To explore this intriguing possibility, we include a lower period cutoff of nine months in multiple ("gap") simulations.

2.2.4 Stability Criteria

To ensure that the secular approximation is valid, we apply three criteria to the initial conditions (Naoz & Fabrycky, 2014). The Mardling & Aarseth (2001) criterion ensures the long-term stability of the system, where i_{tot} denotes the mutual inclination between the inner

and outer orbits in radians:

$$\frac{a_2}{a_1} > 2.8\left(1+\frac{m_3}{m_1+m_2}\right)^{2/5}\frac{(1+e_2)^{2/5}}{(1-e_2)^{6/5}}\left(1-0.3i_{tot}\right) \tag{2.3}$$

We note that this stability criterion does not consider the system's lifetime (see, for example, Mylläri et al., 2018) and therefore under-predicts the number of systems that may undergo EKL oscillations during the 10 Myr integration time.

The second criterion compares the amplitudes of the octupole and quadrupole terms to verify that the perturber is weak, i.e. that higher order terms have a negligible effect. This criterion stipulates that ϵ, the ratio of the octupole and quadrupole amplitudes, remains small:

$$\epsilon = \frac{a_1}{a_2}\frac{e_2}{1-e_2^2} < 0.1 \ , \tag{2.4}$$

The last criterion requires that the inner orbit falls outside the Roche limit to avoid an early merger, before secular effects occur. We use the Roche limit as defined by Eggleton (1983):

$$L_{R,ij} = 0.49\frac{(m_i/m_j)^{2/3}}{0.6(m_i/m_j)^{2/3}+\ln(1+(m_i/m_j)^{1/3})} \ , \tag{2.5}$$

where $j = 1, 2$ and R_i denotes stellar radius. All of our systems begin with $a_1(1-e_1)L_{R,ij} > R_i$.

The stability criteria affect the simulated birth distributions. In Figure 2.1, this effect is most apparent in the thermal eccentricity distribution with no gap. The lack of a gap allows small values of a_1. Given the greater abundance of small semi-major axes, the Roche limit criterion limits the number of high eccentricity systems. Similarly, the requirement that a_1 be small compared to a_2 for a hierarchical triple, a condition reinforced by Eq. 2.3 and 3.31, curtails the number of inner binaries at large periods (Figure 2.1). Due to this effect, the PU and PS gap period distributions strongly resemble each other, and the no-gap PU and PS distributions converge at large periods.

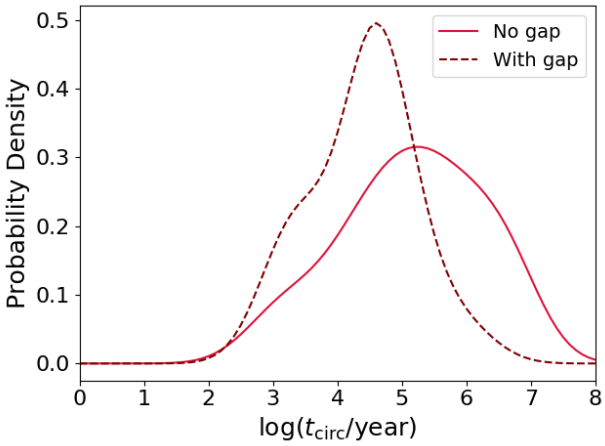

Figure 2.2: **Circularization timescales:** SET-PU-e1 (solid bright red curve) and SET-PS-e1-gap (dashed maroon curve) smoothed histograms of the circularization time ($t_{\rm circ}$), defined by our stopping condition, using a Guassian kernel density estimator. The no-gap simulation has an order of magnitude more circularized systems.

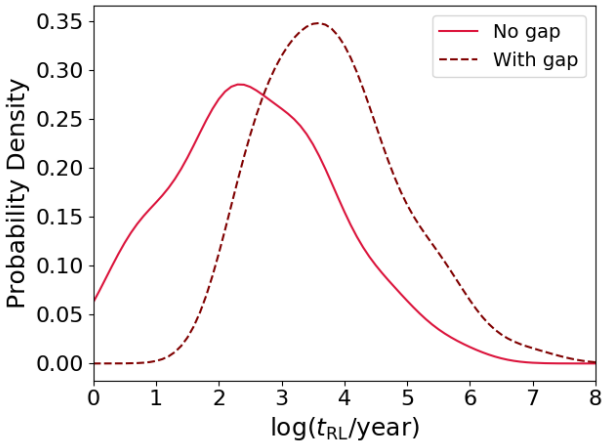

Figure 2.3: **RL-crossing timescales:** Smoothed histogram of the Roche Limit crossing time, called $t_{\rm RL}$, using a Guassian kernel density estimator for SET-PU-e1 (solid bright red curve) and SET-PS-e1-gap (dashed maroon curve). We term these systems RL binaries.

2.2.5 Stopping Conditions

We evolve each triple system for 10 Myr. We also include conditions which, if met, result in an early termination of the integration. We consider two stopping conditions:

- We terminate the simulation once the system tightens and circularizes because tide-dominated systems become numerically expensive. We consider a system to be tidally tightened and circularized when $a_1 < 2.1 R_{i,j}/L_{R,ij}$ and $e_1 < 0.001$. Figure 2.2 shows the typical circularization timescales for gap and no-gap systems.

- If an inner member have crosses the other's Roche limit, i.e., $a_1(1-e_1)L_{R,ij} < R_i$, see Eq. 3.32, we terminate the integration. We denote the time upon which the system crosses the Roche limit as t_{RL}. In Figure 2.3, we show typical t_{RL}. As expected, the gap systems have systematically longer Roche limit crossing times because they are associated with longer quadrupole timescales. The quadrupole timescale T_{quad} depends on P_2^2/P_1, where P_1 (P_2) correspond to the inner (outer) orbital period. Typical gap systems have $\log T_{quad} > 3.5$ with a median $\log T_{quad} \sim 6.7$. While the no-gap distribution has a similar median ($\log T_{quad} \sim 6.8$), the distribution is wider and has more systems with low quadrupole timescales. The lower limit of the distribution shifts to a shorter timescale, $\log T_{quad} > 1.5$.

  Unlike Naoz & Fabrycky (2014), we do not count these systems as merged products because we expect their merger times to be a few million years (Stephan et al., 2016), the same order as the stellar evolution timescale. The outcome of this interaction remains highly uncertain without comprehensive eccentric binary interaction physics. During this process, the stars may or may not be observed as two distinct stars. Thus, to differentiate these systems, we term them Roche limit-crossed binaries, or RL binaries for brevity.

  During a mass transfer process complicated by forced eccentricity oscillations from the

tertiary, an observer may detect m_1 and m_2 as a binary system. We therefore define a possible observed orbit for the RL binaries with $a_{\rm F} \sim R_{\rm RL}$ by assuming angular momentum conservation, a plausible assumption during the final plunge of the merger. We also artificially set the eccentricities of RL binaries to 0.01, which may inflate the number of circularized systems. We caution that the true properties of these systems are highly uncertain, and the actual observed periods may vary largely. In Figure 2.7, we denote this uncertainty with arrows.

2.3 Simulated Results

2.3.1 General outcomes

Each system has three possible general outcomes, shown in Figure 2.4. The final outcome depends mainly on the eccentricity excitations and the efficiency of the tides, which act to tighten and circularize the inner orbit. The "strength" of the EKL mechanism, parameterized by ϵ (Eq. 3.31), combined with the mutual inclination i_{tot} of the system determine the nature of the eccentricity excitations (e.g., Naoz, 2016).

- **Roche Limit (RL) crossing** When extreme eccentricity excitations occur on a shorter timescale than the tidal forces can circularize the system, the pericenter approach can become smaller than the Roche-limit (Eq. 3.32). This type of behavior is depicted in the left hand side of Figure 2.4. This outcome is common in the weak-tide regime examined in this paper.

- **Tidal tightening and circularization** During periods of higher eccentricity induced by the third star, tidal forces can act to shrink and circularize the inner orbit. The tidal forces decrease the inner semi-major axis until the inner orbit decouples from the third star. The decoupling of the outer and inner orbits results in a conservation of their individual angular momenta. As a result, the typical final semi-major axis of the

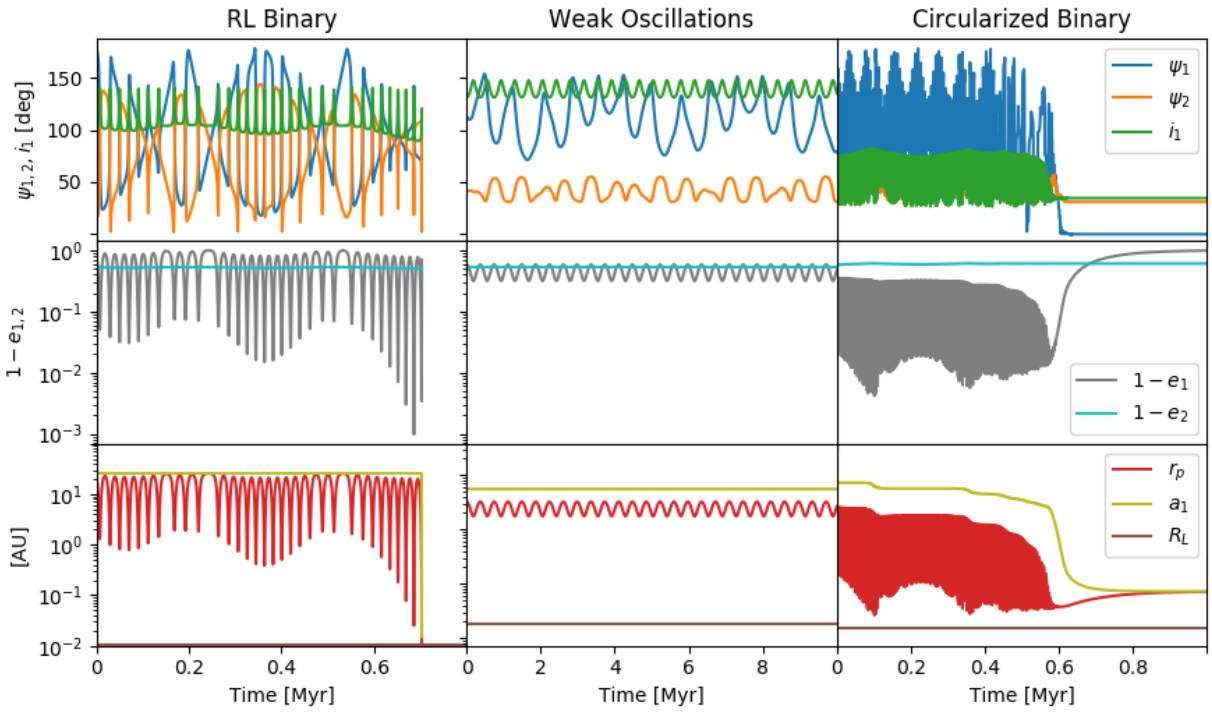

Figure 2.4: **Archetypal systems:** Here we show the time evolution of three triple systems. The left, middle, and right columns represent a Roche-limit crossing system, a system that undergoes weak oscillations, and a tidally circularized system, respectively. The first row shows the inner binary orbital inclination (blue) and obliquities (orange, green) of the stars; the second row, eccentricities of the inner and outer binary; and the last row, the inner semi-major axis, periapsis, and the Roche limit. Note that in the tidally tightened and circularized system, r_p and a_1 converge while e_1 approaches zero. Both simulations take a 10 $M_\odot$ primary. The left-hand side has initial values $m_2 = 2.1\ M_\odot$, $m_3 = 11.7\ M_\odot$, $a_1 = 25.8$ AU, $a_2 = 286.7$ AU, $e_1 = 0.22$, $e_2 = 0.47$, $\beta_1 = 178°$, $\beta_2 = 33°$, $i_1 = 104°$, and $i_2 = 4°$; the middle panel, $m_2 = 9.6\ M_\odot$, $m_3 = 8.3\ M_\odot$, $a_1 = 5.5$ AU, $a_2 = 327.4$ AU, $e_1 = 0.42$, $e_2 = 0.47$, $\beta_1 = 1.7°$, $\beta_2 = 208°$, $i_1 = 131°$, and $i_2 = 4.07°$; and the right-hand side, $m_2 = 6.0\ M_\odot$, $m_3 = 12.6\ M_\odot$, $a_1 = 7.2$ AU, $a_2 = 85.8$ AU, $e_1 = 0.77$, $e_2 = 0.42$, $\beta_1 = 44°$, $\beta_2 = 49°$, $i_1 = 71°$, and $i_2 = 4°$.

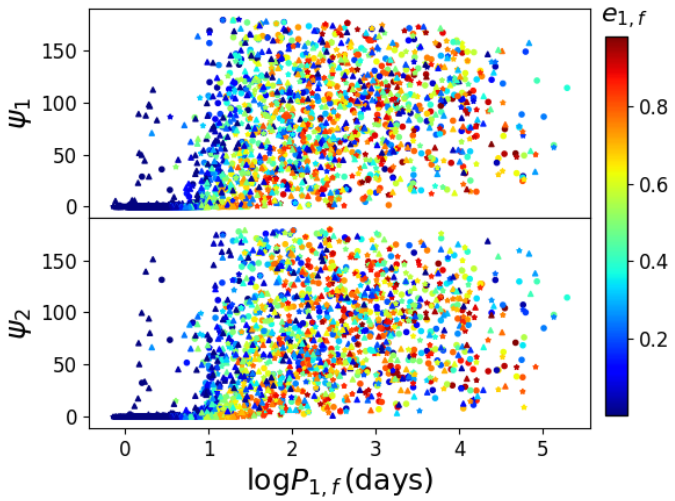

Figure 2.5: **Spin-orbit angle:** The final spin-orbit angle and period for both the primary (top) and secondary (bottom) colored by final eccentricity. Circles represent systems from MET-PU-e1, stars from MET-PU-e2, and triangles from MET-PS-e05. The points at low eccentricity and period but non-zero spin-orbit angles represent Cassini resonances.

inner orbit is $\sim 2a_{1,0}(1-e_{1,0})$, where the subscript "0" denotes initial values. The right column of Figure 2.4 shows an example of this evolution.

Tidal dissipation also tends to align the spin axes of the stars with the inner orbit's angular momentum vector. The spin-orbit angle ψ_1 (ψ_2) is defined as the angle between the inner orbit's angular momentum and the spin axis of m_1 (m_2). Figure 2.5 shows that this angle goes to zero in most systems. However, in some cases, the system can become locked into a resonance, called a Cassini resonance:

$$\Omega_j = 2\frac{2\pi/P_1}{\cos\phi_j + \sec\phi_j}\ , \tag{2.6}$$

where ϕ_j denotes the spin-orbit angle and Ω_j, the spin period of the two stars ($j = 1, 2$) in the inner orbit (e.g., Fabrycky et al., 2007; Stephan et al., 2016; Naoz & Fabrycky, 2014).

- **Weak oscillations** In many cases, the third star induces only weak eccentricity and inclination oscillations that do not result in a dramatic change of the orbital parameters. The middle column of Figure 2.4 shows an example system. While the locations of these

individual systems in the eccentricity distribution shift slightly, they do not introduce a noticeable net change.

2.3.2 Eccentricity distribution and the effect of tides

The final eccentricity distribution tends to retain the same shape and curvature as the birth distribution irrespective of other conditions. We quantify their similarity and provide predictions in §2.3.4.1. This result holds for gap and no-gap simulations. To visualize this trend, we group the results by initial eccentricity distribution in Figure 2.6. The initial period distribution has no discernible effect on the shape of the final eccentricity distribution.

As expected, tidal efficiency results in more circularized systems, increasing the vertical axis intercept of the cumulative distribution as shown in Figure 2.6 for no-gap simulations. Less efficient tides result in an abundance of RL binaries, which can also increase the vertical axis intercept of the cumulative distribution. Recall that we artificially set eccentricity of the *RL* systems to 0.01, which may inflate the number of circularized systems. Irrespective of efficiency, tides have no effect on the overall shape or functional form (e.g., thermal) of the distribution.

2.3.3 Period distribution and the effect of tides

The final long period distribution tends to retain the same shape and curvature as the birth distribution irrespective of other conditions. We quantify the similarity and provide predictions in Section 2.3.4.2.

As mentioned above, we treat the RL systems as tight binaries. Figure 2.7 illustrates the strong dependency of the fraction of circularized systems on tidal efficiency. The dependency of RL system fraction on tidal efficiency is less pronounced, but generally less efficient tides result in more RL crossed systems. Figure 2.7 exemplifies this trade-off between circularized systems and RL-crossed systems, where the red curves count RL binaries. An RL crossing

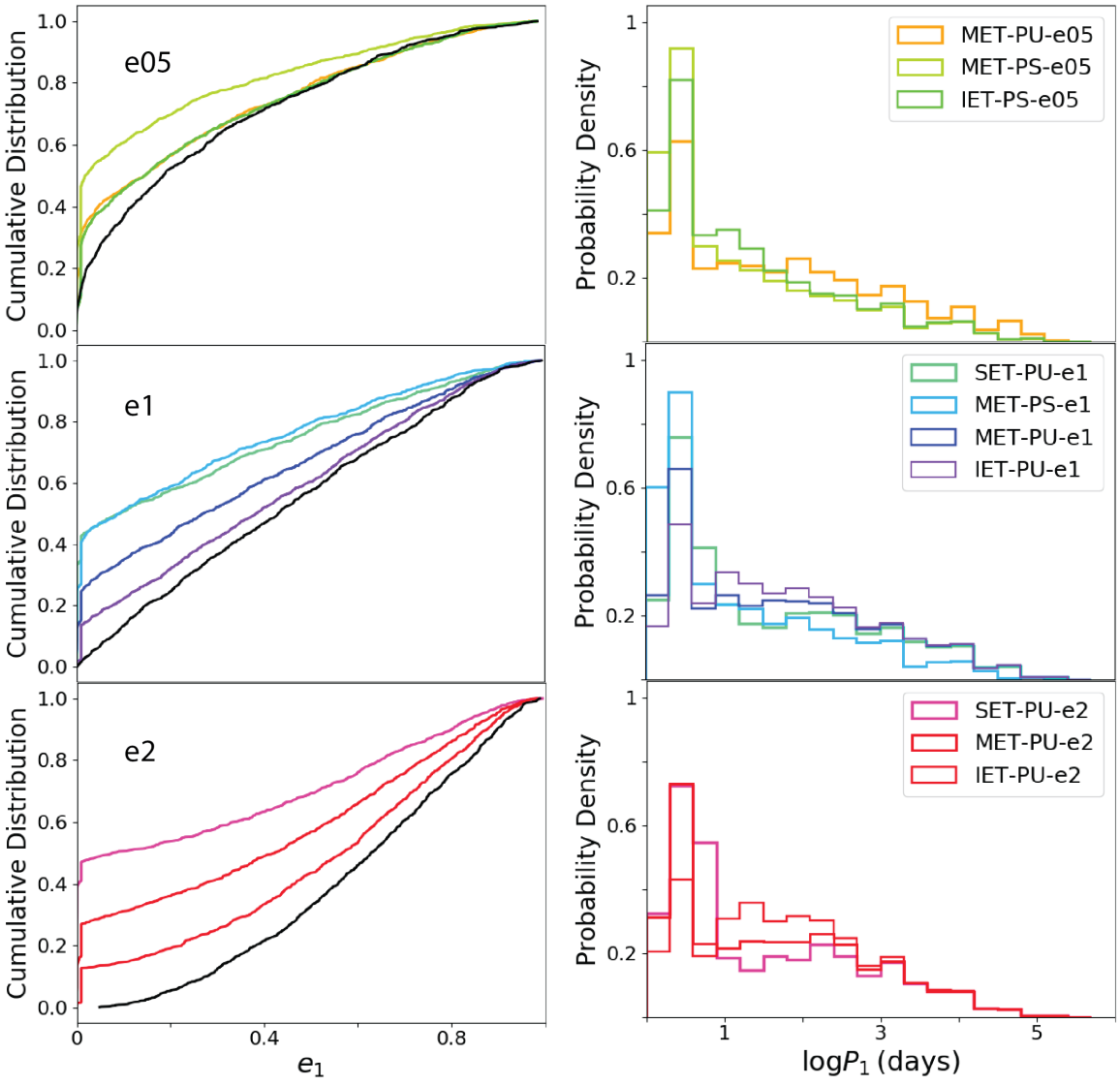

Figure 2.6: **No-gap simulation results by eccentricity.** We consider the results for no-gap simulations by their eccentricity birth distribution. We create a color spectrum based on tidal efficiency and plot the birth eccentricity distribution in black. With the exception of low eccentricities where there is a build-up of circular systems, the final cumulative distribution strongly resembles the birth distribution.

occurs when the EKL mechanism drives extreme eccentricity excitations before before tides can shrink and circularize the system. A lower tidal efficiency therefore gives systems more chances to cross the RL. With the exception of the blue curves in Figure 2.7, we include RL binaries as short-period systems unless otherwise noted.

In Figure 2.7, the final period distribution for gap simulations appears bimodal and exhibits a dearth of systems at intermediate periods. The peak at short-periods consists of RL and tidally tightened systems. In tidally inefficient (IET) simulations, this peak comprises RL binaries, while the vast majority of systems remain at long periods. Even with the most efficient tides (SET), 10 Myr of EKL evolution fail to fill the gap.

Since tidal efficiency is highly sensitive to stellar radius, larger radii yield more circularized systems. Additionally, the final periods of these systems depend on the stellar radii due to angular momentum conservation (Ford & Rasio, 2006). Therefore, as stars leave the main sequence and inflate, we expect circularized systems to have longer periods. To illustrate this behaviour, we consider three approaches to the mass-radius relation in Figure 2.8. Specifically, we consider the ZAMS mass-radius relation $R = 1.01M^{0.57}$ (blue line), as well as $R = 1.33M^{0.55}$ and the TAMS mass-radius relation, $R = 1.61M^{0.81}$ (e.g., Demircan & Kahraman, 1991) (green and red lines, respectively). To highlight the differences, we include a gap and make the tides unrealistically efficient (UET, unrealistic equilibrium tides). As shown in the figure, the larger radii correspond to longer periods for the tidally tightened binaries. Additionally, larger radii result in a more filled gap at intermediate periods. However, even with unrealistically efficient tides, the TAMS distribution fails to match observations.

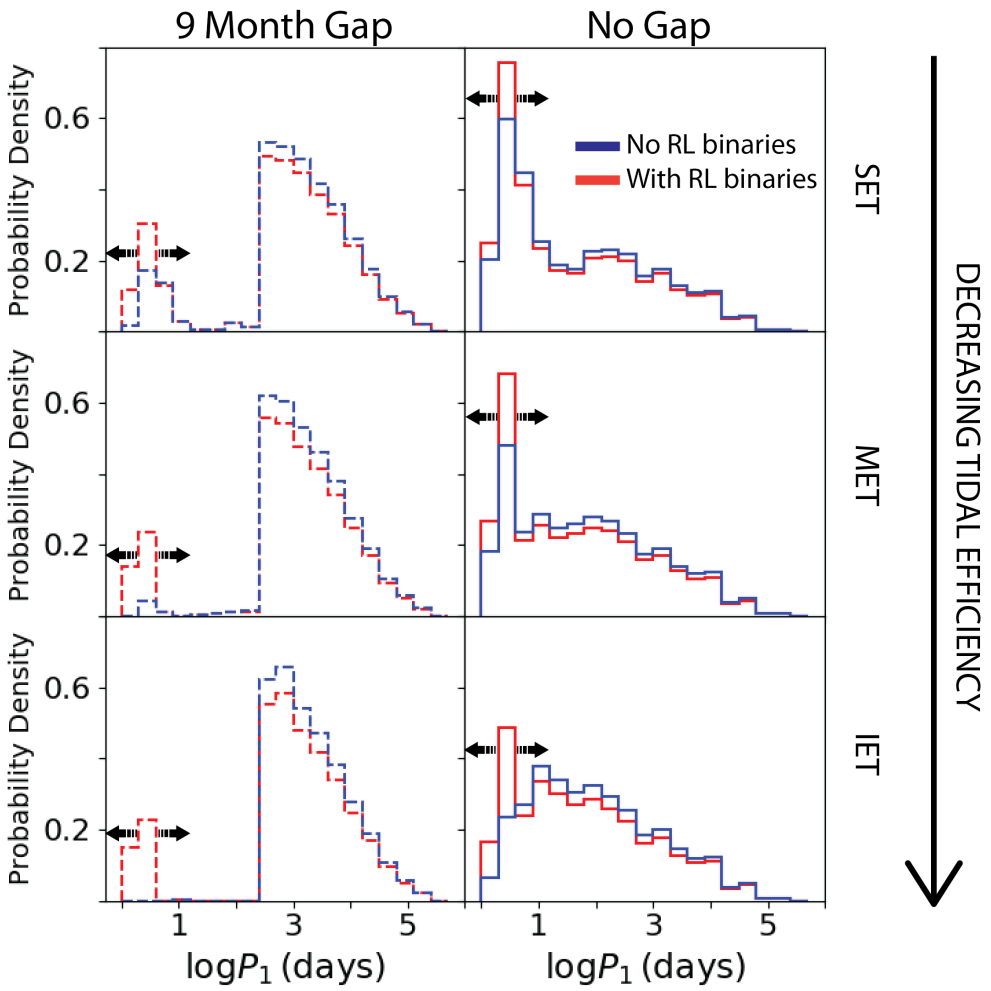

Figure 2.7: **Tidal efficiency and final period distributions.** We show the final period distributions for three different tidal efficiencies: SET, MET, and IET, in order of greatest to least efficiency. The red distribution includes RL crossed systems as tight binaries with periods calculated from angular momentum conservation and the RL stopping condition. These systems therefore appear in a sharp, artificial peak. We use arrows to indicate that the width and true shape of this peak remain unknown. The blue distribution does not include RL crossed systems.

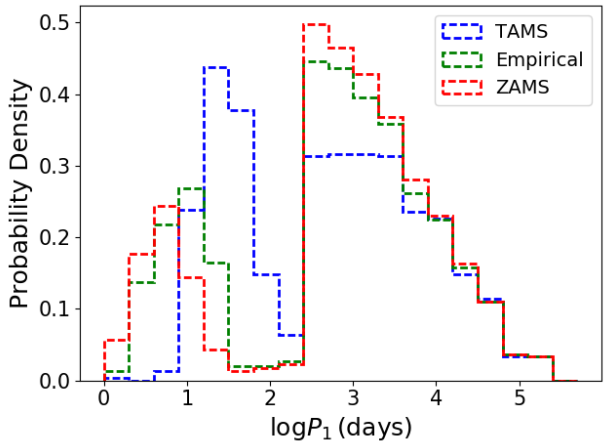

Figure 2.8: **Stellar radii and final period distributions.** Here we show the dependence of the final inner binary period (P_1) probability density on the mass-radius relation for UET simulations with $t_v = 0.005$. The TAMS (red) and ZAMS (blue) relations yield the largest and smallest radius, respectively, for a given mass. Larger radii shift the peak to larger periods.

2.3.4 Predictions: Observable signatures of Birth Properties

2.3.4.1 Eccentricity

To quantify the degree of similarity between the simulated birth and final eccentricity distributions, we fit a function of the form

$$\mathrm{cdf}_e = \kappa_e e^{\alpha_e} + \beta_e \ , \tag{2.7}$$

to the initial and final cumulative distributions, where α_e is the index of the power law and κ_e and β_e are constants. The parameters have the following limits: $0 < \kappa_e < 3$, $-2 < \alpha_e < 2$, and $0 < \beta_e < 0.6$. We argue that the vertical axis intercept, β_e, must be greater than or equal to zero because we are fitting a cumulative distribution. We fit both the initial and final distributions to show consistency between the two. As depicted in Figure 2.9, α_e changes by 0.3 at most, and only for the most efficient tides. We caution that while this trend holds for hierarchical triple dynamics, we do not account for other dynamical processes that may alter the eccentricity distribution.

We vary the range of eccentricity values over which we fit. When fitting over the full range

of eccentricity values, we impose the condition that $e > 0.01$ to absorb all circularized and RL-crossed binary systems into the vertical-axis intercept. We also fit over the range $0.1 < e < 0.7$. We recommend fitting over this range because the EKL Mechanism tends to affect high eccentricity systems the most. As these more eccentric systems circularize or cross the Roche limit, they increase the number of low eccentricity systems. Similarly, a fit of the birth distribution over this range better reflects the function used to generate values because the stability criteria target the extremes.

2.3.4.2 Orbital Period

We use a function of the same form, $\mathrm{cdf}_P = \kappa_P \log P^{\alpha_P} + \beta_P$, with the same limits on α_P, κ_P, and β_P. We fit the period distribution over the range $1 < \log P < 3$. We select the lower limit to avoid the newly-formed peak of short-period systems. This lower limit must be adjusted to accommodate the width of the short-period peak, which will depend on the stellar radii (Figure 2.8) and therefore the age of the binary system when it circularizes. The reason for the upper limit is twofold: the stability criteria curb the number of long period systems, causing our initial distributions to converge at large period, and observational campaigns may not be sensitive to longer periods (e.g., Sana et al. (2013)). The birth distribution signature proves much more difficult to discern in the period distributions than in the eccentricity distributions. We find that the orbital period distribution is most consistently preserved over this range, $1 < \log P < 3$. The power α changes by at most ~ 0.3 for PU simulations and stays ≤ 0.5 for PS simulations.

2.3.5 Comparison to observations

2.3.5.1 Eccentricity Distribution

Several groups have studied the eccentricity distributions of massive binaries. Specifically, Almeida et al. (2017) have examined OB-type spectroscopic systems in the Tarantula region to find that 40% of systems have small eccentricities (< 0.1). Furthermore, their eccentricity

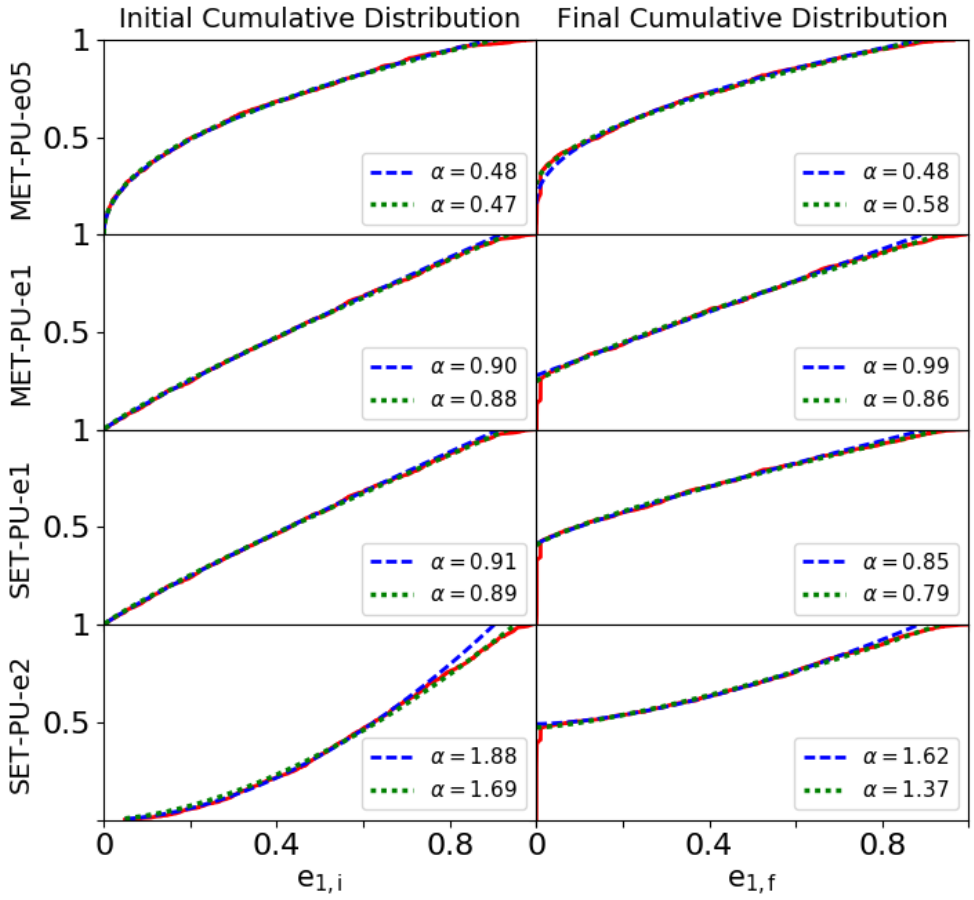

Figure 2.9: **Observational signature of the initial eccentricity conditions.** We show the simulated cumulative distribution for select no-gap simulations in red for the final (initial) distribution, right (left) column. Over-plotted is the fit $\mathrm{cdf}_e = \kappa_e e_1^{\alpha_e} + \beta_e$ for the distribution calculated between two boundaries. In blue, dashed line, we mark the $0.1 < e_1 < 0.7$ boundary while in green, dotted line, we mark the fit over the full range of eccentricity values. The fit function takes the following form: $\mathrm{cdf}_e = \kappa_e e_1^{\alpha_e} + \beta_e$. The final distribution mirror the initial distribution and thus can serve as an observational signature.

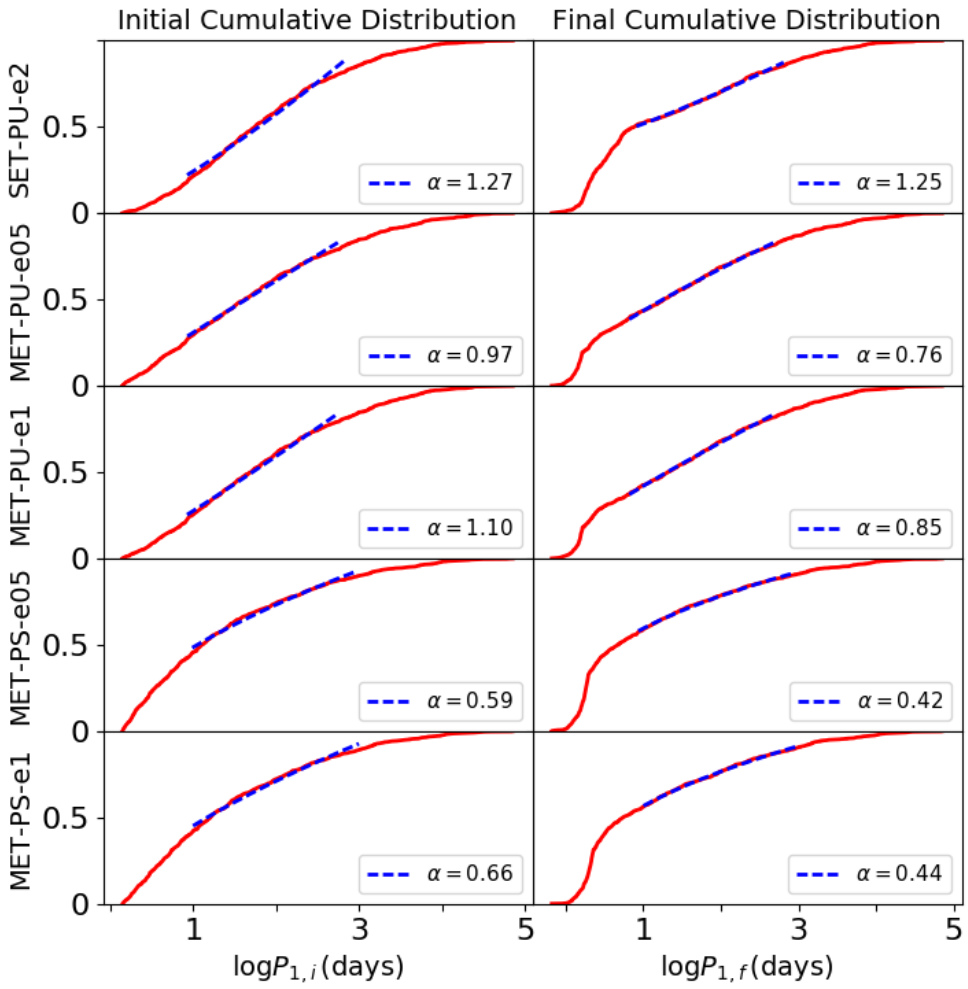

Figure 2.10: **Traces of the initial orbital period distribution.** We show the simulated initial (left) and final (right) cumulative no-gap period distributions. We overplot a fit with of the form $\mathrm{cdf}_P = \kappa_P (\log P)^{\alpha_P} + \beta_P$. We fit the distribution over the range $1 < \log P < 3$. We find that a signature of the birth distribution is best preserved over this range.

distribution appears uniform. However, the cumulative distribution flattens slightly for high (> 0.6) eccentricities, indicating fewer systems there. In a study of 48 massive systems from the Cygnus OB2 association, Kobulnicky et al. (2014) also show a flattening in the cumulative distribution at high eccentricity and attribute it to an observational bias. While this observed flattening may indeed reflect observational biases, we do find that our stability conditions curb the number of high eccentricity systems. As a result, our initial conditions exhibit flattening at large eccentricities (see Figure 2.1), which persists in the final distribution.

Similar to Almeida et al. (2017), Kobulnicky et al. (2014) note an abundance of low (< 0.1) eccentricity systems and conclude that the distribution is uniform for $e \lesssim 0.6$. In their review, Duchêne & Kraus (2013) also suggest that massive binaries follow a uniform eccentricity distribution, while Sana & Evans (2011) and Sana et al. (2012) give a probability density of the form $f(e) \propto e^{-0.5}$. Moe & Di Stefano (2017) find a thermal eccentricity distribution, $f(e) \propto e$, for OB-type binaries using the catalog from Malkov et al. (2012). However, their finding pertains to wider binaries with periods between 10 and 100 days, and many of our systems have shorter periods.

We find that the power law index is a good indicator of the initial condition. Additionally, Geller et al. (2019) determine that star cluster dynamics has little to no effect on the shape of the eccentricity distribution for binaries with modest orbital periods. These combined results imply that the final distribution resembles the birth distribution. The birth distribution of population with uniform eccentricities is therefore also uniform.

2.3.5.2 Period Distribution

Duchêne & Kraus (2013) estimate that 30% of massive binaries have periods of less than ten days. Sana & Evans (2011) find that 50% to 60% of systems fall at $\log P < 1$. Similarly, the data of Almeida et al. (2017) indicate an abundance ($\sim 40\%$) of short-period (< 1 week) systems. Kobulnicky et al. (2014) also affirm the abundance of short-period binaries.

Counting RL binaries in the no-gap simulations, systems with $\log P < 1$ represent 45%, 36%, and 29% of the SET, MET, and IET inner binaries, respectively, in Figure 2.7. The super efficient tides (SET, first row) seem too efficient. However, counting only systems with $\log P < 3.4$ to reflect observational limits, the SET and MET simulations match the estimates of Sana & Evans (2011) and Kobulnicky et al. (2014) with 51% and 42% short-period ($<$ 10 days) systems, respectively. The IET simulation has 34%. Additionally, observations may not be sensitive to our so-called RL binaries. In that case, the IET tides become too inefficient to account for observations. Examining only tidally-tightened systems, the fractions of short-period binaries fall to 46%, 34% and 24% of total systems with $\log P < 3.4$ for SET, MET, and IET simulations, respectively.

A power law of the form $f(\log P/\text{days}) \propto (\log P/\text{days})^{\alpha}$ is often fitted to the orbital period distribution (e.g., Kobulnicky et al., 2014). The index of this power law varies in the literature. Sana et al. (2012) suggest $\alpha = -0.55$, while Sana et al. (2013) find $\alpha = -0.45$. Almeida et al. (2017) conclude that an index between -0.2 and -0.5 reproduces the data well depending on the range over which they fit. Kobulnicky et al. (2014) suggest that tight binary peak has some structure, i.e. the distribution is not uniform at short-periods.

In Figure 2.11, we show the cumulative distributions for all of our no-gap simulations over the range $0.15 < \log P < 3.4$. Bounded by the curves $\text{cdf}_P \sim (\log P)^{0.8}$ (Almeida et al., 2017; Kobulnicky et al., 2014) and $\text{cdf}_P \sim (\log P)^{0.5}$ (Sana et al., 2012, 2013), the gray region depicts the range of power laws fitted to observations. While several of our simulated results resemble the power laws fitted to the data, generally, SET and PS simulations seem to overpredict the number of short-period systems, while IET simulations underpredict the number of short period systems.

We perform a Kolmogorov-Smirnov (KS) two-sample test to compare our final period distributions to observations. We perform this test both with and without including RL binaries in our simulated sample. Comparing to the data of Sana et al. (2012), we cannot reject

the null hypothesis that the observations and simulated results share a parent probability density distribution for the following simulations: MET-PS-e05, MET-PS-e1, SET-PU-e2, IET-PS-e05 both with and without RL binaries. We also perform this test with the data from Kobulnicky et al. (2014) and find that we cannot reject the null hypothesis for MET-PS-e05 and IET-PS-e05 without RL binaries; MET-PU-e2 and MET-PU-e05 with RL binaries; and SET-PU-e2 and SET-PU-e1 both with and without RL binaries. We do not assign much significance to these results. We have a number of systems, the RL binaries, with poorly understood periods in MET and IET no-gap simulations, which hinder a statistical comparison between our results and the data. Additionally, the data have far fewer systems and are subject to observational biases: at large periods, the observed distribution likely diverges from the intrinsic distribution (Sana et al., 2012). The latter explains why the KS test favors PS and SET simulations, while the fitted power laws more often coincide with MET-PU simulations (Figure 2.11).

Unlike the no-gap simulations, the gap simulations seem to be in tension with observations. We plot the cumulative distributions for the gap simulations with more efficient tides in Figure 2.12. The curves all exhibit a similar behavior indicative of a bimodal distribution. We again perform a KS test to compare our simulated results with the observations. The bottom panel of Figure 2.12 plots simulation results with the data from Sana et al. (2012) and Kobulnicky et al. (2014) that we test. We find that we can reject the null hypothesis that the simulated distributions and data are drawn from the same parent probability density distribution. Two major differences separate our simulated results from the observations: the persistence of a substantial population of long-period systems and the lack of intermediate period binaries, as illustrated by Figure 2.7. While the true separations of RL binaries – and whether they can fall at intermediate periods – is highly uncertain, a substantial long-period population will nonetheless persist.

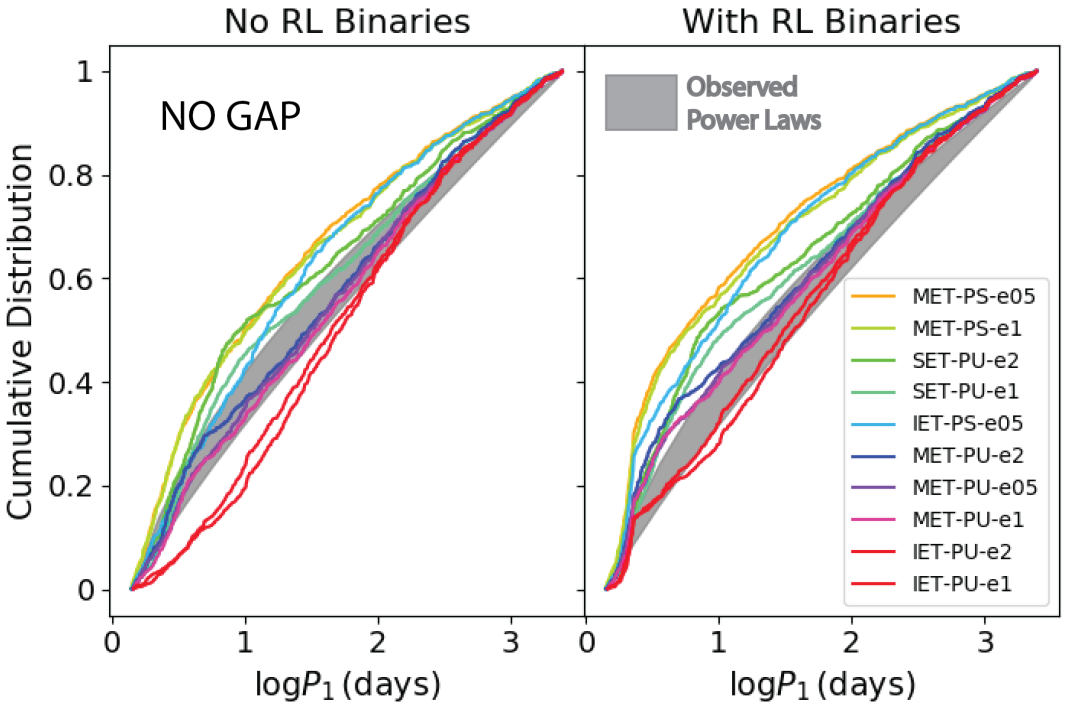

Figure 2.11: **Power laws from observations compared with no-gap results** We plot the cumulative distributions for our no-gap simulations with and without RL binaries. The gray shaded region encompasses the range of power laws indicated by observations. The curves $\mathrm{cdf}_P \sim (\log P)^{0.8}$ (Almeida et al., 2017; Kobulnicky et al., 2014) and $\mathrm{cdf}_P \sim (\log P)^{0.5}$ (Sana et al., 2012, 2013) bound the gray region. To avoid visual clutter, we deviate from our preferred presentation for the period distributions, a probability density, and instead focus on cumulative distributions here.

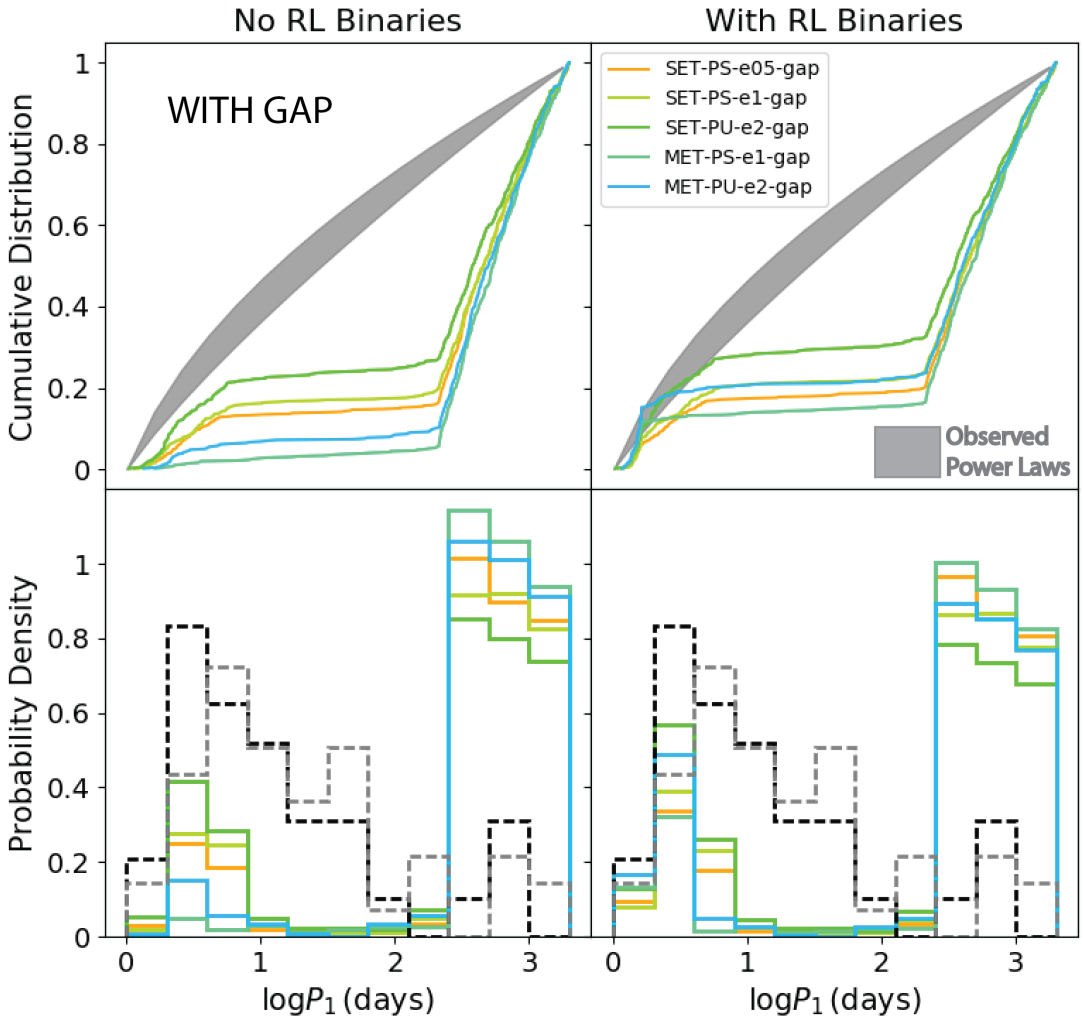

Figure 2.12: **Upper Panel: Power laws from observations compared with gap results** We plot the cumulative distributions for select gap simulations with and without RL binaries. These simulations have more efficient (SET or MET) tides and therefore the most short-period systems. The gray shaded region represents observationally constrained power laws. The curves $\mathrm{cdf}_P \sim (\log P)^{0.8}$ (Almeida et al., 2017; Kobulnicky et al., 2014) and $\mathrm{cdf}_P \sim (\log P)^{0.5}$ (Sana et al., 2012, 2013) bound this region. **Lower Panel: Probability density with data** We plot the probability densities for select gap simulations with and without RL binaries. The gray and black dashed histograms represent data from Kobulnicky et al. (2014) and Sana et al. (2012), respectively.

2.4 Discussion

A distant stellar companion can drive the long-term evolution of a massive stellar binary. Distant companions, which may be quite common, can therefore alter the observed orbital parameter distributions for massive binaries. We characterize these effects for a large variety of birth distributions and tidal efficiencies. We find the following:

- **Spin-Orbit Angle Distribution:** Figure 2.5 plots the spin-orbit angles and periods of 3000 realizations of massive triples color-coded by eccentricity. For long-period systems, no trend in spin-orbit angle and eccentricity exists. However, as systems circularize at periods of about 10 days, the orbit and stars' angular momenta align such that the spin-orbit angle goes to zero, with a few exceptions: occasionally the spin-orbit angle becomes locked in a (non-zero) resonance, called a Cassini resonance.

- **Eccentricity distribution:** The final eccentricity distribution is an excellent indication of the birth distribution. The cumulative distribution retains the curvature of the birth distribution. Since the EKL Mechanism most affects high eccentricity systems, a fit over the range $0.1 < e < 0.7$ of a function $\mathrm{cdf_e} \propto e^{\alpha_e}$ quantifies this trend (see Figure 2.9). Generally, the change in α_e is within 0.3, with a tendency to flatten – or render more uniform – the eccentricity distribution.

- **Period distribution:** A signature of the birth period distribution persists at $1 < \log P < 3$. We fit the period cumulative distribution with a power law over this range. The index changes by ~ 0.3 for the uniform initial condition and remains $\lesssim 0.5$ for $\mathrm{cdf}_P \sim (\log P)^{0.5}$ (PS) initial condition simulations (Figure 2.10).

- **Short period binaries:** Observations indicate an abundance of short-period binaries (e.g., Duchêne & Kraus, 2013). In our simulations, the tidal efficiency determines both the resulting number of short-period binaries and the dominant type of short-period system. Less efficient tides give systems more chances to cross the Roche limit, while

efficient tides yield more circularized, tight binaries. The former results in an artificial peak in our final period distribution because the final properties of such systems remain uncertain. Due to angular momentum conservation, the final period of any short-period system is proportional to the stellar radius. We treat the stellar radii as constant. However, realistically, the radii will expand as the stars age. Systems which tidally tighten or cross the Roche Limit at later times will therefore fall at longer periods (Figure 2.8).

- **Initial Period Gap:** Sana et al. (2017) suggest that massive binaries may form with large separations and tighten over time to match the parameter distributions of older populations. The EKL mechanism in concert with tidal dissipation represents a channel for producing hardened binaries. However, the EKL mechanism fails build up a sufficient population of short period binaries if we begin with a lower period cutoff of nine months (Figure 2.12).

  We perform a brief calculation to assess whether type II migration may fill a 9 month gap in the inner period distribution. Following Armitage (2007), the type-II migration timescale τ can be written as: $\tau \sim 2/(3\alpha)(h/a_1)^{-2}\Omega^{-1}$, where α is related to the viscosity, h is the scale height, and h/a_1 represents the disk aspect ratio. Ω denotes the angular velocity. A nine month period corresponds to a roughly 2 AU semi-major axis. Taking the primary and secondary to have masses 10 and 5 $M_\odot$, respectively, Ω is approximately 0.7 yr^{-1}. We assume that $h/a_1 \approx 0.07$ (e.g., Ruge et al., 2013) and $\alpha \approx 0.01$ (Armitage, 2007). We find that the timescale is about 2×10^4 yr. Type II migration therefore represents a mechanism to bridge an initial period gap, as suggested by Sana et al. (2017), with observations of older populations. Acting over a short timescale to tighten binaries, type II migration may fill the gap in the period distribution. If a binary system undergoing migration has a third companion, the gas will mostly suppress the gravitational perturbation of the tertiary star, although the

system may develop an inclination between the disk and the companion (e.g., Martin et al., 2014).

- **Comparison with Observations: no initial period gap and moderate tides** We compare our cumulative distributions for the final inner orbital period with the observationally constrained power laws in Figure 2.11. Many of our results fall in the region bounded by the power laws indicated by the literature (e.g., Almeida et al., 2017). Howerver, generally, simulations with moderately efficient tides (MET) and a uniform birth period distribution match observed distributions well.

  Several observations indicate a uniform eccentricity distribution except at high eccentricity (e.g., Kobulnicky et al., 2014). Only simulations that begin with a uniform eccentricity distribution produce a uniform distribution as the end result.

Unlike previous studies of EKL evolution in triple stellar systems (e.g., Naoz & Fabrycky, 2014; Bataille et al., 2018; Moe & Kratter, 2018), we find that the final period and eccentricity distributions carry a clear signature of the initial distributions. This behavior is a consequence of the short timescale of evolution (~ 10 Myr) and the moderately efficient tides of stars with radiative envelopes. We expect that as stellar evolution increases the stellar radii and causes mass loss, the orbital configurations will significantly alter.

Acknowledgements

SN thanks Howard and Astrid Preston for their generous support. SCR acknowledges support from the Eugene Cota-Robles Fellowship.

2.5 Appendix

2.5.1 Simulation Parameters

We run several large Mont-Carlo simulations to cover a wide range of initial conditions. Table 2.2 describes the 38 sets of Monte-Carlo simulations. Some simulations adopt a Kroupa mass function with limits $1M_{\odot} < m < 20M_{\odot}$ ("K1") or $6M_{\odot} < m < 20M_{\odot}$ ("K6"). We find that the masses affect the results insofar as they determine the tidal efficiency. For example, for the former limits, the abundance of low mass stars with efficient tides will result in more circularized systems even when using the IET prescription.

Label	Radius	Mass	Eccentricity	Period	Tides
PU-e1-M10-TAMS	TAMS	$m_1 = 10M_\odot$ & Uniform q	Uniform	Uniform	SET
PU-e1-M10-Emp	Empirical	$m_1 = 10M_\odot$ & Uniform q	Uniform	Uniform	SET
PU-e1-M10-ZAMS	ZAMS	$m_1 = 10M_\odot$ & Uniform q	Uniform	Uniform	SET,MET,IET, UET(g),SET(g),MET(g),IET(g)
PS-e1-M10-ZAMS	ZAMS	$m_1 = 10M_\odot$ & Uniform q	Uniform	$f(\log P) \sim \log P^{-0.5}$	SET, MET, SET(g)
PS-e05-M10-TAMS	TAMS	$m_1 = 10M_\odot$ & Uniform q	$f(e) \sim e^{-0.5}$	$f(\log P) \sim \log P^{-0.5}$	UET(g)
PS-e05-M10-Emp	Empirical	$m_1 = 10M_\odot$ & Uniform q	$f(e) \sim e^{-0.5}$	$f(\log P) \sim \log P^{-0.5}$	UET(g), LET(g)
PS-e05-M10-ZAMS	ZAMS	$m_1 = 10M_\odot$ & Uniform q	$f(e) \sim e^{-0.5}$	$f(\log P) \sim \log P^{-0.5}$	MET, IET, UET(g), SET(g), MET(g)
PU-e05-M10-ZAMS	ZAMS	$m_1 = 10M_\odot$ & Uniform q	$f(e) \sim e^{-0.5}$	$f(\log P) \sim \log P^{-0.5}$	MET
PU-e2-M10-ZAMS	ZAMS	$m_1 = 10M_\odot$ & Uniform q	Thermal	Uniform	SET, MET, IET, SET(g), MET(g)
PS-e2-K6-Emp	Empirical	Kroupa with $6M_\odot < m < 20M_\odot$	Thermal	$f(\log P) \sim \log P^{-0.5}$	LET(g)
PS-e05-K6-Emp	Empirical	Kroupa with $6M_\odot < m < 20M_\odot$	$f(e) \sim e^{-0.5}$	$f(\log P) \sim \log P^{-0.5}$	LET(g)
PU-e05-K6-Emp	Empirical	Kroupa with $6M_\odot < m < 20M_\odot$	$f(e) \sim e^{-0.5}$	Uniform	LET(g)
PU-e2-K6-Emp	Empirical	Kroupa with $6M_\odot < m < 20M_\odot$	Thermal	Uniform	LET(g)
PS-e1-K1-ZAMS	ZAMS	Kroupa with $1M_\odot < m < 20M_\odot$	Uniform	$f(\log P) \sim \log P^{-0.5}$	IET(g)
PU-e1-K1-ZAMS	ZAMS	Kroupa with $1M_\odot < m < 20M_\odot$	Uniform	$f(\log P) \sim \log P^{-0.5}$	IET
PU-e1-K6-ZAMS	ZAMS	Kroupa with $6M_\odot < m < 20M_\odot$	Uniform	$f(\log P) \sim \log P^{-0.5}$	LET
PU-e2-K1-ZAMS	ZAMS	Kroupa with $1M_\odot < m < 20M_\odot$	Thermal	Uniform	IET(g)
PS-e05-K1-ZAMS	ZAMS	Kroupa with $1M_\odot < m < 20M_\odot$	$f(e) \sim e^{-0.5}$	$f(\log P) \sim \log P^{-0.5}$	IET(g)
PS-e2-K1-ZAMS	ZAMS	Kroupa with $1M_\odot < m < 20M_\odot$	Thermal	$f(\log P) \sim \log P^{-0.5}$	IET
PU-e05-K1-ZAMS	ZAMS	Kroupa with $1M_\odot < m < 20M_\odot$	$f(e) \sim e^{-0.5}$	Uniform	IET
PU-e05-K6-ZAMS	ZAMS	Kroupa with $6M_\odot < m < 20M_\odot$	$f(e) \sim e^{-0.5}$	Uniform	LET

Table 2.2: Parameters and birth distributions used by each 10 Myr Monte Carlo simulation. A "g" denotes simulations that include a gap.

2.5.2 Fitting the Period Distribution

Taking a similar approach to Section 2.3.4.2, we fit the cumulative no-gap period distribution over the range $0.15 < \log P < 3.4$, selected to reflect the limits in, for example, Almeida et al. (2017) and Sana et al. (2013), in figure 2.13. With $0.4 < \alpha_P \leq 0.5$, PU-MET simulations best match observationally constrained cumulative distribution functions which have $0.5 < \alpha < 0.8$. We show additional examples in 2.14. The IET-PU distributions are too flat, while either SET or PS conditions give too pronounced curvature with $\alpha_P < 0.2$. Taking the observations and our fits at face value, we suggest that moderately efficient tides – or another model with a similar efficiency – are the best candidate. However, these fits remain uncertain because of the RL binaries, included in the cumulative distribution.

We further suggest that cumulative distributions be fitted in two parts: one where the short-period peak occurs and one for periods longer that ~ 10 days. Since MET-PU simulations yield a similar final period distribution irrespective of eccentricity initial condition, we fit the MET-PU-e1 results as an example in Figure 2.15.

2.5.3 Additional Examples of Period Distribution Traces

We apply the method described in Section 2.3.4.2 to all of our no-gap simulations to find traces of the initial period distribution in the final result. We show the other five simulations here. As noted in Section 2.3.4.2, the index α of the power law fitted over the range $1 < \log P < 3$ changes by at most ~ 0.3 for PU simulations and stays $\lesssim 0.5$ for PS simulations.

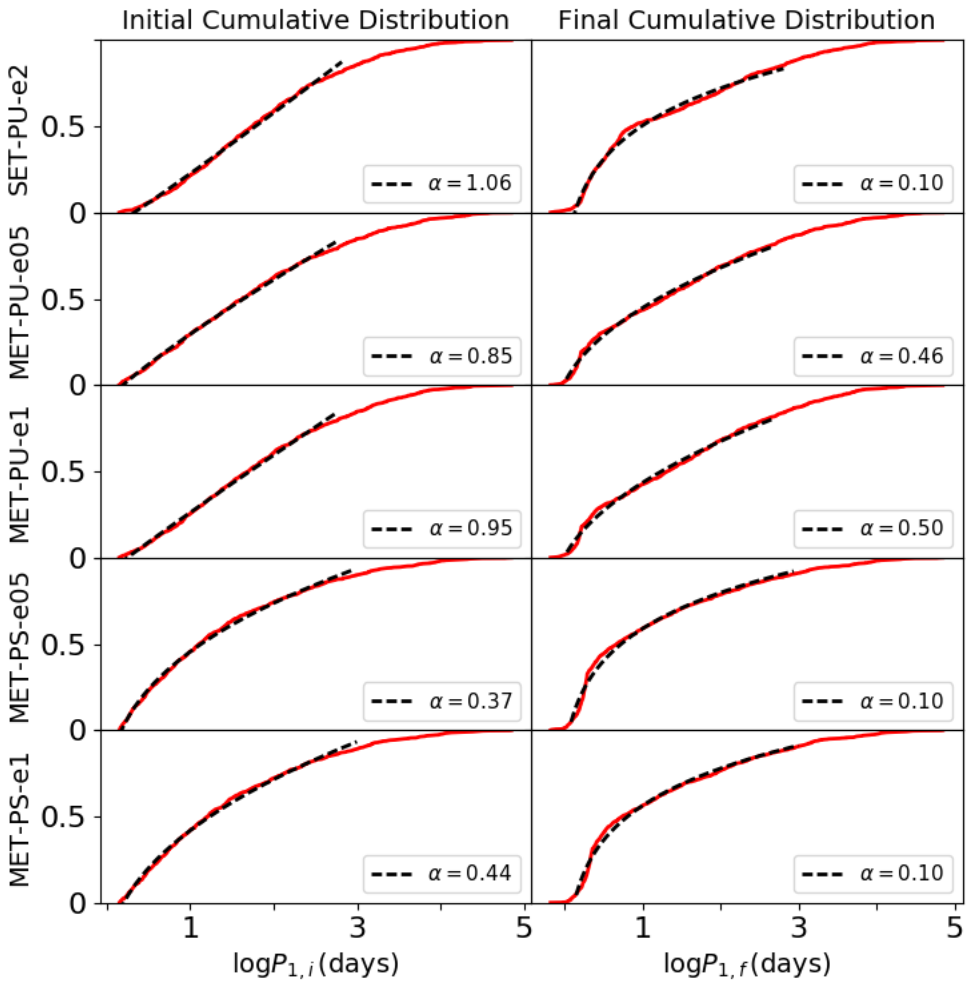

Figure 2.13: **Final period distribution fit.** We show the simulated cumulative distribution in red for the final (initial) distribution, right (left) column. We overplot a fit with of the form $\mathrm{cdf}_P = \kappa_P (\log P)^{\alpha_P} + \beta_P$. We fit the distribution over the range $0.15 < \log P < 3.4$ to examine overall trends in the period distribution.

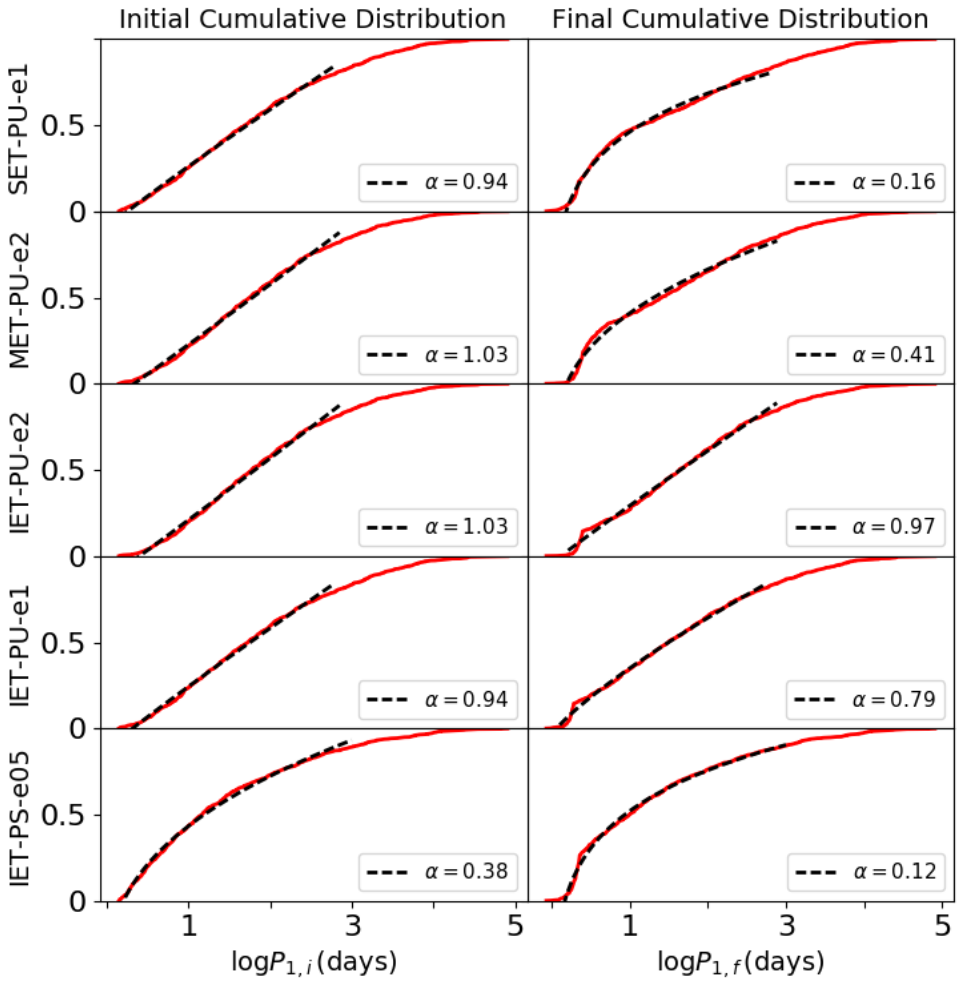

Figure 2.14: **Final period distribution fit, additional examples.** We show the simulated cumulative distribution in red for the final (initial) distribution, right (left) column. We overplot a fit with of the form $\mathrm{cdf}_P = \kappa_P (\log P)^{\alpha_P} + \beta_P$. We fit the distribution over the range $0.15 < \log P < 3.4$ to examine overall trends in the period distribution.

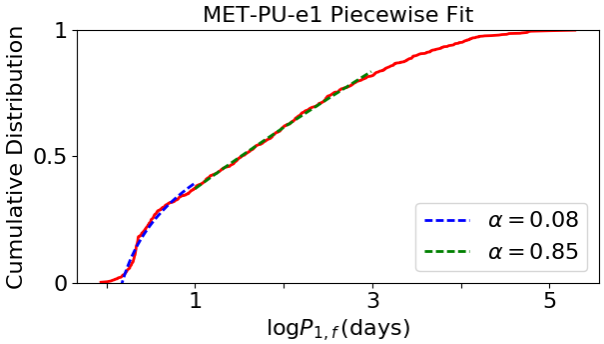

Figure 2.15: **Example two-part fit of period distribution** We fit the most promising (PU, MET) simulated results with in two parts, $0.15 < \log P < 1$ and $1 < \log P < 3$. We use the e1 simulation and note that the eccentricity does not affect this result.

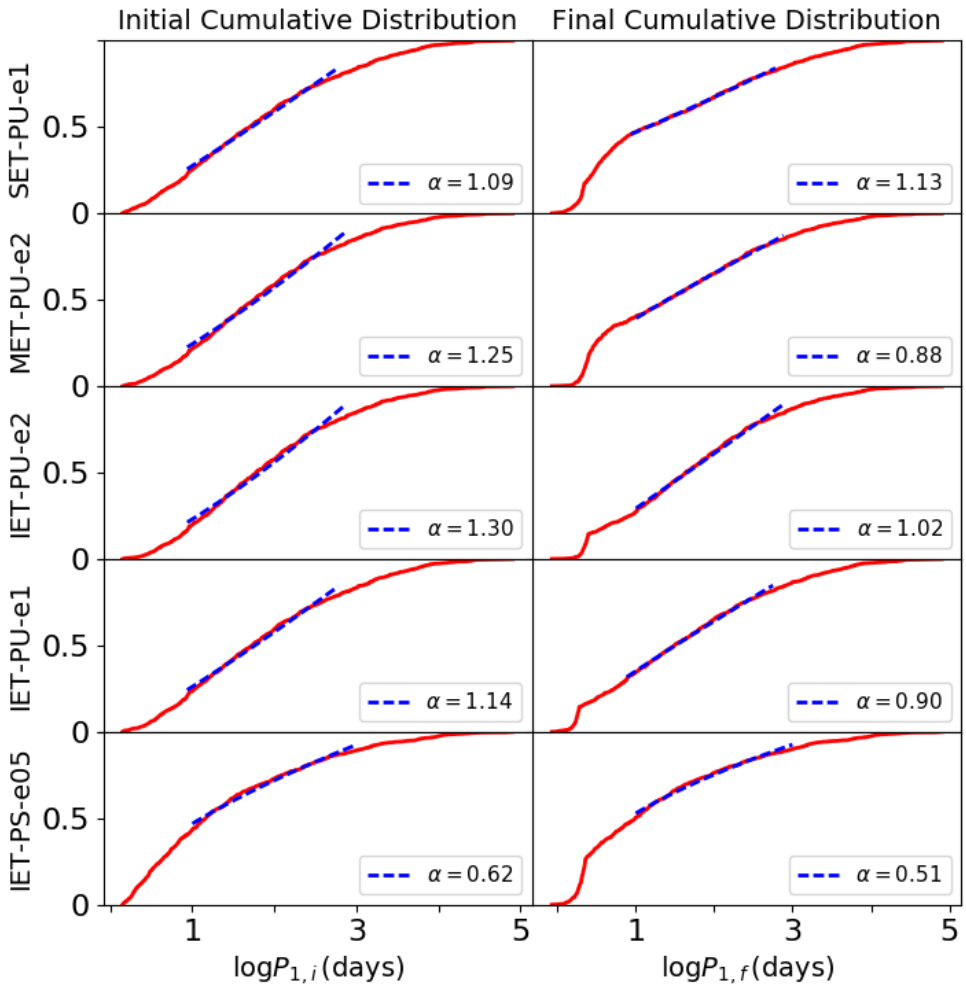

Figure 2.16: **Signature of the initial orbital period distribution.** We show the simulated cumulative distribution in red for the final (initial) distribution, right (left) column. We overplot a fit with of the form $\mathrm{cdf}_P = \kappa_P (\log P)^{\alpha_P} + \beta_P$. We fitted the distribution over the range $1 < \log P < 3$ to find a signature of the birth distribution.

CHAPTER 3

Using Binaries to Constrain the Density of Objects in the Galactic Center

Stars often reside in binary configurations. The nuclear star cluster surrounding the supermassive black hole (SMBH) in the Galactic Center (GC) is expected to include a binary population. In this dense environment, a binary frequently encounters and interacts with neighboring stars. These interactions vary from small perturbations to violent collisions. In the former case, weak gravitational interactions unbind a soft binary over the evaporation timescale, which depends on the binary properties as well as the density of surrounding objects and velocity dispersion. Similarly, collisions can also unbind a binary, and the collision rate depends on the density. Thus, the detection of a binary with known properties can constrain the density profile in the GC with implications for the number of compact objects, which are otherwise challenging to detect. We estimate the density necessary to unbind a binary within its lifetime for an orbit of arbitrary eccentricity about the SMBH. We find that the eccentricity has a minimal impact on the density constraint. In this proof-of-concept, we demonstrate that this procedure can probe the density in the GC using hypothetical young and old binaries as examples. Similarly, a known density profile provides constraints on the binary orbital separation. Our results highlight the need to consider multiple dynamical processes in tandem. In certain cases, often closer to the SMBH, the collision timescale rather than the evaporation timescale gives the more stringent density constraint, while other binaries farther from the SMBH provide unreliable density constraints because they migrate

inwards due to mass segregation.

3.1 Introduction

Most galaxies have a 10^{6-9} $M_\odot$ supermassive black hole (SMBH) at their center (e.g., Kormendy, 2004; Ferrarese & Ford, 2005; Kormendy & Ho, 2013). The Milky Way's center hosts the closest known SMBH, Sagittarius A*, surrounded by a dense nuclear star cluster. With a mass of $4 \times 10^6\, M_\odot$, the SMBH dominates the gravitational potential in the inner parsec region (Ghez et al., 2005; Gillessen et al., 2009). The proximity of this environment presents a unique opportunity to broaden our understanding of the physical processes unfolding in galactic centers.

The nuclear star cluster is largely dominated by a diffuse population of old (> 1 Gyr) stars (Nogueras-Lara et al., 2019; Schödel et al., 2020), including several bright giants (e.g. Do et al., 2009). Observations have also unveiled a population of approximately $4 - 6$ Myr-old stars within the central pc of the Galactic Center (GC) (e.g., Lu et al., 2009; Bartko et al., 2010; Do et al., 2013a,b; Feldmeier-Krause et al., 2015). A subset of those young stars, the so-called the S-star cluster, have eccentric orbits that are distributed isotropically within ~ 0.04 pc of the SMBH (Ghez et al., 2005, 2008; Gillessen et al., 2009, 2017), though a recent study suggests that the S-stars may be arranged in two discs (Ali et al., 2020). Additionally, observations have revealed a stellar disk structure in the inner parsec region (e.g., Levin & Beloborodov, 2003; Paumard et al., 2006; Lu et al., 2009; Bartko et al., 2009; Yelda et al., 2014). Throughout this paper, when we refer to the GC, we are focusing on this inner region where the nuclear star cluster resides. This unique environment, a stellar cluster embedded within the gravitational potential of a SMBH, is expected to yield several interesting phenomena such as hypervelocity stars (e.g., Hills, 1988; Yu & Tremaine, 2003; Ginsburg & Loeb, 2007) and stellar binary mergers (e.g., Antonini et al., 2010, 2011; Prodan et al., 2015; Stephan et al., 2016, 2019). These phenomena require the existence of binaries

in this dense region.

Stars often reside in a binary configuration. Approximately 50% of KGF stars and more than 70% of OBA stars exist in binaries (e.g., Raghavan et al., 2010). However, few binaries have been observed in the GC. Approximately 0.05 pc from the SMBH, the equal mass binary IRS 16SW has a period of 19.5 days and total mass of approximately 100 $M_{\odot}$ (Ott et al., 1999; Martins et al., 2006). Pfuhl et al. (2014) confirm the existence of two additional binaries approximately 0.1 pc from the SMBH: a short-period (2.3 days) eclipsing Wolf-Rayet binary and a long-period (224 days) low eccentricity ($e = 0.3$) binary. These confirmed binaries are the most direct evidence of the broader binary population expected to reside in the GC. A near-infrared variability study has detected 10 binaries in the region of interest (Dong et al., 2017a,b). Observational studies suggest that the OB binary fraction in the GC is comparable to that in young massive stellar clusters (e.g., Ott et al., 1999; Rafelski et al., 2007), and the eclipsing young OB binary fraction in the GC is consistent with the local fraction (Gautam et al., 2019). Furthermore, the theoretical study Stephan et al. (2016) suggests a 70% binary fraction for the population from the most recent star formation episode, 6 Myr ago, in the nuclear star cluster (e.g., Lu et al., 2013).

Few systems have been identified because the detection of binaries in the GC stellar population faces several observational challenges. These challenges include high extinction towards the GC and extreme stellar crowding near the supermassive black hole. Adaptive optics (AO) on large ground-based telescopes, allowing deep, diffraction-limited observations of the GC stellar populations, can overcome some of these limitations. However, AO imaging limits photometric precision (e.g., Schödel et al., 2010; Gautam et al., 2019), while AO spectroscopic studies are not sensitive to fainter members of the GC stellar population (e.g., Do et al., 2013a). Furthermore, binary searches require large stellar sample sizes and frequent monitoring of the stellar population to measure sufficient photometric or spectroscopic variability. However, not many such surveys have yet been performed for the stellar population

in the central half parsec of the GC.

However, other phenomena hint at the existence of binaries in the GC. The abundant X-ray sources there may trace to binaries in which a black hole accretes material from a stellar companion (Muno et al., 2005; Cheng et al., 2018; Zhu et al., 2018; Hailey et al., 2018), while Muno et al. (2006, 2009) and Heinke et al. (2008) attribute these X-ray sources to Cataclysmic Variables, a binary composed of a White Dwarf and main-sequence star. Hypervelocity stars likely originate from a binary that has been disrupted by the SMBH, ejecting one of the binary members from the GC (e.g., Hills, 1988; Yu & Tremaine, 2003; Ginsburg & Loeb, 2007; Perets, 2009a,b). More recently, a theoretical study, Naoz et al. (2018) explains puzzling disk properties with an abundance of binary systems.

In a dense environment like the GC, a binary system frequently encounters other stars. Several studies have explored the complex physics and implications of these encounters (e.g., Heggie, 1975; Hills, 1975; Heggie & Hut, 1993; Rasio & Heggie, 1995; Heggie & Rasio, 1996; Binney & Tremaine, 2008; Hopman, 2009; Leigh et al., 2016, 2018; Hamers & Samsing, 2019). If a passing star approaches the binary with impact parameter on the order of the binary separation, it interacts more strongly with the closer binary member. This interaction imparts energy to the binary system and causes the binary to widen. Over a long period of time, many such encounters eventually unbind the binary. The evaporation timescale refers to the amount of time necessary for the binary to undergo this process (see the derivation in Binney & Tremaine, 2008). This timescale depends on the binary's characteristics as well as environmental properties such as the stellar number density and velocity dispersion. Additionally, stars in the binary can collide with passing objects with a timescale that also depends on the density of the system's environment (e.g., Sigurdsson & Phinney, 1993; Fregeau et al., 2004; Binney & Tremaine, 2008). The survival of the binary over its lifetime therefore depends on the surrounding density; too dense an environment results in the binary's destruction. Given these relations, a binary system with a known age provides an upper limit on the local

density and can constrain the density profile in the GC.

Mass segregation is expected to concentrate the dense remnants of massive stars in the central pc of the GC (e.g., Shapiro & Marchant, 1978; Cohn & Kulsrud, 1978; Morris, 1993; Miralda-Escudé & Gould, 2000; Baumgardt et al., 2004). Numerous studies explore the expected number of stellar mass black holes and their influence on the density profile of the GC (e.g., Miralda-Escudé & Gould, 2000; Freitag et al., 2006; Alexander & Hopman, 2009; Merritt, 2010; Aharon & Perets, 2016). In particular, if the GC evolved in isolation, it should be dynamical relaxed (e.g., Bar-Or et al., 2013), resulting in a simple, cusp-like power law density profile (e.g., Bahcall & Wolf, 1976; Alexander & Hopman, 2009; Keshet et al., 2009; Aharon & Perets, 2016)[1]. However, observations indicate that the profile may be shallower (e.g., Buchholz et al., 2009; Do et al., 2009; Bartko et al., 2010; Gallego-Cano et al., 2018, 2020; Schödel et al., 2014, 2018, 2020). A density constraint can clarify the profile and the number and distribution of stellar remnants, which are difficult to detect.

We expand upon the framework presented in Alexander & Pfuhl (2014), the first use of a binary to constrain the density of the GC. In particular, we derive the evaporation timescale for a binary with an arbitrary eccentricity about the SMBH. We consider several dynamical processes, such as collisions and two body relaxation, in this proof-of-concept of binaries as probes of the GC density. Similarly, a known density profile can be used to infer a binary's orbital configuration. We begin by outlining the equations that describe relevant dynamical processes, including evaporation, two-body relaxation, the Eccentric Kozai-Lidov mechanism, and collisions, in Section 3.2. Section 3.3 summarizes the qualitative outcomes of binary systems subjected to competing dynamical processes. We explore the use of binaries as a probe of the GC environment, specifically the underlying density distribution, and address the fates of older long-lived binaries in Section 3.4. Lastly, we constrain the parameter space

[1]Certain physical processes may also modify the density profile. For example, binary disruption by the SMBH can steepen the density cusp (Fragione & Sari, 2018)

for hypothetical systems by assuming that observed S-stars reside in a binary system in Section 3.5. We summarize our results in Section 3.6.

3.2 Equations

3.2.1 The Evaporation Process

The evaporation process describes the unbinding of a binary due to interactions with passing neighbors.[2] Derived using diffusion physics (Binney & Tremaine, 2008), the evaporation timescale depends on several properties. Some of these parameters pertain to the binary itself, such as the initial semimajor axis, $a_{\rm bin}$ and mass $M_{\rm bin}$, while others describe the binary's environment. In the latter category, the density of the scatterers, likely stars, and their velocity dispersion affect this timescale.

The evaporation timescale is inversely proportional to the density. The higher the density of scatterers, which are stars and stellar remnants, the more frequent the encounters. We assume that the density of objects is spherically symmetric and write it as a function of $r_\bullet$, the distance from the SMBH:

$$\rho(r_\bullet) = \rho_0 \left(\frac{r_\bullet}{r_0}\right)^{-\alpha} , \tag{3.1}$$

where ρ_0 is the normalized density at r_0 and α is the slope of the power law.[3] We use values $1.35 \times 10^6\, M_\odot/{\rm pc}^3$ and $0.25\,{\rm pc}$ for these parameters, respectively (Genzel et al., 2010). These values are very similar in magnitude to those presented in Schödel et al. (2018).

Additionally, the evaporation timescale is proportional to the velocity dispersion since the relative speed between the binary and passing star determines the length of each encounter.

[2]Binaries can also be ionized, that is, unbound in a single interaction with a neighbor. The associated timescale for this process is a factor of approximately $\ln\Lambda$ larger than the evaporation timescale (Heggie, 1975; Binney & Tremaine, 2008). We omit this process here because evaporation occurs on a faster timescale.

[3]We do not consider any broken power laws. However, in Section 3.4.1, the density constraint derived from a binary's survival depends very weakly on α, suggesting that, despite our assumptions here, the procedure can be used even if a broken power law describes the density profile in the GC.

For a low velocity dispersion, the passing star's gravitational force has longer to act on the binary, producing greater change in the binary's orbital configuration. The Jeans Equation relates the density distribution to the one dimensional velocity dispersion. We express the velocity dispersion as:

$$\sigma(r_\bullet) = \sqrt{\frac{GM_\bullet}{r_\bullet(1+\alpha)}}, \tag{3.2}$$

where G is the gravitational constant, α is the slope of the density profile, and $M_\bullet$ denotes the mass of the SMBH (Alexander, 1999; Alexander & Pfuhl, 2014).

We consider a binary at distance $r_\bullet$ from the SMBH. We adapt the evaporation timescale equation to depend explicitly on the distance $r_\bullet$ (Binney & Tremaine, 2008; Alexander & Pfuhl, 2014; Stephan et al., 2016):

$$t_{ev} = \frac{\sqrt{3}\sigma(r_\bullet)}{32\sqrt{\pi}G\rho(r_\bullet)a_{\rm bin}\ln\Lambda(r_\bullet)}\frac{M_{\rm bin}}{\langle M_*\rangle}, \tag{3.3}$$

where $M_{\rm bin}$ is the total mass of the binary and $\langle M_*\rangle$ is the average mass of a star in the GC.[4] The evaporation timescale also depends on the Coulomb logarithm $\ln\Lambda$, where Λ is the ratio of the maximum to minimum impact parameter. In the evaporation process, $b_{max} = a_{\rm bin}/2$ for the passing star to interact more strongly with one of the binary members. Otherwise, the encounter will affect the center of mass. The strongest deflection, 90°, gives b_{min}. We obtain the expression from Alexander & Pfuhl (2014):

$$\Lambda = 2\frac{\sigma^2}{v_{\rm bin}^2} = \frac{2a_{\rm bin}M_\bullet}{M_{\rm bin}r_\bullet(1+\alpha)}\ . \tag{3.4}$$

In the last transition, we substitute Eq. (5.3) for σ and $GM_{\rm bin}/a_{\rm bin}$ for the orbital velocity of the binary, averaged over the mean anomaly. This approximation assumes that the inner binary orbital timescale is shorter than the orbital timescale about the SMBH.

[4]We assume that $n\langle M_*^2\rangle \approx \rho\langle M_*\rangle$ from the evaporation timescale equation in Alexander & Pfuhl (2014). However, an alternative is defining $M_* = \langle M_*^2\rangle/\langle M_*\rangle$ such that ρM_* appears in the denominator of Eq. 3.16 following the notation of Kocsis & Tremaine (2011).

Combining these equations and assumptions, we find that the evaporation time has $r_\bullet$ dependence:

$$t_{ev} \propto \frac{r_\bullet^{\alpha-1/2}}{\ln\left(\beta/r_\bullet\right)} \ , \tag{3.5}$$

where

$$\beta = \frac{2a_{\rm bin}M_\bullet}{M_{\rm bin}(1+\alpha)} \ . \tag{3.6}$$

We illustrate the dependency of the evaporation timescale as a function of distance in Figure 5.1. Specifically, we plot the evaporation time of an equal mass $M_{\rm bin} = 2\,M_\odot$ binary with 0.1 and 0.5 au semimajor axis for $\alpha = 1$ to $\alpha = 2$ in Figure 5.1 in dark blue. The darkest line represents $\alpha = 1.75$, the profile for a dynamically relaxed single mass system (Bahcall & Wolf, 1976). As the evaporation process relies on weak encounters, the true evaporation time of a binary system likely does not differ substantially from the evaporation timescale (Perets et al., 2007). We extend the axes in Figure 5.1 to extreme values close to the SMBH, where our assumptions may break down, in particular regarding a continuous distribution of objects. However, we note that a recent analysis of S0-2 observations suggests that low-mass objects may still reside interior to its orbit (e.g., Naoz et al., 2020).

3.2.1.1 Binaries Soften with Time

The evaporation process requires that a binary begins in a soft configuration. A soft binary has a gravitational binding energy that is less than the kinetic energy of the neighboring stars:

$$s = \frac{E}{\langle M_*\rangle\sigma^2} < 1, \tag{3.7}$$

where $E = Gm_1m_2/(2a_{\rm bin})$ and $\langle M_*\rangle$ is the average stellar mass in the GC. This configuration allows a passing star to interact more strongly with one of the binary members. This condition places a minimum on the semimajor axis a binary can have to evaporate. Following Alexander & Pfuhl (2014), we refer to s as the softness parameter.

Additionally, soft binaries tend to soften over time. The evaporation timescale depends on

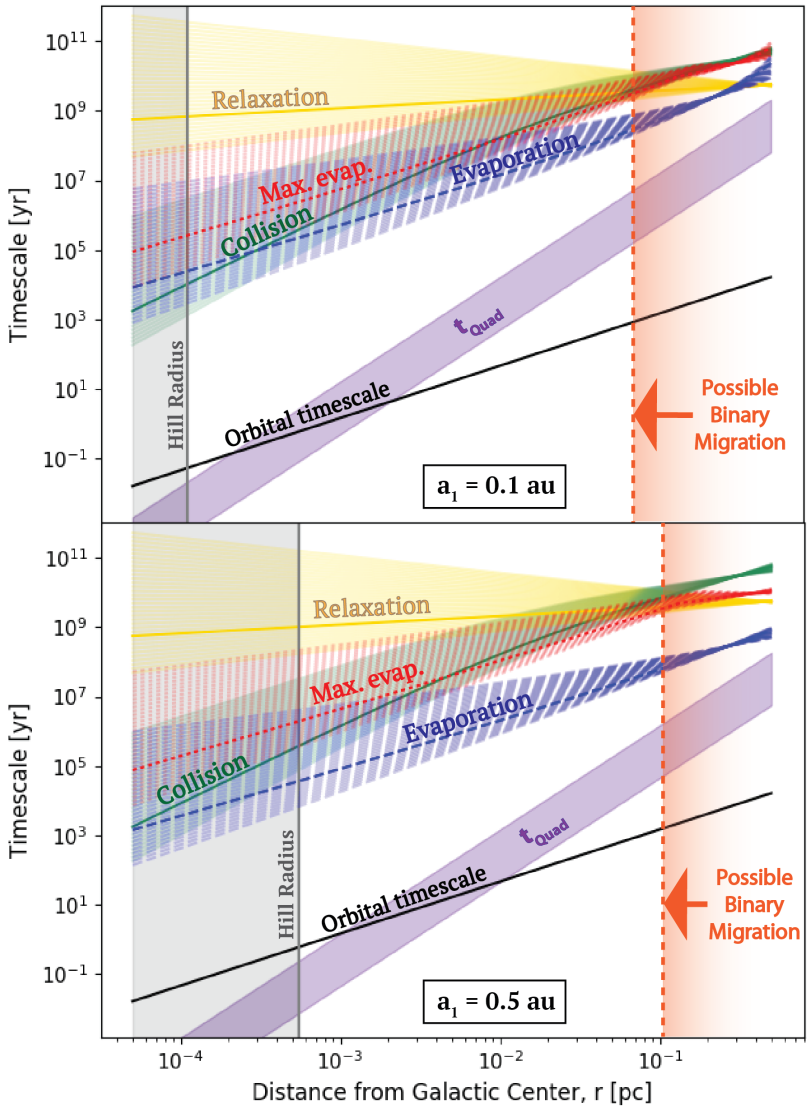

Figure 3.1: Two examples for the relevant timescales in the problem, as a function of the distance of the binary from the SMBH. We consider an equal mass binary with $M_{\rm bin} = 2M_\odot$ and semimajor axis 0.1 au and 0.5 au for the top and bottom panels, respectively. For the timescales that depend on the density, we consider a range of power laws from $\alpha = 1$ to $\alpha = 2$. All of the timescales increase with decreasing α. Relevant timescales include the evaporation timescale (dark blue), the evaporation timescale with the history parameter (red, labeled Max. Evap.), the relaxation timescale (gold), the collision timescale (green), and the EKL quadrupole timescale (purple). The darkest lines have $\alpha = 1.75$ (Bahcall & Wolf, 1976).

$a_{\rm bin}$. However, as $a_{\rm bin}$ increases with time, the evaporation timescale depends on when in its lifetime the binary is observed. The birth configuration, namely the initial $a_{\rm bin}$, should determine the true evaporation timescale of the system. Assuming that the binary began harder and softened over its lifetime places an upper limit on the evaporation time:

$$\begin{aligned} t_{ev,\max} &= t_{ev} S_h \\ &= \frac{\sqrt{3}\sigma(r_\bullet)}{32\sqrt{\pi} G \rho(r_\bullet) a_{\rm bin} \ln\Lambda(r_\bullet)} \frac{M_{\rm bin}}{\langle M_* \rangle} S_h \ , \end{aligned} \tag{3.8}$$

where

$$S_h = \frac{s_h}{s_0} \tag{3.9}$$

accounts for the binary's history, the widening the binary separation over time (Alexander & Pfuhl, 2014). We refer to S_h as the history parameter. s_0 is the the softness parameter calculated at present time, when the binary is observed. s_h finds the hardest possible initial configuration that the binary can have in order to place the most conservative overestimate on the evaporation time:

$$s_h = \min[1, s(a_{\rm bin} = R_1 + R_2)] \ , \tag{3.10}$$

where $R_{1,2}$ are the initial zero-main sequence radii of the stars, estimating the binary as a contact binary at the beginning of it's life (Alexander & Pfuhl, 2014). In other words, s_h chooses the tightest possible initial configuration to permit evaporation at birth, either a contact binary or at the limit for a soft binary, given by $s = 1$ (Eq. (3.7)).

Assuming the star's mass and the velocity dispersion have not changed over the binary's lifetime, the history parameter reduces to the ratio of the observed present day semimajor axis $a_{\rm bin}$ to the tightest possible initial semimajor axis $a_{\rm bin,min}$. Therefore, working from Eq. (3.8),

$$\begin{aligned} t_{\rm ev,max} &= t_{\rm ev}(a = a_{\rm bin}) \times \frac{a_{\rm bin}}{a_{\rm bin,min}} \\ &\approx t_{\rm ev}(a = a_{\rm bin,min}) \ . \end{aligned} \tag{3.11}$$

If we assume no mass loss due to stellar evolution and neglect any changes in the Coulomb logarithm, scaling by the history parameter is equivalent to simply calculating the evaporation timescale using the tightest possible configuration $a_{\rm bin,min}$.

We include a conservative maximum evaporation time (red) in Figure 5.1 by scaling the dark blue curves by factor S_h. The true evaporation time lies between these two curves.

3.2.1.2 Orbit Averaging

In the GC, the density and velocity dispersion depend on the distance from the SMBH, around which any binaries must also orbit. Therefore, the evaporation timescale also depends on the eccentricity of the binary's orbit about the SMBH. A binary on an eccentric orbit will pass through the denser, more energetic inner regions of the GC unlike a binary on a circular orbit with the same semimajor axis. To account for the eccentricity's effect, we average the contributions of each segment of the orbit. We weight each segment by the amount of time the binary spends there.

We consider a stellar binary with orbital parameters $a_{\rm bin}, e_{\rm bin}$ on an eccentric orbit about the Galactic Center. We refer to the stellar binary as the inner orbit. We define the outer orbit, that of the binary about the SMBH, to have orbital parameters $a_\bullet, e_\bullet$. Averaging over the outer orbit, we obtain the evaporation time as a function of orbital parameters $a_\bullet$ and $e_\bullet$. Specifically, we average over the canonical coordinate $M_\bullet$, the mean anomaly of the outer orbit:

$$t_{ev} \propto \frac{1}{2\pi}\int_0^{2\pi} \frac{r_\bullet^{\alpha-1/2}}{\ln\left(\beta/r_\bullet\right)} dM_\bullet. \tag{3.12}$$

However, to integrate, we make a coordinate transformation from the mean anomaly to the eccentric anomaly, $E_\bullet$, using

$$r_\bullet = a_\bullet(1 - e_\bullet \cos E_\bullet) \tag{3.13}$$

and $dM_\bullet = r_\bullet/a_\bullet dE_\bullet$.

We assume that the Coulomb Logarithm does not depend on $r_\bullet$, i.e. the logarithm changes very slowly and can be considered constant in the integral. We arrive at the integral:

$$t_{\rm ev} \propto \frac{1}{2\pi} \int_0^{2\pi} a_\bullet^{\alpha-1/2} \left(1 - e_\bullet \cos E_\bullet\right)^{\alpha+1/2} dE_\bullet \tag{3.14}$$

with the result $t_{\rm ev} \propto a_\bullet^{\alpha-1/2} \times f(e)$ where

$$\begin{aligned} f(e_\bullet) &= \frac{(1-e_\bullet)^{\alpha+\frac{1}{2}}}{2} {}_2F_1\left(\frac{1}{2}, -\frac{1}{2} - \alpha; 1; \frac{2e_\bullet}{e_\bullet - 1}\right) \\ &+ \frac{(1+e_\bullet)^{\alpha+\frac{1}{2}}}{2} {}_2F_1\left(\frac{1}{2}, -\frac{1}{2} - \alpha; 1; \frac{2e_\bullet}{e_\bullet + 1}\right) \end{aligned} \tag{3.15}$$

and ${}_2F_1$ is the hyper geometric function. Including the other parameters, we find that

$$t_{\rm ev} = \frac{\sqrt{3}\sigma(a_\bullet)}{32\sqrt{\pi}G\rho(a_\bullet)a_{\rm bin} \ln\Lambda(a_\bullet)} \frac{M_{\rm bin}}{\langle M_* \rangle} \times f(e_\bullet) \ , \tag{3.16}$$

where σ, ρ, and the Coulomb logarithm are all evaluated at $a_\bullet$. In Section 3.4.1, we rearrange this equation to obtain the maximum density at a distance $a_\bullet$ from the SMBH. Note that $f(e)$ is always of order unity, indicating that the eccentricity of an orbit about the SMBH makes little difference to the evaporation time. We remind the reader that the maximum evaporation timescale is achieved by multiplying Eq. (3.16) by the history parameter, S_h (see Eq. (3.8)).

In Figure 3.2, we plot the evaporation timescale as a function of eccentricity normalized by that of a circular orbit of the same semimajor axis. We vary the stellar density as a function of radius by using values of α from 0.5 to 2. Binaries on eccentric orbits have a longer evaporation timescale, and this effect becomes more pronounced with increasing α. This result indicates that the evaporation timescale for a binary on an eccentric outer orbit will have the same order of magnitude as the circular case. This minimal change stems from the fact that the binary will spend more time near the apoapsis of its orbit, offsetting the effects of reaching denser, more energetic regions closer to the SMBH. The environmental conditions at the distance $a_\bullet$ therefore give a good approximation of the evaporation time.

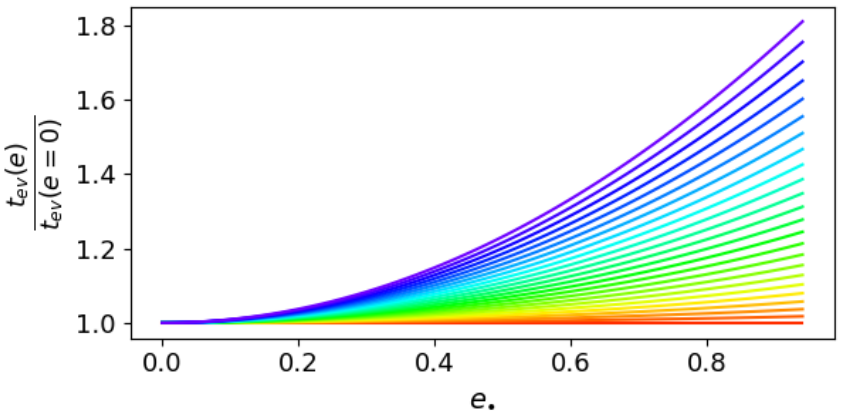

Figure 3.2: The evaporation time for a binary on an eccentric orbit with semimajor axis 1 au normalized by that of a circular orbit. We vary the density distribution of stars by assuming different values of α, from $\alpha = 0.5$ (red), which gives constant evaporation time, to $\alpha = 2$ (purple).

3.2.2 Two-Body Relaxation

The evaporation process requires that the maximum impact parameter must be about $a_{\rm bin}/2$ to ensure that the passerby interacts more strongly with one of the binary members as opposed to the binary center of mass. However, the interactions that fail to meet this criterion still impact the dynamical evolution of the binary. Interactions acting on the center of mass change the binary's overall trajectory. Over a relaxation time, these interactions alter the outer orbit.

For a single mass system, the two-body relaxation timescale can be written as:

$$t_{\rm relax} = 0.34 \frac{\sigma^3}{G^2 \rho \langle M_* \rangle \ln \Lambda_{\rm rlx}} \tag{3.17}$$

(Spitzer, 1987; Binney & Tremaine, 2008, Eq. (7.106)). We use this equation to gauge the timescale over which the orbit of the binary about the SMBH changes as $m_{\rm bin} \sim \langle M_* \rangle$ in this case. Additionally, the timescale over which the outer orbit changes through binary interactions with single stars is similar to the relaxation timescale (Hopman, 2009). Interactions at all impact parameters perturb the binary's trajectory about the SMBH, so the Coulomb logarithm in the relaxation timescale $\ln \Lambda_{\rm rlx}$ differs from that in the evaporation

timescale. The strongest deflection still gives $b_{\rm min}$. However, $b_{\rm max}$ becomes $r_\bullet$ to encompass all interactions from objects interior to the binary's orbit about the SMBH. In Figure 5.1, we plot the relaxation timescale for a variety of α in gold with the dark line representing $\alpha = 1.75$.

Perhaps more appropriate for binary systems is the mass segregation timescale, which also derives from the relaxation process and has a similar form to Eq. (5.7) (e.g., Bonnell & Davies, 1998; Spitzer, 1987; Merritt, 2006). Binary systems sink inwards according to their masses, which are higher on average than that of the surrounding objects (e.g., Mathieu & Latham, 1986; Geller et al., 2013; Antonini et al., 2014). The binary migrates towards the SMBH on the mass segregation timescale $t_{\rm seg} \approx \langle M_* \rangle / m_{\rm bin} \times t_{\rm relax}$ (e.g., Merritt, 2006). For more massive systems, we use this equation to calculate the timescale over which the outer orbit changes.[5]

3.2.3 Inelastic Collisions

In a dense environment like the GC, direct collisions between objects occur frequently. Accounting for gravitational focusing, the collision rate can be expressed as:

$$t_{\rm coll}^{-1} = 16\sqrt{\pi}\frac{\rho(r_\bullet)\sigma(r_\bullet)}{\langle M_* \rangle} R_j^2 \left(1 + \frac{v_{\rm esc}^2}{\sigma(r_\bullet)^2}\right), \tag{3.18}$$

where $v_{\rm esc} = \sqrt{2Gm_j/R_j}$ is the escape speed from one of the stars in the binary with mass (radius) m_j (R_j) (Binney & Tremaine, 2008, Eq. (7.195)). For a soft binary, we treat the collision separately from the evolution of the orbit. The primary will suffer a collision sooner than the less massive companion because of its enhanced cross-section. Therefore,

[5]We focus on changes to the energy of the outer orbit, which affects the semimajor axis, through two-body relaxation. However, resonant relaxation processes also take place, altering the outer orbit's angular momentum magnitude and orientation (e.g., Rauch & Tremaine, 1996; Hopman & Alexander, 2006a; Kocsis & Tremaine, 2011). Since the collision and evaporation timescales depend weakly on eccentricity (Figures 2 and 3), scalar resonant relaxation, which changes the angular momentum vector's magnitude, does not impact our procedure. Similarly, vector resonant relaxation, which changes the outer orbit's inclination, also does not affect our procedure, although it can help the system enter the EKL-favored regime (e.g., Hamers et al., 2018).

we calculate the collision timescale using the primary star. We plot this timescale in green in Figure 5.1.

To find the collision timescale for a star on an eccentric orbit about the SMBH, we average the collision rate Eq. (3.18) over the mean anomaly similar to Eq. (3.12). After a coordinate transformation to the eccentric anomaly $E_\bullet$, over which we integrate, the collision rate for an eccentric orbit becomes

$$\begin{aligned} t_{\rm coll}^{-1} &= 16\sqrt{\pi}\frac{\rho(a_\bullet)\sigma(a_\bullet)}{\langle M_*\rangle}R_j^2 \\ &\times \left(f_1(e_\bullet) + f_2(e_\bullet)\frac{v_{\rm esc}^2}{\sigma(a_\bullet)^2}\right), \end{aligned} \tag{3.19}$$

where

$$\begin{aligned} f_1(e_\bullet) &= \frac{(1-e_\bullet)^{\frac{1}{2}-\alpha}}{2}{}_2F_1\left(\frac{1}{2},\alpha-\frac{1}{2};1;\frac{2e_\bullet}{e_\bullet-1}\right) \\ &+ \frac{(1+e_\bullet)^{\frac{1}{2}-\alpha}}{2}{}_2F_1\left(\frac{1}{2},\alpha-\frac{1}{2};1;\frac{2e_\bullet}{e_\bullet+1}\right) \end{aligned} \tag{3.20}$$

and

$$\begin{aligned} f_2(e_\bullet) &= \frac{(1-e_\bullet)^{\frac{3}{2}-\alpha}}{2}{}_2F_1\left(\frac{1}{2},\alpha-\frac{3}{2};1;\frac{2e_\bullet}{e_\bullet-1}\right) \\ &+ \frac{(1+e_\bullet)^{\frac{3}{2}-\alpha}}{2}{}_2F_1\left(\frac{1}{2},\alpha-\frac{3}{2};1;\frac{2e_\bullet}{e_\bullet+1}\right). \end{aligned} \tag{3.21}$$

Figure 3.3 shows the collision timescale as a function of eccentricity normalized by that of a circular orbit. The density has values of α ranging from 0.5 (red) to 2 (purple). Increasing the eccentricity increases the average collision rate, decreasing the collision timescale. The change becomes more pronounced for steeper density profiles but does not exceed a factor of two. As in Section 3.2.1.2, we attribute this minimal change to the conditions near periapsis and apoapsis offsetting the other's impact.

Eq. (3.18) assumes that stars of equal mass compose the population, and its derivation involves averaging over the velocity distribution of the stars. In later sections, we violate

this assumption by considering a massive star with less massive surrounding objects. We can estimate the collision timescale in this scenario using a simple $t_{\rm coll}^{-1} = n\sigma A$ calculation. The cross-section of interaction A equals πb^2, where b is the maximum impact parameter for a physical collision. Accounting for gravitational focusing,

$$b^2 = r_c^2 + r_c \frac{2GM_t}{\sigma^2} \ , \tag{3.22}$$

where r_c is the sum of the radii of the interacting stars, $R_j + \langle R_* \rangle$, and $M_t = m_j + \langle M_* \rangle$. We estimate that the collision rate is

$$t_{\rm coll}^{-1} = \frac{\pi\rho\sigma}{\langle M_* \rangle} \left(r_c^2 + r_c \frac{2GM_t}{\sigma^2} \right) \ . \tag{3.23}$$

In the limit that all stars are identical, we set $r_c = 2R_j$ to find that Eq. (3.18) is only a factor of two bigger than Eq. (3.23). This comparison suggests that averaging over the velocity distribution introduces a small numerical factor, increasing the collision rate. Averaging Eq. (3.23) over the eccentricity results in a very similar equation to Eq. (3.19):

$$\begin{aligned} t_{\rm coll}^{-1} &= \frac{\pi\rho(a_\bullet)\sigma(a_\bullet)}{\langle M_* \rangle} \\ &\times \left(f_1(e_\bullet) r_c^2 + f_2(e_\bullet) r_c \frac{2GM_t}{\sigma(a_\bullet)^2} \right) \ . \end{aligned} \tag{3.24}$$

3.2.4 Eccentric Kozai-Lidov Timescale

Any binary system in the GC forms a triple system with the SMBH. Dynamical stability requires that this triple has a hierarchical configuration: the binary must have a much tighter (inner) orbit than that of its center of mass about the SMBH, referred to as the outer orbit. The condition $a_{\rm bin} << a_\bullet$ allows an expansion of the gravitational potential in terms of the small parameter $a_{\rm bin}/a_\bullet$ (Kozai, 1962; Lidov, 1962). The SMBH perturbs the binary's orbit, causing the eccentricity and inclination of the stellar binary to oscillate in the Eccentric Kozai-Lidov (EKL) Mechanism (see the review Naoz, 2016). The quadrupole term in the expansion has an associated timescale, which represents the timescale of the oscillations:

$$t_{\rm EKL,quad} = \frac{16}{30\pi} \frac{M_{\rm bin} + M_\bullet}{M_\bullet} \frac{P_\bullet^2}{P_{\rm bin}} \left(1 - e_\bullet^2\right)^{3/2} , \tag{3.25}$$

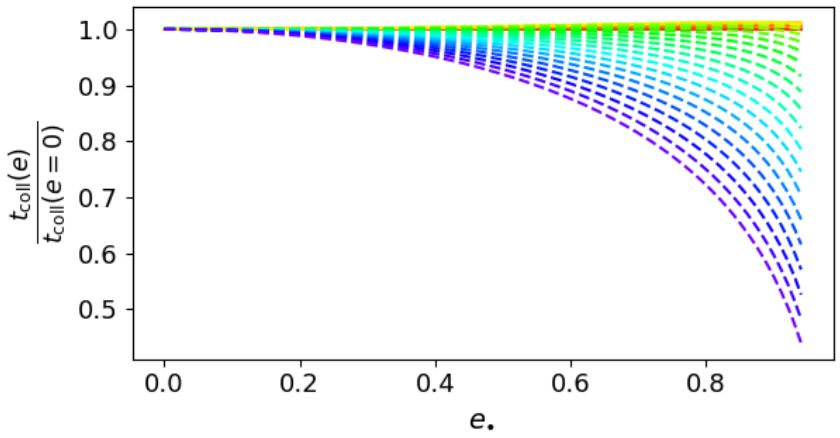

Figure 3.3: The collision timescale for a star on an eccentric orbit about the SMBH normalized by that of a circular orbit. We vary the density distribution of stars by assuming different values of α, from $\alpha = 0.5$ (red) to $\alpha = 2$ (purple).

where $P_{\rm bin}$ ($P_\bullet$) denotes the period of the inner (outer) orbit (e.g., Antognini, 2015; Naoz, 2016). We plot a range of quadrupole timescales in purple for $e_\bullet = 0$ to $e_\bullet = 0.95$ in Figure 5.1.

These EKL oscillations can result in one of several outcomes. The oscillations can drive the eccentricity to extreme values and cause the inner binary to merge (e.g., Antonini & Perets, 2012; Naoz & Fabrycky, 2014; Stephan et al., 2016; Hoang et al., 2018; Rose et al., 2019; Fragione & Antonini, 2019). Similarly, weak encounters with a passing object may change the eccentricity of the binary and result in a merger (e.g. Hamers & Samsing, 2019; Samsing et al., 2019; Michaely & Perets, 2019; Young & Hamers, 2020). Stephan et al. (2016) estimates that after a few Gyr, 30 per cent of a GC binary population will have merged through the EKL mechanism. However, if tides work efficiently during these periods of high eccentricity, the binary orbit may instead tighten and circularize (e.g., Naoz & Fabrycky, 2014; Rose et al., 2019). Yet another possibility is that the system undergoes weak eccentricity oscillations (e.g., Rose et al., 2019).

3.3 The Outcome: Relax, Evaporate, or Collide?

A competition between several processes determines the dynamical fate of a binary. We consider two examples in Figure 5.1. Both of the binaries in the figure are equal mass with $M_{\rm bin} = 2\,M_\odot$. Their semimajor axes differ by a factor of 5 to illustrate the relationship between these competing timescales and the softness of the binary. These binary parameters ensure that the systems are both long-lived and soft enough to undergo evaporation throughout most of the inner region $r \leq 0.5$ pc of the GC.

Figure 5.1 indicates that most soft binaries will evaporate before one of the binary members collides with a passerby. However, within about 10^{-2} pc of the SMBH, those systems that approach the boundary $s = 1$, given by Eq. (3.7), may undergo an inelastic collision before the system has had time to evaporate. We reserve a detailed examination of this outcome for future study. Additionally, for most of inner parsec of the GC, the evaporation timescale is shorter than the relaxation timescale, implying that the binary will evaporate before it can migrate closer to the SMBH. However, for both of the examples, as $r_\bullet$ approaches 0.5 pc, the relaxation timescale becomes shorter than the evaporation timescale. Here, a binary migrates inward before it unbinds.

The examples in Figure 5.1 assume that the binary has a circular orbit about the SMBH. The collision timescale decreases with the eccentricity $e_\bullet$ (Figure 3.3), while the evaporation timescale increases (Figure 3.2). An eccentric orbit will increase the range of distances from the SMBH over which $t_{\rm coll} < t_{\rm ev}$. Additionally, eccentric orbits have a shorter relaxation timescale than circular orbits of the same semimajor axis (Sari & Fragione, 2019). Therefore, the relaxation and evaporation timescales will cross closer to the SMBH for eccentric orbits, increasing the parameter space in which the binary migrates before it evaporates.

Figure 3.4 illustrates the qualitative evolutionary trajectories for a binary system depending on its initial semimajor axis $a_{\rm bin}$. This binary resides 0.3 pc from the SMBH and is an equal

mass system with $M_{\rm bin} = 2\,M_{\odot}$. We consider three qualitative examples. In the case (a), the binary with $a_{\rm bin} \lesssim 0.05$ au has a hard configuration. This tight binary will migrate towards the SMBH. The hard binary becomes harder from frequent interactions with nearby objects (e.g., Heggie, 1975). The system may harden to the point where it crosses the Roche Limit, or the EKL mechanism may drive the system to merge (e.g., Stephan et al., 2016, 2019; Rose et al., 2019). The system may also have an exchange interaction with another star (e.g. Hopman, 2009). We estimate that this system's exchange interaction timescale is approximately $0.8 \times t_{\rm rlx}$ or 4×10^9 yr (Eq. (43) from Hopman, 2009).

For scenario (b), the case $0.05 \lesssim a_{\rm bin} \lesssim 0.1$ au, the binary is marginally soft. It evaporates over a timescale longer than the relaxation timescale, allowing the system to move inwards over its lifetime. It will eventually evaporate at a closer distance to the SMBH than the location of its birth. The inward migration brings the binary into a comparatively denser region, where the evaporation timescale is shorter. The coupling of the relaxation and evaporation processes may therefore result in a puzzling binary, one whose age and location suggest that it should have already evaporated. Such a system owes its longevity to originating in a less dense region further from the SMBH.

Finally, case (c) has $0.1\,{\rm au} \lesssim a_{\rm bin}$. The evaporation process has a shorter timescale compared to other dynamical processes. The system will unbind due to weak interactions with neighbors. In both soft binary cases, (b) and (c), the system may also merge through the EKL mechanism.

To assess the outcomes in a population of binaries, we generate 70000 stable systems in the GC using similar parameter distributions to Stephan et al. (2016) (see Appendix 3.7.1). About 99 per cent of these systems are soft. Only about 3 per cent of these soft systems experience a collision while the binary is still bound. Using the mass segregation timescale, we estimate that up to 10 per cent of the binaries drift inwards before they unbind (see Appendix 3.7.3 and Figure 3.11). These systems tend to be tighter binaries that reside further

from the SMBH. These demographics suggest that mass segregation plays a secondary role to evaporation in shaping the distribution of binaries in the GC, in particular the binary fraction as a function of distance from the SMBH. The vast majority of systems are soft and unbind over shorter timescales. As shown previously using EKL simulations with evaporation in the GC (e.g., Stephan et al., 2016; Hoang et al., 2018), we expect a dearth of binaries closer to the SMBH, a trend that will become more pronounced over time.

3.4 Constraining the dark cusp and the binary parameters

We build upon the framework presented in Alexander & Pfuhl (2014) which uses a binary to provide density and relaxation time constraints on the dark cusp in the GC. The evaporation timescale relates key binary and GC properties. Section 3.3 shows that most binaries in the GC are susceptible to evaporation. Eq. (3.16) presents a unique opportunity to use a set of known parameters to constrain unknown properties. A confirmed binary can thereby be used to probe the density at the GC. On the other hand, a constraint on the density some distance from the SMBH informs the allowable properties of any hypothetical binary system in that vicinity. We explore these relations in the context of an old and a young binary.

3.4.1 Galactic Center Stellar Density

The evaporation timescale relates binary properties and the density. The age of the system sets a lower limit on the evaporation timescale: the binary would not be observed if the evaporation timescale were shorter than the system's age. Therefore, a confirmed binary provides an upper limit on the density in its vicinity. Setting $t_{\rm age} = t_{\rm ev}$, we can rearrange Eq. (3.16) to find $\rho_{\rm max}$ at the distance $a_\bullet$ from the SMBH:

$$\rho_{\rm max,ev} = \frac{\sqrt{3}}{32\sqrt{\pi}G} \frac{\sigma(a_\bullet)}{a_{\rm bin} \ln \Lambda(a_\bullet)} \frac{1}{t_{\rm age}} \frac{M_{\rm bin}}{\langle M_* \rangle} f(e_\bullet). \tag{3.26}$$

Note that we do not assume a constant Coulomb logarithm.

Collisions may also unbind the binary system (e.g., Sigurdsson & Phinney, 1993; Fregeau

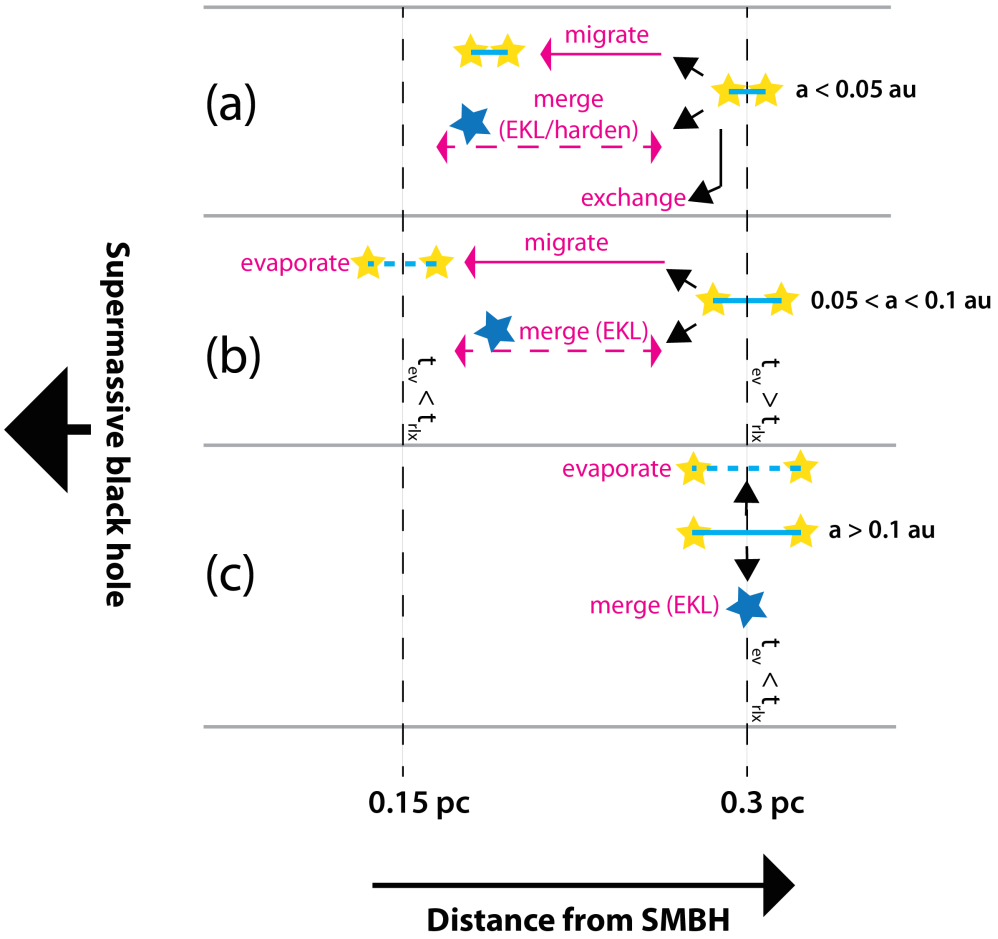

Figure 3.4: We chart qualitative evolutionary possibilities for a $M_{\rm bin} = 2\,M_\odot$ binary system at 0.3 pc from the SMBH depending on its initial semimajor axis, depicted by the blue lines. A dashed blue line indicates a binary that has evaporated. We explore three cases, labeled (a), (b), and (c). Each case corresponds to a row, separated by the light grey solid lines. The shortest timescale at the binary's location determines its fate. The binary migrates when $t_{\rm relax} < t_{\rm ev}$. Note that in scenario (a), the binary is too hard to evaporate. The collision timescale for these systems is too long to alter the qualitative evolution. In all cases, a merger represents a possible outcome. Blue stars symbolize a merger product. Numerical values are approximate in this qualitative illustration.

et al., 2004). A collision can ionize the binary if the incoming star has velocity greater than the critical velocity

$$v_{\rm crit} = \left[\frac{G(M_{\rm bin}+m_3)}{M_{\rm bin}m_3}\left(\frac{m_1 m_2}{a_{\rm bin}}\right)\right]^{1/2}, \tag{3.27}$$

where $M_{\rm bin} = m_1 + m_2$ and m_3 is the mass of the incoming neighbor (Fregeau et al., 2004). We take m_3 to be $\langle M_* \rangle$. We assume that wherever $\sigma > v_{\rm crit}$, a collision will unbind the binary. Therefore, setting $t_{\rm coll} = t_{\rm age}$ provides another density constraint. We can rearrange the collision timescale Eq. (3.18) to obtain an upper limit on the density at $a_\bullet$:

$$\begin{aligned}\rho_{\rm max,coll} &= \frac{\langle M_* \rangle}{\pi\sigma(a_\bullet)}\frac{1}{t_{\rm age}} \\ &\times \left(f_1(e_\bullet)r_c^2 + f_2(e_\bullet)r_c\frac{2GM_{\rm t}}{\sigma(a_\bullet)^2}\right)^{-1},\end{aligned} \tag{3.28}$$

where $M_{\rm t} = m_1 + \langle M_* \rangle$. We use the primary mass in this calculation because the more massive star will undergo a collision sooner. Above this density limit, the primary has likely already collided with a passing star, ionizing the system.

The maximum density constraints depend on the average mass of the objects interacting with the binary. Based on work in Alexander & Hopman (2009), Alexander & Pfuhl (2014) present two equations for $\langle M_* \rangle$ as a function of distance from the SMBH. One equation corresponds to a top-heavy initial mass function, while the other derives from a universal initial mass function (IMF). In the former case, $\langle M_* \rangle$ is approximately $10\,M_\odot$ over the range of distances we consider, while the latter equation gives an $\langle M_* \rangle$ ranging from 1 to $2\,M_\odot$. At 0.15 pc, where the known binary IRS 16NE resides, $\langle M_* \rangle$ equals $1.2\,M_\odot$ for the universal IMF (Alexander & Pfuhl, 2014).

We present a proof of concept for hypothetical young and old binary systems using these density constraints (Figure 3.5). For these systems, we adopt a circular orbit around the SMBH, such that $f(e) \to 1$. We consider two cases for $\langle M_* \rangle$. In the first case, we simply adopt $\langle M_* \rangle = 1.2\,M_\odot$. In the second case, we consider $\langle M_* \rangle = 10\,M_\odot$ to reflect Alexander

& Pfuhl (2014)'s top-heavy IMF. We assume that $10\,M_\odot$ main-sequence stars dominate the surrounding objects and adopt a radius of approximately $3.5\,R_\odot$ for these objects to calculate the collision density constraint. However, the top heavy IMF is most relevant within ~ 0.01 pc of the SMBH, where an abundance of stellar mass black holes may result in an $\langle M_* \rangle$ closer to $10\,M_\odot$ (Freitag et al., 2006; Alexander & Hopman, 2009). The collisional radius is much smaller for stellar mass black holes. While we restrict ourselves to an $\langle M_* \rangle$ that remains constant throughout the GC, this procedure can incorporate an $\langle M_* \rangle$ that varies as a function of distance from the SMBH with the form $\langle M_* \rangle \propto r_\bullet^{-\beta}$. This change will alter the orbit-averaged result (Section 3.2.1.2). However, the result should still have the form of a hypergeometric function. We expect that the eccentricity dependence will remain weak.

3.4.1.1 The Cusp and Young Binaries

We adopt parameters $M_{\rm bin} = 80 M_\odot$ and $a_{\rm bin} = 3.11$ for the confirmed binary system IRS 16NE (Pfuhl et al., 2014; Alexander & Pfuhl, 2014). Like Alexander & Pfuhl (2014), we assume an age of 6 Myr for the system, consistent with observations of the young GC stellar population (e.g., Paumard et al., 2006; Bartko et al., 2009; Lu et al., 2013). While IRS 16NE resides at $a_\bullet = 0.15$ pc (see Figure 3.5, black dashed vertical line), we place limits on the density over a range of distances from the SMBH using a IRS 16NE-like binary in the first row of Figure 3.5.

In conjuction with the known binary parameters, setting $t_{\rm ev} = t_{\rm age}$ gives an upper limit on the density in the binary's vicinity using Eq. 3.26 (solid multicolored curve; see lower right plot for labels). We scale this density limit by the history parameter to arrive at a conservative maximum density (dashed multicolored curve). The history parameter assumes that the binary has been softening over its lifetime from the tightest possible initial configuration. This density constraint is only valid where the binary is soft enough to evaporate. Gautam et al. (in prep) find that IRS 16NE is a hard binary at 0.15 pc. For the case $\langle M_* \rangle = 1.2\,M_\odot$, a binary with the parameters $a_{\rm bin}$, $M_{\rm bin}$ of IRS 16NE only becomes soft in the inner 0.01

pc, where the velocity dispersion is higher. We shade the region where the binary is hard in gray. The left limit of this region depends on the velocity dispersion and therefore α. However, to avoid over-cluttering the figure, we simply mark the region as beginning where the binary becomes hard for $\alpha = 2$ (blue).

Similarly, we plot the maximum density constraint from collisions (Eq. (3.28)) in black. The solid segment of the curve coincides with the region in which the neighboring stars have sufficient energy to ionize the system; the velocity dispersion is greater than the critical velocity. The dashed portion indicates the density at which the primary has undergone a collision that may alter the binary configuration while leaving the system bound. The dashed segment therefore cannot constrain the density.

The maximum density constraint is set by either the collision or evaporation timescale, whichever falls lower. We can rule out densities above this threshold. More specifically, we can eliminate certain density power laws of the form Eq. 5.1 (faded solid lines) with $\alpha = 1$ (red) to $\alpha = 2$ (blue) that lie above the $\rho_{\rm max}$ curve. We shade the forbidden density region in Figure 3.5.We note that if the $10\,M_\odot$ case is dominated by stellar mass black holes as opposed to main sequence stars, the collision timescale becomes very long compared to the evaporation timescale. In this case, the evaporation timescale would set the density constraint in Figure 3.5.

3.4.1.2 The Cusp and Old Binaries

An older binary places a more stringent constraint on the maximum density than the young system. Given the dearth of confirmed binaries, we use a hypothetical older binary with the same parameters as the lower panel of Figure 5.1: $m_1 = m_2 = 1\,M_\odot$ and $a_{\rm bin} = 0.5$ au. In the orange shaded region, the relaxation timescale exceeds the evaporation timescale, allowing the binary to migrate inward before it has evaporated and placing a caveat on a density

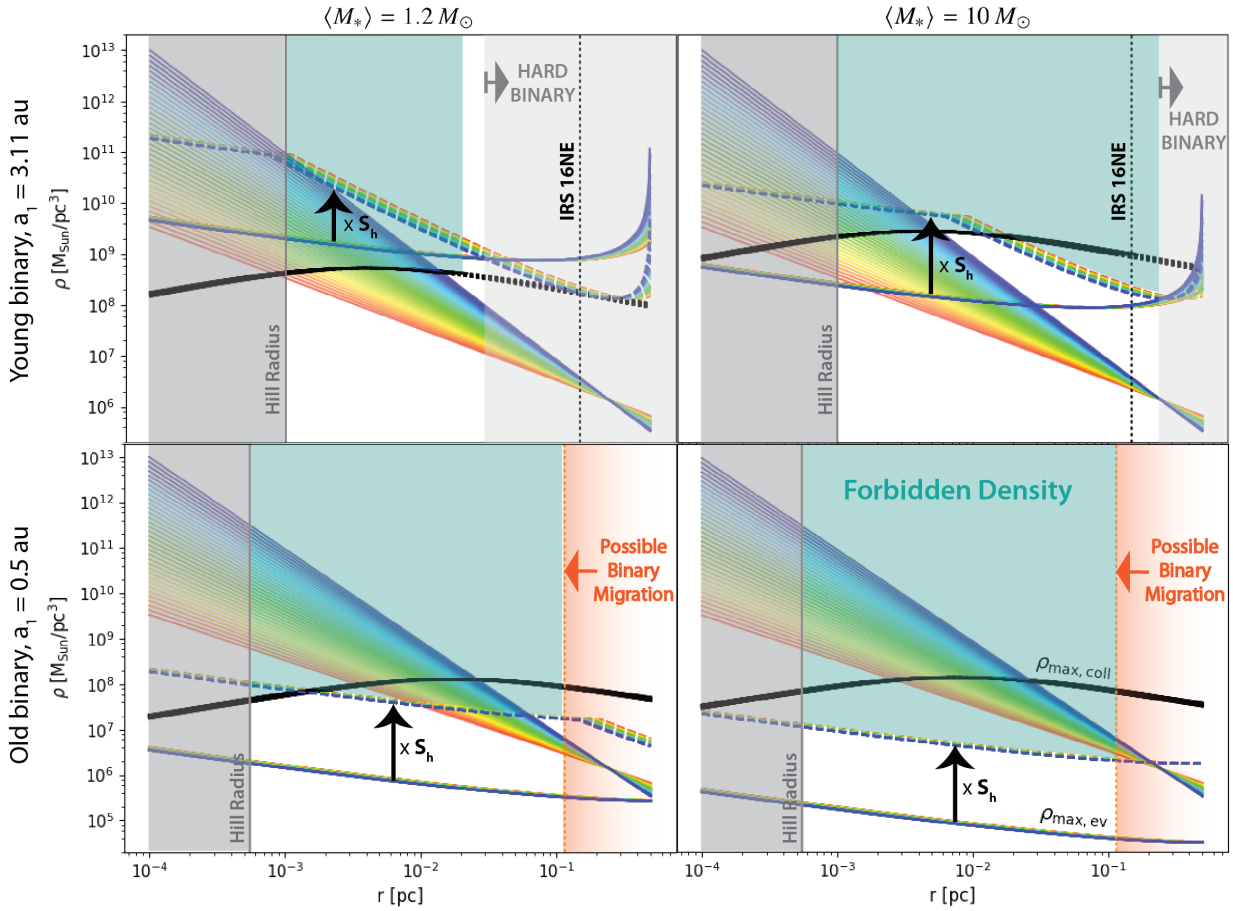

Figure 3.5: Given a binary, we plot the maximum density for no evaporation as a function of distance from the SMBH with (colorful dashed) and without (colorful solid) the history parameter S_h, given by Eq. (3.8) and (3.9). The black curve depicts the maximum density for no collision. The solid portion of the curve denotes the region in which the velocity dispersion is greater than the critical velocity to ionize the binary. The dashed black segment cannot constrain the density. Solid faded lines indicate the density as a function of r assuming a power law like Eq. 5.1 for $\alpha = 1$ (red) to $\alpha = 2$ (blue). The left (right) column assumes $\langle M_* \rangle = 1.2\,M_\odot$ ($\langle M_* \rangle = 10\,M_\odot$). See the note at the end of Section 3.2.1 about the x-axes limits, which we extend to extreme values. **Upper Row: Young Massive Binary** This binary has the parameters of IRS 16NE from Alexander & Pfuhl (2014). **Lower Row: Old Binary** This binary is identical to the system used in the lower panel of Figure 5.1: a 1 Gyr old equal mass binary with $1\,M_\odot$ stars and 0.5 au separation. Approaching 0.5 pc, the evaporation timescale exceeds the relaxation timescale, allowing inward migration. These density constraints imply that the detection of an older binary close to the SMBH may suggest a recent dynamical formation scenario.

constraint derived from the system.[6] However, the left boundary of that region is determined by assuming the binary has evolved from the tightest possible initial configuration. Therefore, it likely overestimates the true region in which a given binary migrates more quickly than it evaporates. We plot $\rho_{\rm max,ev}$ with (dashed dark line) and without (solid dark line) the history parameter. The black dashed curve represents $\rho_{\rm max,coll}$ from Eq. (3.28). For this long-lived, less massive binary, collisions do not play a significant role in its evolution. Over most of the GC, the binary evaporates before it experiences an inelastic collision.

In Figure 3.5, we illustrate our interpretation of the plot by shading the region of forbidden density in teal. The maximum density can be compared to the density power laws of the form Eq. 5.1 (faded solid lines) with $\alpha = 1$ (red) to $\alpha = 2$ (blue). Within ~ 0.01 pc of the SMBH, all density power laws lie above the $\rho_{\rm max}$ for binary survival. We conclude that old binaries cannot survive within ~ 0.01 pc of the SMBH. The discovery of a soft, old binary in that region may indicate a dynamical formation mechanism.

3.4.2 The Binary Separation

Similar to the maximum density constraint, we can solve Eq. (3.16) for $a_{\rm bin}$ to find the maximum separation a binary can have at a certain age by setting $t_{ev} = t_{\rm age}$:

$$a_{\rm bin,max} = \frac{\sqrt{3}}{32\sqrt{\pi}G} \frac{\sigma(r_\bullet)}{\rho(r_\bullet) \ln \Lambda} \frac{1}{t_{\rm age}} \frac{M_{\rm bin}}{\langle M_* \rangle}. \tag{3.29}$$

A binary wider than $a_{\rm bin,max}$ would have already evaporated. We assume that the Coulomb logarithm, which depends on $a_{\rm bin}$, is approximately constant and use a value of 5 based on Figure 3.10. We also assume that $\langle M_* \rangle = 1.2\, M_\odot$ for the remainder of this paper.

In this exercise, we are considering the maximum allowed separation after $t_{\rm age}$ years of evolution. We do not take the history parameter into account because it assumes the tightest

[6] Tidal breakup of a triple or quadrupole system can also deliver binary systems from farther out in the GC (Fragione & Gualandris, 2018; Fragione, 2018). These systems would similarly provide unreliable density constraints.

possible initial separation for the binary. Evolution from this tight state can only lead to an observed separation shorter then the one presented in Eq. (3.29). We also neglect collisions because the collision rate does not depend on the binary semimajor axis. However, a star in these hypothetical binaries may meet the condition $t_{\rm coll} \leq t_{\rm age}$ closer to the SMBH, where the velocity dispersion is high, unbinding the binary. While collisions may act faster than evaporation close to the SMBH, they do not lead to a wider maximum binary separation.

3.4.2.1 Young Binary Separation

In Figure 3.6, we consider three young binaries. Two have the same masses as the nominal systems from Section 3.4.1: one with $m_1 = m_2 = 1\,M_\odot$ and another with $m_1 = m_2 = 40\,M_\odot$. We also include a binary with $m_1 = 10\,M_\odot$ and $m_2 = 1\,M_\odot$, similar to the parameters in Section 3.5 where we consider hypothetical binaries in place of S-stars. The dashed colored lines depict the semimajor axis that these young binaries can have as a function of distance from the SMBH for $\alpha = 1$ (red) to $\alpha = 2$ (blue). Above this curve, the binary would have already evaporated within its lifetime. The solid lines, also colored by α, represent the minimum semimajor axis the binary can have while remaining susceptible to evaporation. Below this line, the binary is too hard to evaporate. We also plot the limit at which the binary will succumb to tidal forces from the SMBH and become unbound and the limit at which the binary will cross its own Roche limit to undergo mass transfer, labeled the binary Roche limit.

3.4.2.2 Old Binary Separation

Similarly, we plot the maximum a_1 (dashed colored lines) for a 1 Gyr-old binary with $m_1 = m_2 = 1\,M_\odot$ using to Eq. (3.29). Unlike the young binary examples, we omit high-mass stars because they evolve on shorter timescales. As expected, only a narrow range of $a_{\rm bin}$ remains allowable for older systems. Observing an old binary between 0.0025 pc $\lesssim r_\bullet \lesssim$ 0.07 pc may help disentangle the possible power-law index, α, of the underlying density. Additionally,

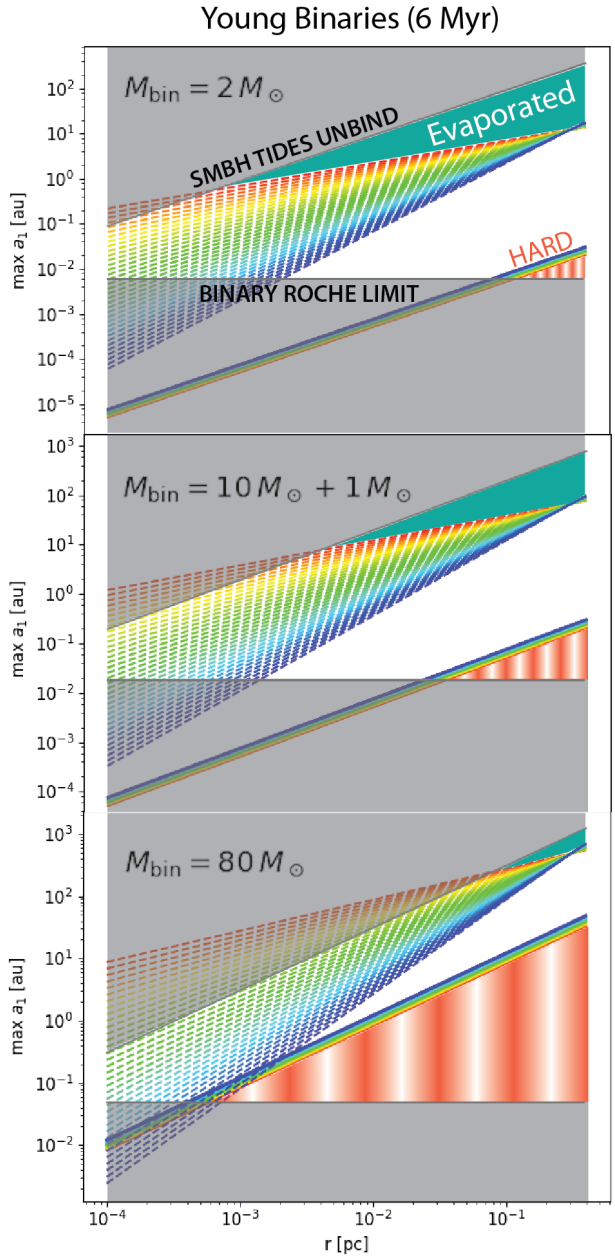

Figure 3.6: We consider $M_{\rm bin} = 2, 11$ and 80 $M_\odot$ from top to bottom, and estimate the maximum separation after 6.6 Myr, according to Equation (3.29), assuming a constant Coulomb logarithm. This maximum semimajor axis as a function of the binary distance form the SMBH is depicted by the colorful dashed lines, where as in previous figures, we vary α from 1 (red) to 2 (blue). Above this line the binary should have been evaporated (teal area). Following the same color convention, we also plot the minimum semimajor axis the binary can have to be considered soft and undergo evaporation. Below this line the binary is hard (shaded with red stripes). We shade in grey the regime at which the inner binary will cross it's own Roche limit (see Eq. (3.32)) and the regime at which the SMBH will tidally disrupt and unbind the binary (see Eq. (3.30), where for simplicity we assumed $e_\bullet, e_{\rm bin} \to 0$). Note the different limits on the y-axis due to the different masses. See the note at the end of Section 3.2.1 about the x-axes limits.

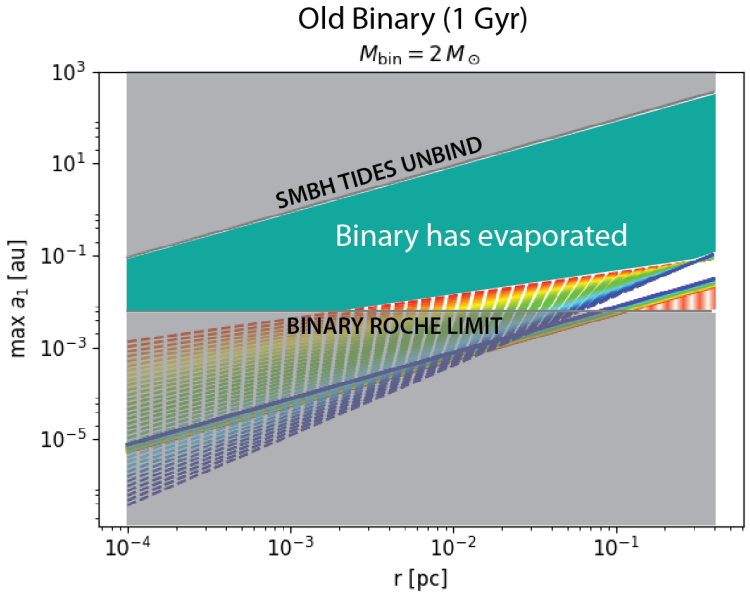

Figure 3.7: Assuming a constant Coulomb logarithm, the dashed lines indicate the maximum semimajor axis a 1 Gyr-old binary $2\,M_\odot$ can have to survive at a certain distance from the SMBH. As in previous figures, we vary α from 1 (red) to 2 (blue). We also plot the minimum semimajor axis (solid lines) the binary can have to be considered soft and undergo evaporation. The grey regions represent parameter space excluded either because the binary would be tidally unbound by the SMBH or the stars would undergo mass transfer. The binary is too hard to evaporate in the red striped region. See the note at the end of Section 3.2.1 about the x-axes limits, which we extend to extreme values.

observing an old binary within $\sim$ 0.0025 pc of the SMBH may suggest a new, perhaps dynamically formed system.

3.5 The S-Star cluster

While few confirmed binaries exist in the GC, observational evidence indicates their presence. We consider the possibility that observed stars in the GC are embedded in a binary system. Several S-stars have eccentric orbits about the SMBH within 0.05 pc (e.g., Ghez et al., 2005; Gillessen et al., 2009, 2017), and observations indicate that many of these stars are young (e.g., Paumard et al., 2006; Lu et al., 2009; Bartko et al., 2009; Habibi et al., 2017).[7] Previous studies explore the alternative that these stars, namely S0-2, may in fact represent binary

[7]The S-star population also contains some older stars (e.g. Habibi et al., 2019).

systems and assess their possible orbital configurations (e.g., Li et al., 2017; Chu et al., 2018). The procedure presented here may also constrain the parameter space of the hypothetical binary's orbital configuration.

In particular, we consider as a proof of concept three well studied S-stars, S0-1, S0-2, and S0-5 and constrain the allowable semi-major axis and local density (Figure 3.8). A future observational constraint on the density will narrow the range of allowable binary semi-major axis, while a confirmed detection of an S-star binary system will place limits on the density. Radial velocity measurements in particular can provide constraints on the semimajor axes and companion masses of potential S-star binaries (Chu et al. in prep.).

We impose several conditions to ensure that each hypothetical binary is dynamically stable and long-lived. These criteria place upper and lower limits on $a_{\rm bin}$. First, we consider the Hill Radius for a three-body system. This condition requires that the stellar binary's apoapse distance $a_{\rm bin}(1+e_{\rm bin})$ does not exceed the Hill radius:

$$a_{\rm bin}(1+e_{\rm bin}) < a_\bullet(1-e_\bullet)\left(\frac{m_1}{3M_\bullet}\right)^{1/3} , \tag{3.30}$$

(e.g., Naoz & Silk, 2014). We assume that the hypothetical stellar binary orbit is circular. An eccentric orbit will at most change the maximum $a_{\rm bin}$ by a factor of two. The vertical blue line, labeled accordingly, marks this upper limit in Figure 3.8.

We also impose a hierarchical configuration: the (hypothetical) stellar binary must have a much tighter configuration than the orbit of its center of mass about the SMBH. The SMBH graviationally perturbs the stellar binary and alters its orbital properties. To ensure that these changes are secular and the system is dynamically stable, the parameter ϵ, which represents the pre-factor in the three body Hamiltonian, cannot exceed 0.1:

$$\epsilon = \frac{a_{\rm bin}}{a_\bullet}\frac{e_\bullet}{1-e_\bullet^2} < 0.1 . \tag{3.31}$$

(e.g., Lithwick & Naoz, 2011; Naoz, 2016). The vertical red line indicates this limit in Figure 3.8.

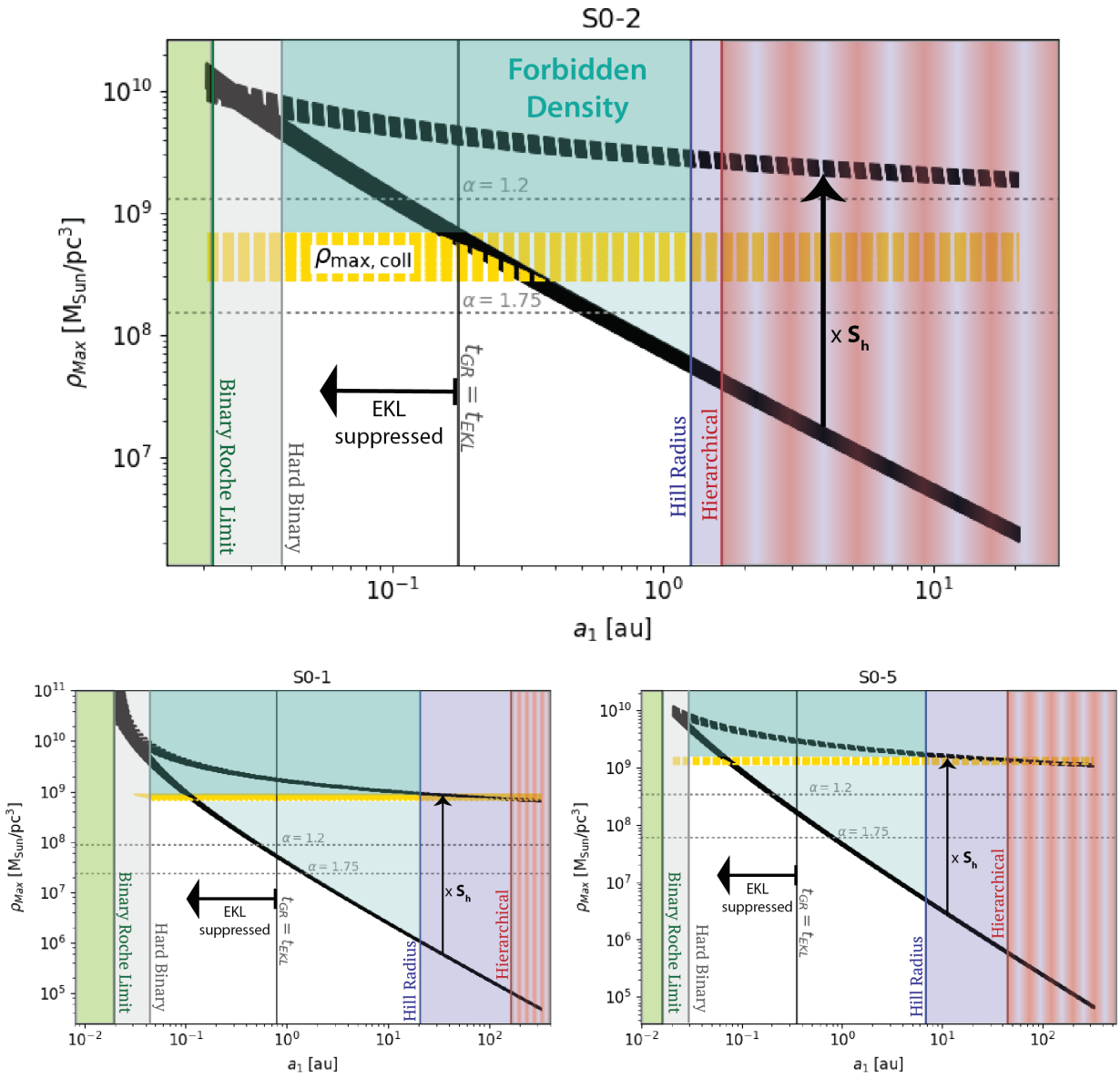

Figure 3.8: We take the orbital parameters of S0-1, S0-2, and S0-5 and, assuming that these stars in fact represent binaries, constrain the density-semimajor axis parameter space. As a function of binary semimajor axis, we find the maximum density (black solid line) allowed in the region given that the binary has yet to evaporate. We include the history parameter in the dashed black curve. The density at which the primary star has undergone an ionizing collision is given by the horizontal dashed gold line. Criteria for the Hill radius (blue) and dynamical stability (red) place upper limits on the maximum semimajor axis of the hypothetical binary, while the binary's Roche limit (green) sets the lower limit. We also calculated the region in which GR precession suppresses the EKL mechanism. We note that in the S0-1 plot, the $\rho_{\max,\mathrm{ev}}$ limit does not appear dashed because we plot these curves for a range of α.

Additionally, for a stable binary, no mass transfer or common envelop phase can be occurring. Therefore, the binary cannot cross its own internal Roche Limit. This condition places a lower limit on $a_{\rm bin}$:

$$a_{\rm bin} > R_j \left(\frac{m_j}{m_1 + m_2} \right)^{-1/3}, \tag{3.32}$$

where R_j denotes the radius of one of the stars. We choose the largest radius between the two stars to reach the most conservative limit, the green vertical line in Figure 3.8.

Radial velocity data for S0-2 (also known as S2) indicate that any hypothetical secondary is limited to about a solar mass (Chu et al., 2018). Furthermore, Habibi et al. (2017) provide values of 6.6 Myr old and $14\,M_\odot$ for the age and mass of S0-2. For our hypothetical S0-2 binary, we use a $14\,M_\odot$ primary and $1\,M_\odot$ secondary. S0-1 (also known as S1) and S0-5 (also known as S9) have approximate masses 12 and $8\,M_\odot$, respectively (e.g., Habibi et al., 2017). We use values 0.88, 0.56, and 0.64 for $e_\bullet$ and 16, 166, and 51.3 yr for $P_\bullet$ for S0-2, S0-1, and S0-5, respectively (Gillessen et al., 2017). We assume that the stars formed in the same star formation episode approximately 6 Myr ago. In our proof of concept, we adopt a secondary of $1\,M_\odot$ for each hypothetical binary. For less massive stars, the radial velocity effects of a binary may be less apparent, raising the possibility that the star has a more massive dark companion. However, the effects of companion mass on $\rho_{\rm max}$ is relatively weak such that even approaching an equal mass binary, the maximum density will change at most by a factor of 2.

A stable binary at this proximity to the SMBH will experience EKL perturbations, which tend to increase the binary eccentricity and may lead to merger (e.g., Naoz & Fabrycky, 2014; Naoz et al., 2016; Stephan et al., 2016, 2019). For example, the quadrupole timescale for S0-2 falls below $\sim 1 \times 10^5$ yr and may be as short as 10 yr for the range of semi-major axis shown in the figure. Thus, it is likely that the EKL mechanism has already driven an S-star binary to merge (e.g., Stephan et al., 2016, 2019). For a binary to remain stable and not undergo EKL oscillations, the general relativity precession timescale must be shorter

than the EKL-quadrapole timescale (e.g., Ford et al., 2000; Naoz et al., 2013b). Following Eq. (59) in Naoz (2016), this limit occurs at the black vertical line in Figure 3.8. To the left of this boundary, the EKL mechanism is suppressed.

We calculate the maximum density by using the binary's age as a lower limit on the evaporation (Eq. (3.26)) or collision time (Eq. (3.28)) . The solid black curve corresponds to the evaporation constraint. This curve represents the maximum density in the binary's neighborhood as a function of the binary's semi major axis a_1. The dashed black curve is the $\rho_{\rm max,ev}$ scaled by the history parameter to give a very conservative upper limit. The true density of the region must lie below this curve for the hypothetical binary to remain bound today. Additionally, the gold curve depicts the density at which the binary is unbound by a physical collision. These hypothetical systems meet the criterion $\sigma(a_\bullet) > v_{\rm crit}$ for all values of α. The range of α values introduces a spread in the $\rho_{\rm max}$ estimate, with the uppermost limit of $\rho_{\rm max,coll}$ corresponding to $\alpha = 1$. For comparison, the horizontal dashed grey curves represent the density in the binary's neighborhood as given by the power law Eq. (5.1) for two values of α.

We note that for younger systems such as these, we expect the true $\rho_{\rm max}$ to lie closer to the solid black curve, $\rho_{\rm max}$ without the history parameter, because the system has had less time to evolve from its initial configuration. We denote this uncertainty by shading this density region in a lighter teal in Figure 3.8. However, generally, the most conservative maximum density estimate is given by either the collision timescale or the evaporation timescale with the history parameter. For these massive binaries, the collision timescale sets the upper limit on the regional density. The plot can be interpreted in two ways, depending on the observational constraint. For example, if observations indicate a density of $\sim 8\times10^8\,M_\odot/{\rm pc}^3$, the semimajor axis of an S0-5 binary cannot exceed about 0.1 au if we assume no evolution from a tighter initial configuration. However, if observations determine that S0-1 is a binary with semimajor axis 0.1 au, the density must fall below $\sim 10^9\,M_\odot/{\rm pc}^3$.

3.6 Discussion

Recent observational and theoretical studies suggest the presence of binaries in the GC (e.g., Ott et al., 1999; Rafelski et al., 2007; Dong et al., 2017a,b; Stephan et al., 2016, 2019; Naoz et al., 2018; Gautam et al., 2019). These binaries may have a soft orbital configuration, such that their binding energy is less than the kinetic energy of the neighboring stars. In this dense environment, interactions with neighboring stars can alter the binary's orbital parameters (e.g., Rasio & Heggie, 1995; Heggie & Rasio, 1996). Over time, these interactions can unbind soft binaries (e.g., see derivation of Eq. (7.173) in Binney & Tremaine, 2008). The timescale for unbinding, or evaporation, depends on the density of the surrounding region. Similarly, a star in a binary may undergo a direct collision with a passing star, which may unbind the binary, and the collision rate depends on the neighborhood density. Therefore, a detection of a soft binary can constrain the underlying density profile in the GC.

We consider the following processes that can affect the binary: (1) unbinding due to interactions with neighboring stars, with the associate evaporation timescale for an arbitrary eccentric orbit (Eq. (3.16)); (2) collision with passing stars (Eq. (3.18)) that may unbind the binary if the velocity dispersion exceeds the critical velocity; (3) the two body relaxation process by which the binary migrates toward the center over a typical timescale (Eq. (5.7)); and finally, the EKL mechanism that can drive a binary to merge (e.g., Stephan et al., 2016, 2019). Figure 5.1 depicts the relevant timescales. We find that some soft binaries at approximately 0.1 pc from the SMBH migrate inwards before they unbind. These binaries relocate to a region of higher density, where had they resided over their full lifetime, they would have already evaporated. Additionally, the eccentricity about the SMBH has a marginal effect on the evaporation and collision timescales, used to constrain the GC density.

We derive a density constraint to ensure the binary's survival over its lifetime. Given a binary's age, we estimate the maximum density of the surrounding region, above which the binary would have already evaporated or undergone a direct collision, unbinding the system.

We outline this procedure using several proofs of concept. Firstly, we consider the potential of a confirmed wide binary to constrain the GC density. We focus on IRS 16NE, a young wide binary[8], as a case study. While this binary is hard at its estimated position of 0.15 pc, we show that an IRS 16NE-like binary can be used to constrain the density closer to the SMBH. We also consider an older low-mass system. Figure 3.5 compares the maximum density allowed by a binary to power law density distributions in the GC.

Additionally, as a binary can constrain environmental properties, environmental properties can inform the maximum orbital separation of a hypothetical binary. Given a power law density distribution for the GC, Figure 3.6 and 3.7 depict the allowable binary separation as a function of distance from the SMBH for a hypothetical system to survive over its lifetime. These figures correspond to a young and old binary, respectively. Figures 3.5 and 3.7 imply that a low-mass, older ($1\,\mathrm{Gyr} \leq t_{\mathrm{age}}$) binary cannot exist within 0.01 pc of the SMBH. The detection of such a system may indicate a dynamical formation mechanism. Lastly, we combine the approaches of Figures 3.5 and 3.6 in Figure 3.8. The S-star cluster consists of several well-studied stars with constrained orbits about the SMBH (e.g., Ghez et al., 2005; Habibi et al., 2019; Gillessen et al., 2017). We consider the possibility that one of these stars is embedded in a soft binary system and constrain the binary separation and density parameter space.

We demonstrate that the density constraining procedure must consider collisions for any system, especially those with a massive star whose larger cross-section increases the collision rate. The collision timescale, not the evaporation timescale, sets the upper limit on the local density, provided that the collision has sufficient energy to ionize the system. Future work may extend this procedure to environments in which a SMBH does not dominate the gravitational potential. In such environments, the velocity dispersion will depend on the

[8] Alexander & Pfuhl (2014) estimate IRS 16NE's age to be consistent with the overall young population at the GC, a few Myr (e.g., Paumard et al., 2006). Furthermore, IRS 16NE has an orbit of $P = 224$ days (Pfuhl et al., 2014).

density profile. We reserve a more comprehensive integration of collisions and their outcomes into this framework for future study. Future work may also incorporate other processes like tidal capture and clarify their bearing on our ability to derive density constraints from binary systems.

Acknowledgements

We dedicate this paper to the late Tal Alexander, who served as an inspiration for the study of dynamics in dense stellar clusters. In particular, SN would like to thank Tal for sponsoring her as a visiting student at the Weizmann Institute. This opportunity helped her, as a young mother, to juggle new responsibilities and pursuing a PhD by reducing her commute. Furthermore, the experience expanded her collaborations and led to new directions. Thank you, Tal!

We thank the referee for useful comments and questions. We thank Brad Hansen for asking an important question about collisions, which prompted the collision section. SR thanks the Alice Freeman Palmer Fellowship, awarded by Wellesley College, for partial support. SR and SN acknowledge the partial support of NASA grants No. 80NSSC20K0505 and 80NSSC19K0321. SN thanks Howard and Astrid Preston for their generous support.

3.7 Appendix

3.7.1 Velocity Dispersion Evolution

Our framework does not account for a velocity dispersion that evolves over time. We assume a steady-state. We compute the fractional change in the nuclear star cluster's energy from evaporating binaries, the process that we focus on in this study. However, we stress that this exercise does not provide an accurate picture of the velocity dispersion's time evolution.

Ciurlo et al. (2020) estimate a binary fraction of about 5 per cent for low-mass stars. Assuming that there are approximately one million stars in the GC, we generate 72000 dynamically stable stellar binary systems. We use the same birth distributions as Stephan et al. (2016) except our Kroupa IMF has the lower (upper) limit $0.5\,M_\odot$ ($100\,M_\odot$) for the primary and secondary masses. We use S0-2's period to set the lower limit on the birth period distribution for the outer orbit (Stephan et al., 2016). Therefore, these binary systems have $a_\bullet \gtrsim 0.003$ or $10^{-2.5}$ pc. For $\alpha = 1.2$, 99 per cent of the systems are soft. We calculate the evaporation timescale and binding energy for each soft binary. Massive binaries, systems with a $10\,M_\odot$ or larger primary star, represent ~ 5 per cent of the soft systems. All of the soft binaries also meet the criterion to unbind through a collision given by Eq. (3.27) at their respective distance from the SMBH, however only about 2000 systems will undergo a direct collision before they evaporate. Additionally, the EKL mechanism should drive some fraction of these systems to merge before they evaporate (e.g., Stephan et al., 2016). In this calculation, we assume that all soft systems evaporate.

Integrating the following over 10^{-4} to 0.5 pc provides an estimate of the initial kinetic energy for the nuclear star cluster:

$$E_0 = \frac{1}{2}\int_{r_{\rm inner}}^{r_{\rm outer}} \rho\sigma^2 \times 4\pi r^2 dr, \tag{3.33}$$

where ρ and σ are both functions of r given in Section 3.2. We assume that kinetic energy from the cluster goes into unbinding binaries through interactions with neighbor stars. The kinetic energy of the cluster should therefore decrease with time. We assume that all of the binary's potential energy is released at the evaporation time as opposed to in a gradual process. We use these quantities to arrive at a fractional change in cluster kinetic energy as a function of time (Figure 3.9). The small fractional change in energy suggests that a similarly small change in the velocity dispersion, allowing us to assume σ is constant over long periods of time such as a low-mass binary's lifetime.

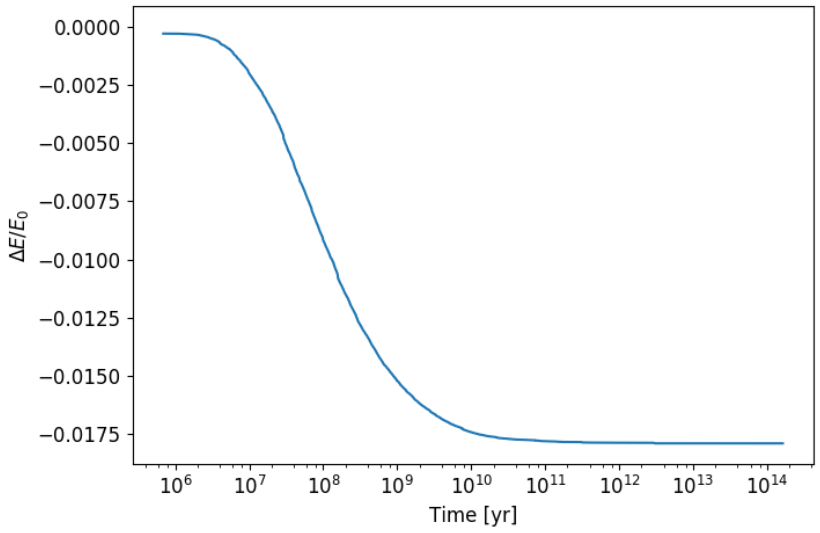

Figure 3.9: We compute the fractional change in the star cluster's kinetic energy due to evaporating binaries. We compare the binding energy of the evaporated binaries to the total kinetic energy of the star cluster from Eq. (3.33).

3.7.2 Coulomb Logarithm

We must assume the Coulomb Logarithm is constant in Section 3.2.1.2 to derive the evaporation timescale as a function of eccentricity. This assumption requires that the Coulomb Logarithm varies slowly between the apoapsis and periapsis of an orbit. Figure 3.10 shows the Coulomb logarithm for low-mass and massive binaries as a function of distance from the SMBH. Additionally, in Section 3.4.2, we assume a constant Coulomb logarithm. We adopt a value of 5 based on Figure 3.10.

3.7.3 Mass segregation and comparison with globular clusters

Unlike globular clusters in which two body relaxation can cause a gradual evaporation of the cluster (e.g., Gieles et al., 2011; Gnedin et al., 2014), nuclear star clusters reside in deeper potential wells. Here we consider a population of 70000 stable systems (see Appendix 3.7.1). Figure 3.11 compares the semimajor axis distributions for the total population of soft binaries (blue) and those with $t_{\rm seg} < t_{\rm ev}$ (orange). The left panel shows $a_{\rm bin}$, and the right, $a_\bullet$. The

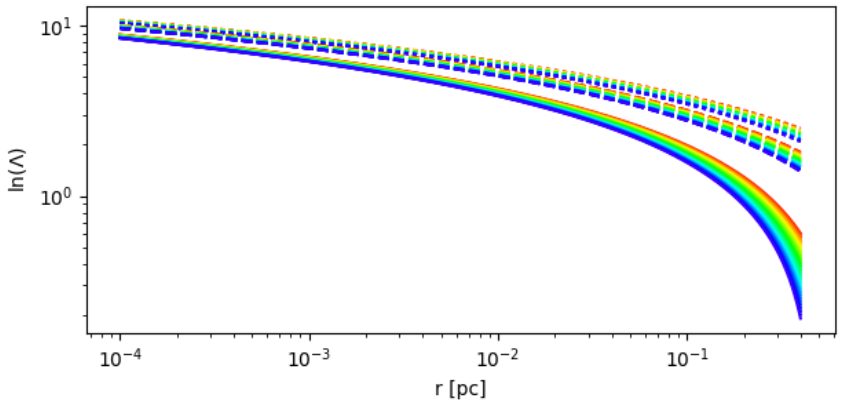

Figure 3.10: The Coulomb logarithm does not vary substantially within 1 pc of the Galactic Center. Here we plot the Coulomb logarithm for different values of α, ranging from 1 (red) to 2 (blue). The dotted curve represents an equal mass $2\,M_\odot$ binary with separation 0.5 au. The dashed (solid) curve represent an equal mass $80\,M_\odot$ binary with separation 10 (3) au.

figure indicates that systems that segregate by mass before unbinding tend to be marginally soft, tighter systems further out from the SMBH, where the velocity dispersion is lower.

Binary demographics in globular clusters may provide interesting parallels to the GC. For example, Geller et al. (2013) and de Grijs et al. (2013) suggest that, contrary to the effects of mass segregation, the binary fraction in the globular cluster NGC 1818 decreases radially towards the center because binary disruption dominates closer to the core. Cheng et al. (2020) discuss a similar competition between mass segregation and binary disruption in the context of the globular cluster M28's X-ray binary population. While N-body simulations are necessary to obtain a comprehensive picture of GC binary demographics over time, based on these calculations, we expect that mass segregation plays a secondary role to evaporation in shaping the distribution of binaries in the GC, in particular the binary fraction as a function of distance from the SMBH. The vast majority of systems are soft and unbind over shorter timescales. We expect a dearth of binaries with decreasing distance to the SMBH, a trend that will become more pronounced over time. Those soft binaries which migrate inwards will also eventually evaporate.

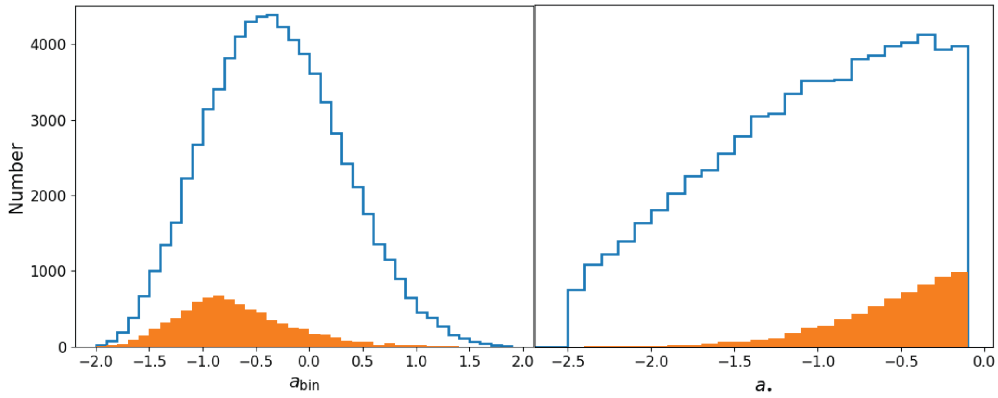

Figure 3.11: The blue histogram shows the semimajor axes of the inner and outer orbits for approximately $70,000$ soft stellar binaries in the GC using the parameter distributions of Stephan et al. (2016). The orange filled histogram depicts the semimajor axes for those systems with $t_{\rm seg} < t_{\rm ev}$. The differences between the blue and orange histograms indicate that migrating systems are generally marginally soft, tighter binaries residing further from the SMBH.

CHAPTER 4

The Formation of Intermediate Mass Black Holes in Galactic Nuclei

Most stellar evolution models predict that black holes (BHs) should not exist above approximately $50 - 70$ $M_\odot$, the lower limit of the pair-instability mass gap. However, recent LIGO/Virgo detections indicate the existence of BHs with masses at and above this threshold. We suggest that massive BHs, including intermediate mass black holes (IMBHs), can form in galactic nuclei through collisions between stellar-mass black holes and the surrounding main-sequence stars. Considering dynamical processes such as collisions, mass segregation, and relaxation, we find that this channel can be quite efficient, forming IMBHs as massive as 10^4 $M_\odot$. This upper limit assumes that (1) the BHs accrete a substantial fraction of the stellar mass captured during each collision and (2) that the rate at which new stars are introduced into the region near the SMBH is high enough to offset depletion by stellar disruptions and star-star collisions. We discuss deviations from these key assumptions in the text. Our results suggest that BHs in the pair-instability mass gap and IMBHs may be ubiquitous in galactic centers. This formation channel has implications for observations. Collisions between stars and BHs can produce electromagnetic signatures, for example, from x-ray binaries and tidal disruption events. Additionally, formed through this channel, both black holes in the mass gap and IMBHs can merge with the supermassive black hole at the center of a galactic nucleus through gravitational waves. These gravitational wave events are extreme and intermediate mass ratio inspirals (EMRIs and IMRIs, respectively).

4.1 Introduction

The recently detected gravitational wave source GW190521 (The LIGO Scientific Collaboration et al., 2020a,b) produced an intermediate mass black hole of approximately 142 $M_\odot$. This event may have also had a 85 $M_\odot$ progenitor, which falls within the pair-instability mass gap that limits stellar black holes (BHs) to no more than $\lesssim 50$ $M_\odot$ (e.g., Heger et al., 2003; Woosley, 2017)[1]. Similarly, the merger products of GW150914, GW170104, and GW170814 fall within the mass gap (e.g., Abbott et al., 2016, 2017a,b). BH mergers that form second generation BHs and, in some cases, intermediate mass BHs (IMBHs), these gravitational wave (GW) events can occur in globular clusters, young stellar clusters, or the field (e.g., Rodriguez et al., 2018; Rodriguez et al., 2019; Fishbach et al., 2020; Mapelli et al., 2021b,a; Di Carlo et al., 2019, 2021; Dall'Amico et al., 2021; Arca Sedda et al., 2023). However, IMBHs are not limited to these locations and may reside in galactic nuclei as well. Several studies propose that our own galactic center may host an IMBH in the inner pc (e.g., Hansen & Milosavljević, 2003; Maillard et al., 2004; Gürkan & Rasio, 2005; Gualandris & Merritt, 2009; Chen & Liu, 2013; Generozov & Madigan, 2020; Fragione et al., 2020a; Zheng et al., 2020; Naoz et al., 2020; GRAVITY Collaboration et al., 2020).

Several IMBH formation channels have been suggested in the literature. For example, IMBHs may have a cosmological origin, forming in the early universe either as a result of the very first stars (e.g., Madau & Rees, 2001; Schneider et al., 2002; Johnson & Bromm, 2007; Valiante et al., 2016) or from direct collapse of accumulated gas (e.g., Begelman et al., 2006; Yue et al., 2014; Ferrara et al., 2014; Choi et al., 2015; Shlosman et al., 2016). These high redshift IMBHs would need to survive galaxy evolution and mergers to present day (e.g., Rashkov & Madau, 2014), with significant effects on their stellar and even dark matter surroundings (e.g., Bertone et al., 2009; Chen & Liu, 2013; Bringmann et al., 2012; Eda

[1]Note that the exact lower and upper limits may be sensitive to metallicity of the progenitor (e.g., Woosley, 2017; Spera & Mapelli, 2017; Limongi & Chieffi, 2018; Sakstein et al., 2020; Belczynski et al., 2020; Renzo et al., 2020; Vink et al., 2021).

et al., 2013; Naoz & Silk, 2014; Naoz et al., 2019). Another popular formation channel relies on the coalescence of many stellar-mass black holes, which may seed objects as massive as SMBHs (e.g., Kroupa et al., 2020). IMBHs may form in the centers of globular clusters, where few-body interactions lead to the merger of stellar-mass BHs (e.g., O'Leary et al., 2006; Gürkan et al., 2006; Blecha et al., 2006; Freitag et al., 2006; Umbreit et al., 2012; Rodriguez et al., 2018; Rodriguez et al., 2019; Fragione et al., 2020b). Other formation mechanisms invoke successive collisions and mergers of massive stars (e.g., Ebisuzaki et al., 2001; Portegies Zwart & McMillan, 2002; Portegies Zwart et al., 2004; Freitag et al., 2006; Sakurai et al., 2017; Kremer et al., 2020; González et al., 2021; Di Carlo et al., 2021; Das et al., 2021b,a; Escala, 2021).

The main obstacle to sequential BH mergers in clusters is that the merger recoil velocity kick often exceeds the escape velocity from the cluster (e.g., Schnittman & Buonanno, 2007; Centrella et al., 2010; O'Leary et al., 2006; Baibhav et al., 2020, Rom & Sari, in prep.). However, nuclear star clusters at the centers of galaxies do not encounter this problem. For example, Fragione et al. (2021) explore repeated BH-BH mergers in nuclear star clusters without a SMBH. They considered BH binary-single interactions, binary BH GW merger, and GW merger recoil kicks. The post-kick merger product sinks back towards the cluster center over a dynamical friction timescale. Using this approach, they showed that $10^3 - 10^4$ $M_\odot$ IMBHs can form efficiently over the lifetime of a cluster.

However, as discussed in Section 4.2.2, direct BH-star collisions are much more frequent than BH-BH collision in galactic nuclei, making the former a promising channel for BH growth. In an N-body study of young star clusters, Rizzuto et al. (2022) find that BH-star collisions are a main contributor to the formation of BHs in the mass gap and IMBHs. In a similar vein, Stone et al. (2017) demonstrate that massive BHs can form from repeated tidal encounters between stars and BHs. More generally, several studies have explored the role of collisions in a GN, with implications for the stellar and red giant populations (e.g., Dale & Davies,

2006; Dale et al., 2009; Balberg et al., 2013; Mastrobuono-Battisti et al., 2021). We propose that IMBHs can form naturally within the central pc of a galactic center through repeated collisions between BHs and *main sequence stars*. During a collision, the BH can accrete some portion of the star's mass. Over many collisions, it can grow appreciably in size. We demonstrate that this channel can create IMBHs with masses as large as 10^4 $M_\odot$, an upper limit that depends on the density profile of the surrounding stars and the efficiency of the accretion.

The paper is structured as follows: we describe relevant physical processes and our approach in Section 4.2. In particular, we provide an overview of collisions in Section 4.2.2 and present our statistical approach in Section 4.2.3. Section 4.2.4 discusses our treatment of the mass growth with each collision and presents analytic solutions to our equations in two different regimes, efficient collisions and inefficient collisions We compare these solutions to our statistical results. Sections 4.2.6 and 4.2.8 discuss implications for GW merger events between IMBHs and the SMBH. We then incorporate relaxation processes and discuss the subsequent results in Section 4.2.9. Finally, we discuss and summarize our findings in Section 4.3.

4.2 Methodology

We consider a population of stellar mass BHs embedded in a cluster of 1 $M_\odot$ stars. When stars and BHs collide, the BHs can accrete mass. The growth rate depends on the physical processes outlined below. We use a statistical approach to estimate the stellar encounters and final IMBH masses.

4.2.1 Physical Picture

We consider a population of BHs within the inner few parsecs of the SMBH in a galactic nucleus (GN). We assume that the BH mass distribution follows that of the stars from which they originate, a Kroupa initial mass function $dN/dm \propto m^{-2.35}$. While this choice repre-

sents a gross oversimplification, it has very little bearing on our final results. Future work may address the particulars of the BH mass distribution, but we do not expect that it will significantly alter the outcome. The upper and lower limits of the BH mass distribution are 5 and 50 $M_\odot$, respectively. We select the upper limit to encompass the range of upper bounds predicted by stellar evolution models, which vary between 40 and 125 $M_\odot$ depending on the metallicity (Heger et al., 2003; Woosley, 2017; Spera & Mapelli, 2017; Limongi & Chieffi, 2018; Belczynski et al., 2020; Renzo et al., 2020). We assume that the orbits of the BHs follow a thermal eccentricity distribution. We draw their semimajor axes, $a_\bullet$, from a uniform distribution in log distance, $dN/d(\log r)$ being constant. While this distribution is not necessarily representative of actual conditions in the GN, we use it to build a comprehensive physical picture of BH growth at all distances from the SMBH, including within 0.01 pc. Otherwise, the innermost region of the GN would be poorly represented in our sample. We consider other observationally motivated distributions in Section 4.2.9, but reserve a more detailed examination of the distribution's impact for future work.

4.2.2 Direct Collisions

BHs in the GN can undergo direct collisions with other objects. The timescale for this process, $t_{\rm coll}$, can be estimated using a simple rate calculation: $t_{\rm coll}^{-1} = n\sigma A$, where n is the number density of objects, σ is the velocity dispersion, and A is the cross-section. We use the collision timescale from Rose et al. (2020):

$$\begin{aligned} t_{\rm coll}^{-1} &= \pi n(a_\bullet)\sigma(a_\bullet) \\ &\times \left(f_1(e_\bullet) r_c^2 + f_2(e_\bullet) r_c \frac{2G(m_{BH}+m_\star)}{\sigma(a_\bullet)^2} \right) . \end{aligned} \tag{4.1}$$

where G is the gravitational constant and r_c is the sum of the radii of the interacting objects, a black hole with mass m_{BH} and a star with mass $m_\star$. Detailed in Rose et al. (2020), $f_1(e_\bullet)$ and $f_2(e_\bullet)$ account for the effect of the eccentricity of the BH's orbit about the SMBH on the collision rate, while n and σ are simply evaluated at the semimajor axis of the orbit (see below). Note that this timescale equation includes the effects of gravitational focusing,

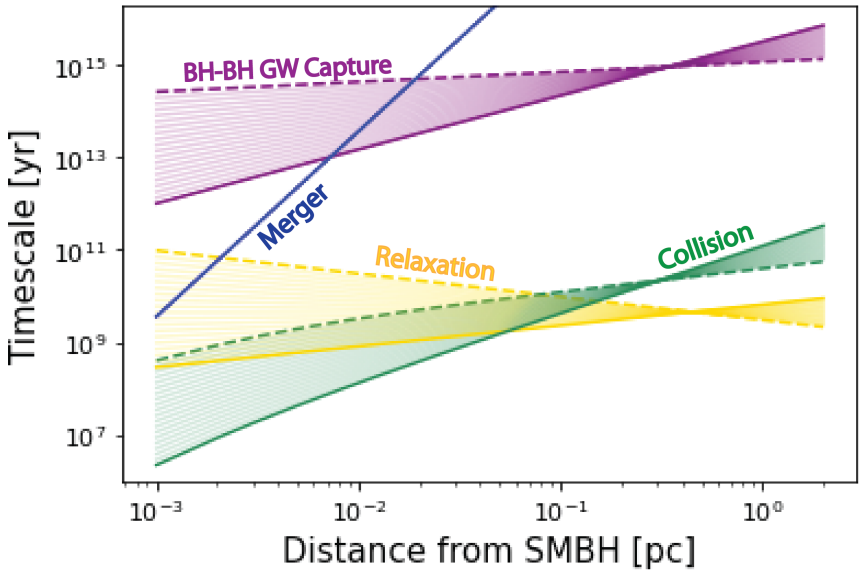

Figure 4.1: We plot the relevant timescales, including collision (green), relaxation (gold), and BH-BH GW capture (purple), for a single BH in the GN as a function of distance from the SMBH. For the collision timescale, we assume the BH is on a circular orbit. The timescales depend on the density, so we adopt a range of density profiles, bounded by $\alpha = 1$ (dashed curve) to $\alpha = 2$ (dark, solid curve). The dark blue line represents the time for a 10^5 $M_\odot$ BH to merge with the SMBH through GW emission.

which enhances the cross-section of interaction.

Assuming a circular orbit for simplicity, we plot the timescale for a BH orbiting in the GN to collide with a $1\,M_\odot$ star as a function of distance from the SMBH in Figure 5.1.[2] As this timescale depends on the density of surrounding stars, we adopt a density profile of the form:

$$\rho(r_\bullet) = \rho_0 \left(\frac{r_\bullet}{r_0}\right)^{-\alpha} , \tag{4.2}$$

where $r_\bullet$ denotes the distance from the SMBH. We adopt a SMBH mass of 4×10^6 $M_\odot$ such that our fiducial GN matches our own galactic center (e.g., Ghez et al., 2005; Genzel et al., 2003). In this case, the normalization in Eq. (5.1) is $\rho_0 = 1.35 \times 10^6\, M_\odot/\mathrm{pc}^3$ at $r_0 = 0.25\,\mathrm{pc}$ (Genzel et al., 2010). Additionally, in Eq. (5.1), α gives the slope of the power law. We assume that a uniform population of solar mass stars account for most of the mass in the

[2]We note that the eccentricity has a very minor effect on the collision timescale (Rose et al., 2020).

GN, making the stellar number density:

$$n(r_\bullet) = \frac{\rho(r_\bullet)}{1\,M_\odot}\ . \tag{4.3}$$

The collision timescale also depends on the velocity dispersion, which we express as:

$$\sigma(r_\bullet) = \sqrt{\frac{GM_\bullet}{r_\bullet(1+\alpha)}}, \tag{4.4}$$

where α is the slope of the density profile and $M_\bullet$ denotes the mass of the SMBH (Alexander, 1999; Alexander & Pfuhl, 2014). As mentioned above, Eq. (5.4) depends on the sum of the radii of the colliding objects, r_c. We take $r_c = 1\,R_\odot$ because these interactions involve a BH and a star, and the former has a much smaller physical cross-section. For example, the Schwarzschild radius of a $10\,M_\odot$ BH is only 30 km, or $4.31 \times 10^{-5}\,R_\odot$. For this reason, direct collisions between compact objects are very rare and not included in our model.

We note that direct collisions between BHs, via GW emission, were shown to be efficient in nuclear star clusters without SMBHs (e.g., Portegies Zwart & McMillan, 2000; O'Leary et al., 2006; Rodriguez et al., 2016). However, in the GN, star-BH collisions are much more frequent than direct BH-BH collisions. As depicted in Figure 5.1, the star-BH collision timescale for a range of density profiles is many orders of magnitude shorter than the BH-BH GW collision timescale (for the relevant equations, see O'Leary et al., 2009; Gondán et al., 2018, for example). Thus, we expect that star-BH collisions will be the main driver of IMBH growth in the GN.

4.2.3 Statistical Approach to Collisions

We simulate the mass growth of a population of BHs with initial conditions detailed in Section 4.2.1. Over an increment Δt of 10^6 yr, we calculate the probability of a collision occurring, given by $\Delta t/t_{\rm coll}$. This choice of Δt is motivated by our galactic center's star formation timescale (e.g., Lu et al., 2009), allowing for regular replenishment of the stellar population in the GN. We have checked that the results are not sensitive to this choice of Δt,

omitted here to avoid clutter. We draw a number between 0 and 1 using a random number generator. If that number is less than or equal to the probability, we increase the BH's mass by Δm, the mass that the BH is expected to accrete in a single collision (see Section 4.2.4 for details). We recalculate the collision timescale using the updated BH mass and repeat this process until the time elapsed equals the simulation time of 10 Gyr[3].

4.2.4 Mass Growth

When a BH collides with a star, it may accrete material and grow in mass. The details of the accretion depend on the relative velocity between the BH and star. For simplicity, this calculation assumes that the two objects experience a head on collision, with the BH passing through the star's center. We begin by considering the escape velocity from the BH at the star's outermost point, its surface, which corresponds to the maximum impact parameter 1 $R_\odot$. Qualitatively, one might expect that the BH could capture the entire star (i.e., $\Delta m \sim 1$ $M_\odot$) if the relative velocity is smaller than the escape velocity from the BH at this point. However, in the vicinity of the SMBH, the dispersion velocity of the stars may be much larger than the escape velocity from the BH at the star's surface. In this case, the BH captures a "tunnel" of material through the star. This tunnel has radius equal to the Bondi radius and length approximately $1\,R_\odot$. For the purposes of this study, we assume that the BH accretes all of the material that it captures. The details of the accretion are uncertain, however, and it may be much less efficient than our results imply. We discuss accretion in Section 4.2.5.

To estimate Δm, we begin with the Bondi-Hoyle accretion rate, $\dot{m}$, given by:

$$\dot{m} = \frac{4\pi G^2 m_{\rm BH}^2 \rho_{\rm star}}{\left(c_s^2 + \sigma^2\right)^{3/2}} \ , \tag{4.5}$$

where c_s is the speed of sound in the star and $\rho_{\rm star}$ is its density (e.g., Bondi, 1952; Bondi

[3]Closer to the SMBH, Δt may exceed the collision timescale by a factor of a few for steep density profiles. We include a safeguard in our code which takes the ratio $t_{\rm coll}/\Delta t$ and rounds it to the nearest integer. We take this integer to be the number of collisions and increase the BH mass accordingly.

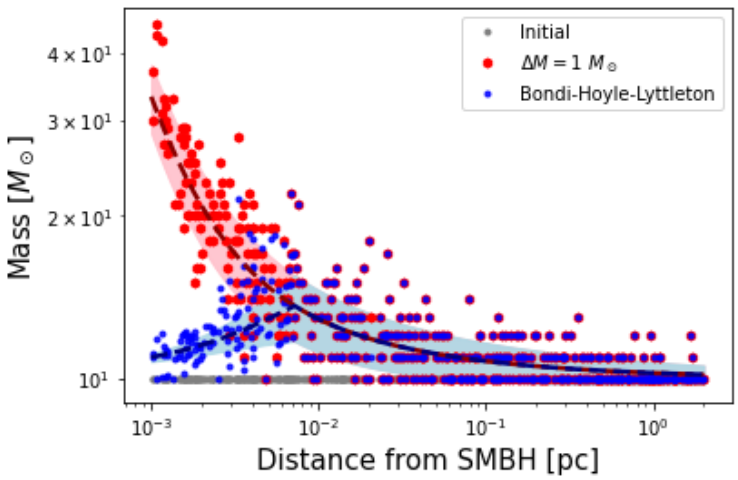

Figure 4.2: We consider an example that highlights the mass growth as a function of distance from the SMBH. Grey dots represent the initial masses and distances from the SMBH of the BHs involved in the simulation. For simplicity, we set the inital mass equal to $10\,M_\odot$ for all of the BHs. Assuming the density profile of stars has $\alpha = 1$, we consider two cases: BHs accrete all of the star's mass during a collision (red) and only a portion of the star's mass is accreted during a collision given by Eq. 4.6 (blue). The latter case results in less growth closer to the SMBH where the velocity dispersion becomes high. The shaded regions and dashed lines represent the analytical predictions detailed in Section 4.2.4.

& Hoyle, 1944; Shima et al., 1985; Edgar, 2004, see latter for a review). We approximate the density as $1\,M_\odot/(4\pi R_\odot^3/3)$ and take the conservative value of $c_s = 500\ km\ s^{-1}$, which is consistent with the sound speed inside a 1 $M_\odot$ star (Christensen-Dalsgaard et al., 1996) and allows us to set a lower limit on Δm. To find Δm, at each collision, we have:

$$\Delta m = \min(\dot{m} \times t_{\star,\rm cross}, 1\ \mathrm{M}_\odot)\ , \tag{4.6}$$

where $t_{\star,\rm cross} \sim R_\odot/\sigma$ is the crossing time of the BH in the star. We take the minimum between $\dot{m} \times t_{\star,\rm cross}$ and 1 $\mathrm{M}_\odot$ because the BH cannot accrete more mass than one star at each collision.

Figure 4.2 juxtaposes the expected growth using Bondi-Hoyle-Lyttleton accretion (blue small points) with a much simpler model in which the BH accretes the star's entire mass, $1\,M_\odot$ (red large points). Both examples start with identical populations of $10\,M_\odot$ BHs (grey) and simulate growth through collisions using a statistical approach. As the BHs grow, the collision timescale, which depends on m_{BH}, decreases. Simultaneously, Δm, which also

depends on m_{BH}, increases. The result is exponential growth (see discussion and details surrounding Eq. (4.8)). In Figure 4.2, however, the simulations assume $\alpha = 1$ for the stellar density profile, ensuring the collision timescale is long compared to the simulation time, 10 Gyr. Therefore, the BHs grow slowly, and their final masses can be approximated using the following equation:

$$m_{\rm final}(t_{\rm coll} \to \text{const.}) \quad = \quad m_{\rm initial} + \Delta m \frac{T}{t_{\rm coll}} \ , \tag{4.7}$$

in which T represents the simulation time and Δm and $t_{\rm coll}$ remain constant, approximated as their initial values.

This equation is plotted in Figure 4.2 for both cases, $\Delta m = 1\,M_\odot$ (red) and Δm from Bondi-Hoyle-Lyttleton accretion (blue), and the curves coincide with the corresponding simulated results. The shaded regions represent one standard deviation from Eq. (4.7), calculated using the square root of the number of collisions, $T/t_{\rm coll}$. As indicated by the results in red, in the absence of Bondi-Hoyle-Lyttleton accretion, the BHs closest to the SMBH experience the most growth because they have shorter collision timescales. However, Bondi-Hoyle-Lyttleton accretion becomes important closer to the SMBH, where the velocity dispersion is large compared with the stars' escape velocity, and curtails the mass growth for BHs in this region. Outside of 10^{-2} pc, a BH consumes the star's entire mass: the accretion-limited Δm governed by Eq. (4.7) is greater than or equal to the star's mass.

Eq. 4.7 does not apply for other values of α. When the collision timescale is shorter, corresponding to a larger index α in the density profile (see Figure 5.1), the growth is very efficient and Δm quickly approaches $1\,\mathrm{M}_\odot$. Consequently, while we can now assume $\Delta m = 1\,\mathrm{M}_\odot$, we can no longer assume the collision timescale is constant. The final mass grows exponentially as a result. For $\Delta m = 1\mathrm{M}_\odot$, the general solution is reached by solving the differential equation $dm/dt = 1\,M_\odot/t_{\rm coll}(m)$, which gives:

$$m_{\rm final}(\Delta m \to 1\,\mathrm{M}_\odot) \quad = \quad -A + (m_{\rm initial} + A)\, e^{CT} \tag{4.8}$$

where $A = \sigma^2 R_{\rm star}/G$ and $C = 2\pi G n_{\rm star} R_{\rm star}/\sigma$. As an example, we plot this curve in purple for the $\alpha = 2$ case, in Figure 4.3, which agrees with the simulated masses.

4.2.5 Uncertainties in Accretion

We note that the ΔM calculated in this proof-of-concept study assumes that the BH accretes all of the material that it captures. Estimating the true fraction of the material accreted by the BH is very challenging; this complex problem requires numerically solving the generalized GR fluid equations with cooling, heating, and radiative transfer, etc. and remains an active field of research (e.g., Blandford & Begelman, 1999; Park & Ostriker, 2001; Narayan et al., 2003; Igumenshchev et al., 2003; Ohsuga et al., 2005; Yuan et al., 2012; Jiang et al., 2014; McKinney et al., 2014; Narayan et al., 2022). Heuristically, if a collision between a BH and a star results in an accretion disk, the disk's viscous timescale may be as low as days. The resultant luminosity can unbind most of the captured material, though details such as the amount accreted and peak luminosity remain uncertain (e.g., Yuan et al. (2012); Jiang et al. (2014), see also the discussion in Stone et al. (2017), Rizzuto et al. (2022), and Kremer et al. (2022)). The question becomes whether or not a BH can still accumulate significant amounts of mass over many collisions even if it accretes very little in a single one. We explore the viability of our channel using a physically motivated inefficient accretion model. Several studies have invoked momentum-driven winds in BH accretion (e.g., Murray et al., 2005; Ostriker et al., 2010; Brennan et al., 2018). We thus estimate the fraction of captured mass accreted to be approximately $v_{esc}/(c\eta)$, where v_{esc} is the escape velocity from the BH at 1 $R_\odot$ and η is the accretion efficiency at the ISCO. We take η to be 0.1 (e.g., Yu & Tremaine, 2002). This expression for the fraction accreted is consistent with Kremer et al. (2022) equation 19 for $s = 0.5$, which is a reasonable value for s, a free parameter between 0.2 and 0.8. We discuss the results of the momentum-driven winds estimate in Section 4.3. We note that the accretion process may be more efficient than this estimate implies if, for example, jets or other instabilities result in the beaming of radiation away from the captured material (e.g.,

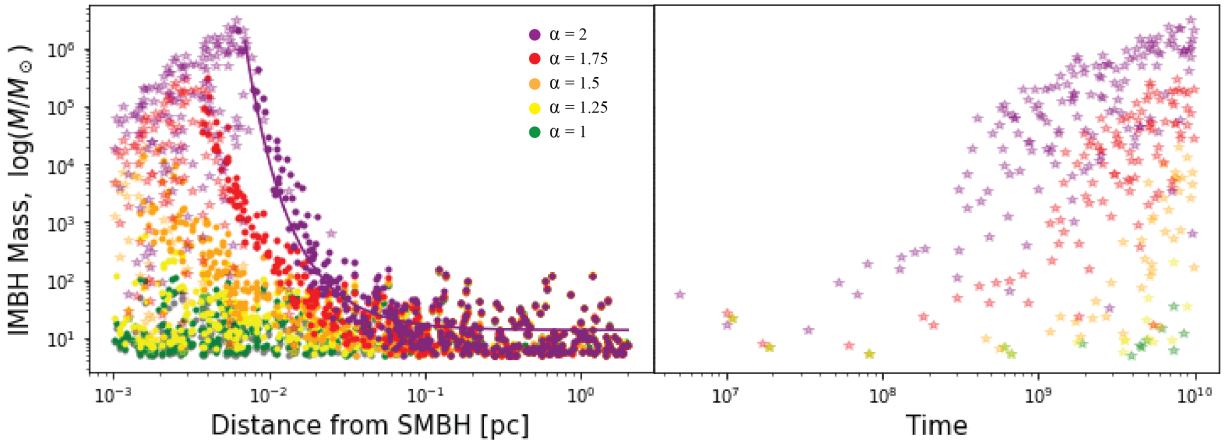

Figure 4.3: On the right, we plot final masses of 500 BHs using different values of α in the density profile, shallow ($\alpha = 1$) to cuspy ($\alpha = 2$). For the latter case, the purple line shows the analytical result from Eq. 4.8, taking $m_{\rm initial}$ to be the average mass of the population. Faded stars indicate BHs that merged with the SMBH through GWs. On the left, we plot the masses and merger times of these BHs.

Blandford & Znajek, 1977; Begelman, 1979; De Villiers et al., 2005; McKinney & Gammie, 2004; McKinney, 2006; Igumenshchev, 2008; Begelman, 2012b,a; McKinney et al., 2014).

4.2.6 GW Inspiral

When a BH is close to the SMBH, GW emission can circularize and shrink its orbit. We implement the effects of GW emission on the BH's semimajor axis and eccentricity following Peters & Mathews (1963). The characteristic timescale to merge a BH with an SMBH is given by:

$$\begin{aligned} t_{GW} &\approx 2.9\times10^{12}\ \mathrm{yr}\left(\frac{M_\bullet}{10^6\ \mathrm{M}_\odot}\right)^{-1}\left(\frac{m_{BH}}{10^6\ \mathrm{M}_\odot}\right)^{-1} \\ &\times \left(\frac{M_\bullet + m_{BH}}{2\times10^6\ \mathrm{M}_\odot}\right)^{-1}\left(\frac{a_\bullet}{10^{-2}\ \mathrm{pc}}\right)^{4} \\ &\times f(e_\bullet)(1-e_\bullet^2)^{7/2}\ , \end{aligned} \tag{4.9}$$

where $f(e_\bullet)$ is a function of $e_\bullet$. For all values of $e_\bullet$, $f(e_\bullet)$ is between 0.979 and 1.81 (Blaes et al., 2002). We plot this timescale for a $1\times10^5\,M_\odot$ BH in Figure 5.1 in blue.

In our simulations, we assume a BH has merged with the SMBH when the condition $t_{GW} <$

$t_{\rm elapsed}$ is met. When this condition is satisfied, we terminate mass growth through collisions for that BH.[4]

4.2.7 IMBH growth

As detailed above, BH-stellar collisions can increase the BH masses as a function of time. Here, we examine the sensitivity of the BH growth to the density power law. From Eq. (5.4), it is clear that the growth rate depends on the stellar density profile, governed by the index α. We expect that higher values of α, or steeper profiles, will result in more efficient mass growth. In Figure 5.1, larger values of α lead to collision timescales in the GN's inner region, inwards of 0.25 pc, that are much smaller that the 10 Gyr simulation time. Figure 4.3 confirms this expectation. It depicts the mass growth of a uniform distribution of BHs with initial conditions detailed in Section 4.2.1 for five α values, spanning 1 (green) to 2 (purple). The most massive IMBHs form inwards of 0.25 pc for the $\alpha = 2$ case.

4.2.8 Gravitational Wave Mergers and Intermediate and Extreme Mass Ratio Inspiral Candidates

Towards the SMBH, efficient collisions can create BHs massive enough to merge with the SMBH through GWs. Following the method detailed in Section 4.2.6, when a given BH meets the criterion $t_{\rm GW} < t_{\rm elapsed}$, we mark it as merged with the SMBH. We assume that at this point the dynamics of the BH will be determined by GW emission, shrinking and circularizing the BHs orbit until it undergoes an extreme or intermediate mass ratio inspiral (EMRI and IMRI, respectively). The righthand plot in Figure 4.3 shows the BH masses versus time of merger. It is interesting to note that even in the absence of relaxation processes, which are often invoked to explain the formation of EMRIs, EMRIs and notably IMRIs can form in this region.

[4]For comparison, we also incrementally changed the semimajor axis and eccentricity from GW emission following the equations in Peters & Mathews (1963). This method leads to a slight increase in the final IMBH masses because it accounts for the collisions that take place while the orbit is gradually shrinking.

4.2.9 Two Body Relaxation Processes

A BH orbiting the SMBH experiences weak gravitational interactions with other objects in the GN. Over a relaxation time, these interactions alter its orbit about the SMBH. The two-body relaxation timescale for a single-mass system is:

$$t_{\rm relax} = 0.34 \frac{\sigma^3}{G^2 \rho \langle M_* \rangle \ln \Lambda_{\rm rlx}}, \tag{4.10}$$

where $\ln \Lambda_{\rm rlx}$ is the Coulomb logarithm and $\langle M_* \rangle$ is the average mass of the surrounding objects, here assumed to be $1\,M_\odot$ (Spitzer, 1987; Binney & Tremaine, 2008, Eq. (7.106)). This equation represents the approximate timescale for a BH on a semi-circular orbit to change its orbital energy and angular momentum by order of themselves. The BH experiences diffusion in its angular momentum and energy as a function of time (depending on the eccentricity of the orbit, this process can be more efficient Fragione & Sari, 2018; Sari & Fragione, 2019). Relaxation can cause the orbit of an object in a GN to reach high eccentricities. If the object is a BH, it can spiral into the SMBH and form an EMRI, while a star can be tidally disrupted by the SMBH (e.g. Magorrian & Tremaine, 1999; Wang & Merritt, 2004; Hopman & Alexander, 2005; Aharon & Perets, 2016; Stone & Metzger, 2016; Amaro-Seoane, 2018; Sari & Fragione, 2019; Naoz et al., 2022). The relaxation process is therefore crucial to our study. In Figure 5.1, we plot the relaxation timescale in gold for a range of α. We note that the Bahcall & Wolf (1976) profile, $\alpha = 7/4$, corresponds to zero net flux and therefore does not preferentially migrate objects inward.

Additionally, because BHs are more massive on average than the surrounding objects, they are expected to segregate inwards in the GN (e.g., Shapiro & Marchant, 1978; Cohn & Kulsrud, 1978; Morris, 1993; Miralda-Escudé & Gould, 2000; Baumgardt et al., 2004). They sink toward the SMBH on the mass segregation timescale, $t_{\rm seg} \approx \langle M_* \rangle / m_{BH} \times t_{\rm relax}$ (e.g., Spitzer, 1987; Fregeau et al., 2002; Merritt, 2006), which is typically an order of magnitude smaller than the relaxation timescale plotted in Figure 5.1.

We incorporate relaxation processes by introducing a small change in the BH's energy and

angular momentum each time it orbits the SMBH. We apply a small instantaneous velocity kick to the BH, denoted as Δv. We draw Δv from a Guassian distribution with average of zero and a standard deviation of $\Delta v_{rlx}/\sqrt{3}$, where $\Delta v_{rlx} = v_\bullet \sqrt{P_\bullet / t_{rlx}}$ (see Bradnick et al., 2017, for an approach to changes in the angular momentum). The new orbital parameters can be calculated following Lu & Naoz (2019), and see Naoz et al. (2022) for the full set of equations.

We account for the effects of relaxation processes, including mass-segregation, using a multi-faceted approach. We begin by migrating each BH towards the center over its mass-segregation timescale, shifting it incrementally inward such that its orbital energy changes by order of itself within the segregation timescale.

As the BHs segregate down the potential well, their abundance with respect to stars increases, until at some turnover radius, BHs become the dominant source of scattering for both black holes and stars. Within this radius, BH self-interaction dominates over two-body scatterings with the now rarer main-sequence stars. The BHs will then settle onto a Bahcall-Wolf profile, while the stars may follow a shallower profile, with approximately $n_\star \propto r^{-1.5}$, inwards of the transition radius (Linial & Sari in prep.).

Therefore, after the initial mass segregation, we allow the BHs to begin diffusing over a relaxation timescale, their orbital parameters changing slowly through a random process. In this random process, some of the BHs may migrate closer to the SMBH. We terminate mass growth when the BH enters the inner 200 au of the GN, within which the density of stars is uncertain. This cutoff is based on the 120 au pericenter of S0-2, the closest known star to the SMBH (e.g., Ghez et al., 2005).

Another physical process that causes inward migration is dynamical friction. A cursory derivation based on the dynamical friction equations described in Binney & Tremaine (2008) reveals the process to have a similar timescale to mass segregation. If a BH diffuses to a

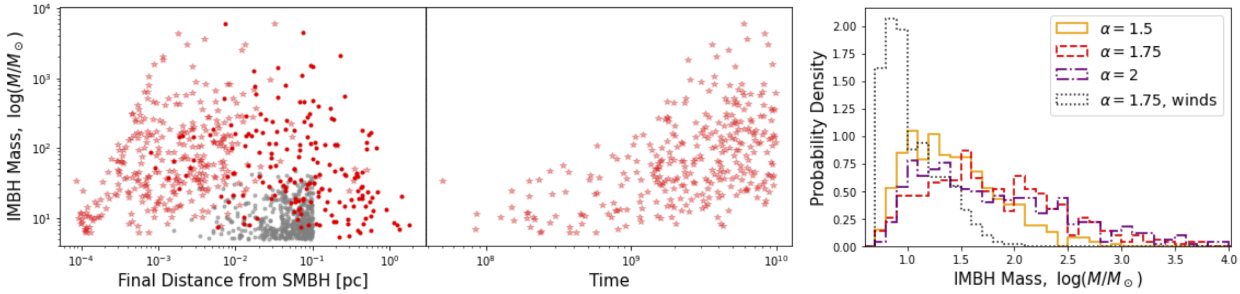

Figure 4.4: Similar to Figure 4.3, we plot the initial masses versus initial distance (grey) and final mass versus final distance (red) for 500 BHs. This simulation includes relaxation processes, including mass segregation, diffusion, and dynamical friction. We assume $\alpha = 1.75$ for the GN density profile. Faded stars represent BHs that merge with the SMBH. As a result of inward migration, BHs merge more quickly with the SMBH, before they can become as massive as those in Figure 4.3. Additionally, more BHs become EMRIs and IMRIs. Additionally, in the third panel, we show a histogram of the simulated IMBH masses for two different values of α, 1.5 (orange, solid), α, 1.75 (red, dashed), and 2 (purple, dash-dotted), accounting for relaxation processes. We also show the results for a simulation with $\alpha = 1.75$ that accounts for momentum-driven winds (black, dotted). Despite the substantially reduced accretion, BHs in the mass gap still form.

distance greater than 2 pc from the SMBH, exiting the sphere of influence, we have it sink inwards, back towards the center, over a dynamical friction timescale. After one dynamical friction timescale has passed, we restart diffusion.

We note that our prescription ignores self-interactions between the BHs. As mentioned above, as the BHs sink towards the SMBH, their concentration in the inner region of the GN increases, allowing them to dominate the scattering. We reserve the inclusion of these interactions for future study.

4.2.10 Effect of Relaxation Processes

As depicted in Figure 4.4, two-body relaxation processes result in more EMRIs and IMRIs events. These processes allow BHs that begin further from the SMBH to migrate inwards and grow more efficiently in mass. However, it also impedes the growth of BHs that are initially closer to the SMBH by allowing them to diffuse out of the inner region where collisions are efficient. As can be seen in Figure 4.4, the net result is that more BHs grow, but the maximum mass is lower compared to the scenario that ignores two-body relaxation. The

histogram in Figure 4.4 presents the final BH mass distributions for different power law indices α. As expected, the two-body relaxation suppresses the α dependence highlighted in Figure 4.3. In fact, using a KS test, we find that we cannot reject the hypothesis that the two distributions were drawn from the same sample for the $\alpha = 1.75$ and $\alpha = 2$ results. Interestingly, a BH mass IMF with an average of 10 $M_\odot$ leads to a final distribution with an average of ~ 200 $M_\odot$ and a median of ~ 45 $M_\odot$, which lies within the mass gap.

4.3 Discussion and Predictions

We explore the feasibility of forming IMBHs in a GN through successive collisions between a stellar-mass BH and main-sequence stars. Taking both a statistical and analytic approach, we show that this channel can produce IMBHs efficiently with masses as high as 10^{3-4} $M_\odot$ and may result in many IMBH-SMBH mergers (intermediate-mass ratio inspirals, or IMRIs) and EMRIs.

As the stellar mass BH collides with a star, the BH will grow in mass. The increase may equal star's entire mass if the relative velocity is smaller than the escape velocity from the BH at 1 $R_\odot$. However, near the SMBH, the velocity dispersion may be larger than the escape velocity from the BH at the star's radius. In this limit, the BH captures a "tunnel" of material through the star, estimated using Bondi-Hoyle-Lyttleton accretion. In our statistical analysis, we account for Bondi-Hoyle-Lyttleton accretion and find that BHs outside of 10^{-2} pc from the SMBH can capture the entire star (see Figure 4.2).

The efficiency of collisions, and therefore IMBH, EMRI, and IMRI formation as well, are sensitive to the underlying stellar density. As shown in Figure 4.3, a steeper density profile results in larger IMBHs. This behavior can be understood from the collision timescale's dependence on the stellar density profile. A steeper profile yields shorter collision timescales near the SMBH. However, the inclusion of relaxation processes in the simulations dampens the influence of the stellar density profile by allowing BHs to diffuse into regions of more

or less efficient growth. As a result, more BHs grow in mass, but their maximum mass is smaller ($\sim 10^4$ $M_\odot$). Additionally, the final masses have no apparent dependence on distance from the SMBH (see Figure 4.4).

Most simulations in our study assume that the BHs accrete all of the mass that they capture. The final BH masses can be taken as an upper limit. We note that the accretion is a highly uncertain process and represents an active field of study (e.g., Blandford & Begelman, 1999; Park & Ostriker, 2001; Narayan et al., 2003; Igumenshchev et al., 2003; Ohsuga et al., 2005; Yuan et al., 2012; Jiang et al., 2014; McKinney et al., 2014; Narayan et al., 2022). To assess the limits of our model, we also consider a physically motivated accretion model, momentum-driven winds (Section 4.2.5). We present the final mass distribution for momentum-driven winds in Figure 4.4. Importantly, we find that BHs within the mass gap still form naturally despite the substantially reduced accretion. About 5% of the BHs grow by 10 to 100 $M_\odot$. Furthermore, if we increase this ΔM estimate by a factor of 2 (i.e., use $\eta = 0.05$), the simulation produces a 3.5×10^3 $M_\odot$ IMBH for the same initial conditions. Our proof-of-concept demonstrates that collisions between BH and stars are an important process that should be taken into account in dense places such as a GN.

Mass growth through BH-main-sequence star collisions may act in concert with other IMBH formation channels, such as compact object binary mergers (e.g., Hoang et al., 2018; Stephan et al., 2019; Fragione et al., 2021; Wang et al., 2021). While in some cases collisions can unbind a binary (e.g., Sigurdsson & Phinney, 1993; Fregeau et al., 2004), BH binaries can be tightly bound enough to withstand the collisions. Wide binaries may also become unbound due to interactions with the neighboring stars and compact objects (e.g., Binney & Tremaine, 1987; Rose et al., 2020, see latter study for the timescale for an arbitrary eccentricity). However, as highlighted in previous studies, a substantial fraction of these binaries may merge due to the Eccentric Kozai Lidov mechanism, leaving behind a single star or a single compact object (e.g., Stephan et al., 2016, 2019; Hoang et al., 2018). Additionally, to be

susceptible to evaporation, BH binaries must have a wider configuration. Otherwise, they will be more tightly bound than the average kinetic energy of the surrounding objects and will only harden through weak gravitational interactions with neighboring stars (see for example Figure 6 in Rose et al., 2020).

We note that we assume a steady-state and treat the stars as a reservoir in this model. Future work will take a more nuanced approach to the background stars, whose density as a function of time can be influenced by several factors. Firstly, the relaxation of the stellar population occurs on Gyr timescales. Some studies have suggested that in situ star formation can occur in the Galactic Center as close as 0.04 pc from the SMBH (e.g., Levin & Beloborodov, 2003; Paumard et al., 2006), and star formation episodes can occur as often as every ~ 5 Myr (e.g. Lu et al., 2009). Therefore, we expect that after the first Gyr, stars within $\lesssim 0.01$ pc will be replenished at intervals consistent with the star formation episodes; the infalling populations of stars are separated by $\sim 5 - 10$ Myr, which is shorter than the collision timescale.

However, star-star collisions may complicate this picture within ~ 0.01 pc. As discussed above, regular star formation ensures the BHs always have a stellar population to interact with outside of ~ 0.01 pc.[5] At 0.01 pc, however, the kinetic energy during a collision between two 1 $M_\odot$ stars is larger than their binding energies. Collisions can therefore thin out the stellar populations during the time it takes them to diffuse to these small radii, $\lesssim 0.01$ pc, and may reduce the BH growth in the innermost region. We reserve the inclusion of star-star collisions for future work. We also note that the disruption of binary stars by the SMBH may help replenish the stellar population even as collisions work to deplete it (e.g., Balberg et al., 2013); when a binary is disrupted, one of the stars is captured on a tightly bound orbit about the SMBH.

[5]In fact, the star-star collision timescale is greater than 10 Myr for the entire parameter space, save at 0.001 pc for larger values of α; the BH-star collision timescale plotted in Fig. 1 is the same order of magnitude as the star-star collision timescale.

An IMBH may also affect the stellar density profile. As it spirals into the SMBH, it can perturb stellar orbits, and these interactions can lead to hypervelocity stars (e.g., Baumgardt et al., 2006a; Löckmann & Baumgardt, 2008). Löckmann & Baumgardt (2008) show that an IMBH can modify an initially steep stellar density profile to become consistent with the flatter cusp observed in the Galactic Center. The stars may then be replenished on 100 Myr timescales (Baumgardt et al., 2006a). Therefore, after the formation of the first few IMBHs, subsequent BH growth may occur in bursts, coinciding with replenishment of the stars.

While there are many competing dynamical processes that shape the stellar density profile, we stress that α can simply be chosen to encapsulate all of the relevant physics. A value for α that is constrained by observations must already reflect ongoing processes like star-star collisions and replenishment. Schödel et al. (2018) find the observed stellar mass enclosed within 0.01 pc of the Milky Way's Galactic Center to be approximately 180 $M_\odot$. This estimate is consistent to order of magnitude with our $\alpha = 1.25$ case. In a simulation like those depicted in Figure 4, which include relaxation, $\alpha = 1.25$ leads to a maximum IMBH mass of 140 $M_\odot$. Furthermore, while the stellar mass within 0.01 pc may be a few hundred $M_\odot$, Do et al. (2019) and GRAVITY Collaboration et al. (2020) set an upper limit on the mass enclosed within the orbit of S0-2 to be about a few thousand $M_\odot$, or 0.1% of the central mass. This upper limit can include mass that was previously in stars but is now in BHs. In that case, the 180 $M_\odot$ is what remains of the stars, while BHs and IMBHs make up the ~ 1000 $M_\odot$ in the innermost region.

Also not included in this study, collisions between the BH and other compact objects will increase the BH growth rate. BH-BH mergers (e.g., O'Leary et al., 2009; Fragione et al., 2021) and even neutron star BH mergers (e.g., Hoang et al., 2020) become more likely as the BHs increase in mass through stellar collisions. As a result, the BH-BH collision timescale, discussed in Section 4.2.2, will become relevant to our simulations, allowing the BHs to grow through this channel in addition to stellar collisions. Additionally, this compact object

mergers result in GW recoil, which may have a large impact on the dynamics (e.g., Baibhav et al., 2020; Fragione et al., 2021).

The BH's mass growth increases GW emission, which dissipates energy from the orbit. Along with relaxation, GW emission causes BHs to sink towards the SMBH and eventually undergo a merger. As a result, the GN environment is conducive to the formation of EMRIs and IMRIs. The GW emission from EMRIs and IMRIs is expected to be at mHz frequencies, making them promising candidates for LISA to observe. While the exact rate calculation is beyond the scope of this study, the mechanism outlined here seems very promising.

Our results also suggest that BHs within the mass gap as well as IMBHs likely exist in many galactic nuclei, as well as within our own galactic center. This implication seems to be consistent with recent observational and theoretical studies (e.g., Hansen & Milosavljević, 2003; Maillard et al., 2004; Gürkan & Rasio, 2005; Gualandris & Merritt, 2009; Chen & Liu, 2013; Generozov & Madigan, 2020; Fragione et al., 2020a; Zheng et al., 2020; Naoz et al., 2020; GRAVITY Collaboration et al., 2020).

Lastly, the collisions between stellar mass BHs and stars may contribute to the x-ray emission from our galactic centre (e.g., Muno et al., 2005, 2009; Hailey et al., 2018; Zhu et al., 2018; Cheng et al., 2018, see Kremer et al. (2022) for a discussion of electromagnetic signatures from BH-star collisions)[6]. These interactions, in particular grazing collisions, may also result in tidal disruption events (e.g., Baumgardt et al., 2006b; Perets et al., 2016; Stone et al., 2017; Samsing et al., 2019; Kremer et al., 2021). Thus, the process outlined here may produce electromagnetic signatures in addition to GW mergers.

[6]The connection between the observed X-ray sources at the Galactic Center and tidal capture has been suggested by Generozov et al. (2018), but see Zhu et al. (2018); Stephan et al. (2019) for alternative channels.

Acknowledgements

We thank the anonymous referee for useful comments. We also thank Jessica Lu, Fred Rasio, Kyle Kremer, Ryosuke Hirai, Ilya Mandel, and Erez Michaely for useful discussion.

SR thanks the Charles E. Young Fellowship, the Nina Byers Fellowship, and the Michael A. Jura Memorial Graduate Award for support. SR and SN acknowledge the partial support from NASA ATP 80NSSC20K0505. SN thanks Howard and Astrid Preston for their generous support. IL thanks support from the Adams Fellowship. SN and RS thank the Bhaumik Institute visitor program. This work was performed in part at the Aspen Center for Physics, which is supported by National Science Foundation grant PHY-1607611.

CHAPTER 5

Stellar Collisions in the Galactic Center

Like most galaxies, the Milky Way harbors a supermassive black hole (SMBH) at its center, surrounded by a nuclear star cluster. In this dense star cluster, direct collisions can occur between stars before they evolve off the main-sequence. Using a statistical approach, we characterize the outcomes of these stellar collisions within the inner parsec of the Galactic Center (GC). Close to the SMBH, where the velocity dispersion is larger than the escape speed from a Sun-like star, collisions lead to mass loss. We find that the stellar population within 0.01 pc is halved within about a Gyr because of destructive collisions. Additionally, we predict a diffuse population of peculiar low-mass stars in the GC. These stars have been divested of their outer layers in the inner 0.01 pc before migrating to larger distances from the SMBH. Between 0.01 and 0.1 pc from the SMBH, collisions can result in mergers. Our results suggest that repeated collisions between lower mass stars can produce massive ($\gtrsim$ 10 $M_\odot$) stars, and there may be $\sim$ 100 of them residing in this region. We provide predictions on the number of G objects, dust and gas enshrouded stellar objects, that may result from main-sequence stellar collisions. Lastly, we comment on uncertainties in our model and possible connections between stellar collisions and the missing red giants in the GC.

5.1 Introduction

Like most galaxies, the Mikly Way harbors a supermassive black hole (SMBH) at its center (e.g., Genzel et al., 2003; Ferrarese & Ford, 2005; Ghez et al., 2005; Kormendy & Ho, 2013).

A dense region of stars and stellar remnants, known as the nuclear star cluster, surrounds the SMBH (e.g., Schödel et al., 2003; Ghez et al., 2005, 2008; Gillessen et al., 2009, 2017). The proximity of the Milky Way's Galactic Center (GC) presents a unique opportunity to observe the consequences of this dense, dynamic environment. One such consequence is that direct collisions can occur between stars (e.g., Dale et al., 2009; Dale & Davies, 2006; Mastrobuono-Battisti et al., 2021; Rose et al., 2020, 2022). As we show below, any 1 $M_\odot$ star within about 0.1 pc of the SMBH experiences at least one collision over its lifetime. At 0.1 pc from the SMBH, the collision timescale is comparable to the main-sequence lifetime of a 1 $M_\odot$ star. Collisions are therefore essential to understanding the properties and demographics of the nuclear star cluster.

A number of studies have explored the effects of this dynamical process on the nuclear star cluster. For example, stellar collisions can modify the stellar density profile near the SMBH, where they deplete the stellar population (e.g., Duncan & Shapiro, 1983; Murphy et al., 1991; David et al., 1987a,b; Rauch, 1999; Freitag & Benz, 2002). Collisions have also been invoked to explain the dearth of 1-3 $M_\odot$ red giants (RGs) in inner 0.1 pc of the GC, a persistent observational puzzle (e.g., Genzel et al., 1996; Bailey & Davies, 1999; Buchholz et al., 2009; Do et al., 2009; Gallego-Cano et al., 2018; Schödel et al., 2018; Baumgardt et al., 2018; Habibi et al., 2019). Genzel et al. (1996) first suggested that RG collisions with main-sequence stars may destroy the RGs. However, theoretical studies diverge on whether such a collision can divest a RG of its envelope, with more recent work indicating insufficient mass loss post-collision (e.g., Alexander, 1999; Bailey & Davies, 1999; Dale et al., 2009, see the latter for discussion). Other mechanisms, such as black hole-RG collisions, RG encounters with stellar binaries, and a nuclear jet from the SMBH during its active phase, can only partly explain the apparent underabundance of RGs within 0.1 pc of the SMBH (e.g., Davies et al., 1998; Dale et al., 2009; Zajaček et al., 2020), though RG interactions with a gaseous disk in the GC represent a viable alternative explanation for their underabudance (e.g., Amaro-Seoane & Chen, 2014; Amaro-Seoane et al., 2020). The cause of the missing

RGs remains an open question, one which main-sequence stellar collisions may yet address (see Mastrobuono-Battisti et al., 2021, and our discussion in Section 5.7).

Collisions and mergers in the nuclear star cluster can also yield a wide range of observables (e.g., Amaro Seoane, 2023). Stellar collisions may be associated with several electromagnetic signatures, including AGN variability (e.g., Murphy et al., 1991; Torricelli-Ciamponi et al., 2000; Freitag & Benz, 2002), the presence of blue stragglers (e.g., Sills et al., 1997, 2001; Lombardi et al., 2002), and supernova-like explosions (Dale & Davies, 2006; Balberg et al., 2013). Furthermore, stellar mergers represent a possible explanation for the origin of G objects, stellar objects that are enshrouded by gas and dust observed in the nuclear star cluster (albeit secular binary mergers rather than impulsive collisions: Antonini et al., 2010; Witzel et al., 2014, 2017; Stephan et al., 2016, 2019; Ciurlo et al., 2020). Lastly, collisions between compact objects can release gravitational wave emission, potentially detectable by the LIGO-Virgo-KARAGA collaboration (e.g., O'Leary et al., 2009; Hoang et al., 2018, 2020; Arca Sedda, 2020).

Also with implications for gravitational wave sources, repeated collisions between stars and black holes (BHs) can cause the latter to grow in mass, producing more massive BHs than predicted by stellar evolution models (see Rose et al. (2022); for BH mass predictions, see also Heger et al. (2003); Woosley (2017); Spera & Mapelli (2017); Limongi & Chieffi (2018); Belczynski et al. (2020); Renzo et al. (2020)). However, for the BHs to grow significantly, there must be a sufficiently large population of stars to sustain the collisions. Star-star collisions may deplete this supply, especially in the region closest to the SMBH, $\lesssim 0.01$ pc, where BH-star collisions can act most efficiently to produce larger BHs (Rose et al., 2022). Therefore, understanding the impact of collisions on the stellar population has important implications for the compact object-star interactions that give rise to massive BHs and interesting electromagnetic signatures (for the latter, see Kremer et al. (2022)).

In this study, we consider the effect of stellar collisions on the masses and survival of stars in

the GC, with implications for the topics described above. We show that collisions between low-mass stars can give rise to a population of young-seeming, massive stars in the vicinity of the SMBH as well as peculiar low-mass stars that have been divested of their outer layers. Additionally, our results suggest that stellar collisions may explain observations of dust-enshrouded gaseous stellar objects and a missing red giant cusp in the Galactic Center. This paper is organized as follows: In Section 5.2, we describe our methodology. Many studies rely on smooth particle hydrodynamics (SPH) to determine the outcome of a collision, a complex problem that depends on assumptions about the stellar structure, impact velocity, and mass ratio of the stars (e.g., Benz & Hills, 1987; Lai et al., 1993; Rauch, 1999; Fregeau & Rasio, 2007; Kremer et al., 2020; Rodriguez et al., 2022). Given these uncertainties, we test different treatments of the mass loss and collision outcomes, documented in Section 5.2.3 and compare their results in Section 5.3. Section 5.4 and 5.5 present and discuss our findings in the context of the stellar demographics and mass function. Sections 5.6 and Section 5.7 discusses implications for the G object and RG populations, respectively. In Section 5.8, we summarize our findings.

5.2 Method

5.2.1 Initial Conditions

We follow a sample population of 1000 stars embedded in the nuclear star cluster. We draw the initial masses of our sample population using a Kroupa initial mass function (IMF). We limit the stars to masses between 0.5 and 100 $M_\odot$. However, in practice, the most massive stars in our simulations tend to be around 30 $M_\odot$ because of the steep IMF. The semimajor axes of the stars are drawn from a uniform distribution in log distance, i.e., one in which $dN/d(\log r)$ is constant. This distribution ensures adequate sampling at all distances from the SMBH, necessary to build comprehensive understanding of stellar collisions in the GC.

We draw the orbital eccentricities of the stars from a thermal distribution. While the young

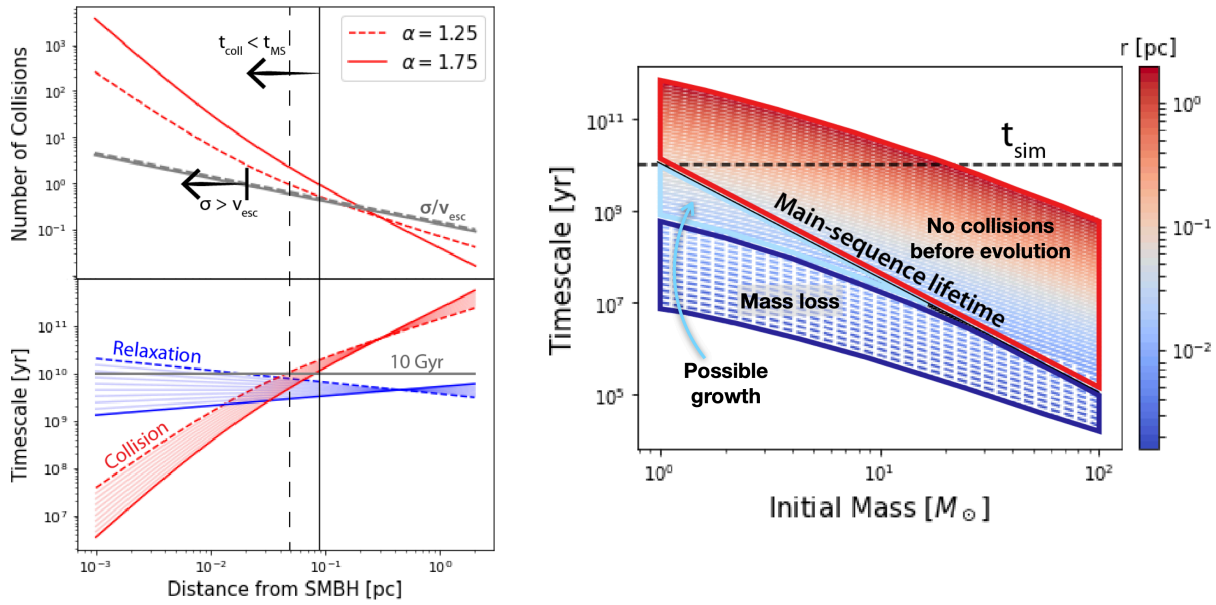

Figure 5.1: **Left lower panel:** We plot the relaxation (blue) and collision (red) timescales for a range of stellar density profiles, from $\alpha = 1.25$ (dashed) to 1.75 (solid). To guide the eye, we plot the approximate lifetime, 10 Gyr, of a solar mass star in grey. The dashed and solid lines indicate the distances from the SMBH at which the star's lifetime is equivalent to the collision timescale for the two stellar density profiles considered in this study. **Left upper panel:** We plot the approximate number of collisions, which is given by the main-sequence lifetime 10 Gyr divided by the collision timescale, as a function of distance from the SMBH. When this number is greater than one, it should be taken as an indicator of the importance of collisions, not the exact number of collisions that will occur, because this estimate assumes that the star's cross-section and mass remain unchanged following each collision. When this number is less than one, it is equivalent to the probability that a solar mass star will experience a collision over its lifetime. In grey, we also plot the velocity dispersion divided by the escape speed from a solar mass star. Where $\sigma > v_{\rm esc}$, collisions may result in significant mass loss. **Right panel:** Similar the lefthand plot, here we compare the collision timescale to other key timescales in our simulation. We calculate the collision timescale as a function of stellar mass and, by extension, stellar radius using Eq. (5.4). We plot this timescale for different distances from the SMBH, as indicated by the colorbar. The dashed black line represents maximum simulation time, 10 Gyr, while the solid black line shows the approximate main-sequence lifetime as a function of mass. Wherever the collision timescale is greater than these two timescales, the chances of a star experiencing a collision, based on its mass and location, are very low. Wherever the collision timescales is shorter than $t_{\rm MS}$, there is a high probability that a star will undergo one or more collisions over its lifetime. Dashed lines represent cases when the velocity dispersion exceeds the escape velocity from the star, a tracer for where collisions tend to be destructive. We have highlighted this region in dark blue.

stellar population has lower eccentricities on average than a thermal distribution (e.g., Yelda et al., 2014; von Fellenberg et al., 2022), the nuclear star cluster is dominated by an old population of stars, with ages on the order of Gyr (e.g., Chen et al., 2023). We therefore assume that the eccentricity distribution for most of the stars has been thermalized; the stars have had sufficient time to interact with one another and exchange energy. Additionally, the S-star cluster exhibits a thermal eccentricity distribution, which may have been achieved through relaxation processes within a 10^7 year timeframe (e.g. Gillessen et al., 2017; Generozov & Madigan, 2020). We explore deviations from an initial thermal eccentricity distribution in Appendix 5.9.2 and find that it has only a minor impact on our final results.

Each star in our sample population is influenced by the surrounding stellar cluster, which we treat as a reservoir. For simplicity, we assume that the surrounding stars have an average mass of 1 $M_\odot$, which remains constant over the duration of our simulation. This value is selected as a good approximation for the average stellar mass in a star cluster with a top heavy IMF, as has been observed in the nuclear star cluster (e.g. Paumard et al., 2006; Bartko et al., 2010; Lu et al., 2009, 2013; Alexander & Pfuhl, 2014).[1] We note that the IMF is not top heavy, perhaps with an average stellar mass closer to 0.33 $M_\odot$, then we are overestimating the amount of mass added to a star in a collision. However, over time, collisions will also change the average mass within the population. Heuristically, we expect that the average stellar mass doubles every collision timescale. The average stellar mass is therefore a function of both time and distance from the SMBH. Outside of 0.1 pc, it should be approximately constant.

We describe the density of the cluster as a function of $r_\bullet$, the distance from the SMBH, using

[1] A top-heavy IMF may be characteristic of star formation in the Galactic Center, an extreme environment in the gravitational potential of a SMBH (e.g. Hosek et al., 2019). In Section 5.5, we discuss the possibility that collision-induced mergers skew the stellar mass distribution towards higher masses. We note that these two explanations are not mutually exclusive.

a power law with the form:

$$\rho(r_\bullet) = \rho_0 \left(\frac{r_\bullet}{r_0} \right)^{-\alpha} , \tag{5.1}$$

where α determines the slope of the density profile. For the inner parsec of the GC, the density is normalized using the observationally-constrained values $\rho_0 = 1.35 \times 10^6 \, M_\odot/\mathrm{pc}^3$ at $r_0 = 0.25\,\mathrm{pc}$ (Genzel et al., 2010). For a uniform population of solar mass stars, the number density becomes:

$$n(r_\bullet) = \frac{\rho(r_\bullet)}{1\,M_\odot} . \tag{5.2}$$

Unless otherwise noted, we assume that the surrounding star cluster is dynamically relaxed, resulting in a cuspy Bahcall-Wolf profile (i.e., $\alpha = 1.75$ Bahcall & Wolf, 1976; Bar-Or et al., 2013; Alexander & Hopman, 2009; Keshet et al., 2009; Aharon & Perets, 2016). The true density profile in the GC may be shallower, with an index closer to 1.5 or 1.25 (e.g., Buchholz et al., 2009; Do et al., 2009; Bartko et al., 2010; Gallego-Cano et al., 2018, 2020; Schödel et al., 2014, 2018, 2020; Linial & Sari, 2022). Appendix 5.9.4 shows results that use $\alpha = 1.25$. The most realistic picture of the GC may lie somewhere between the $\alpha = 1.25$ and 1.75 results.

The mass of the SMBH $M_\bullet$ sets the velocity dispersion of the cluster:

$$\sigma(r_\bullet) = \sqrt{\frac{GM_\bullet}{r_\bullet(1+\alpha)}}, \tag{5.3}$$

where α is the slope of the density profile (Alexander, 1999; Alexander & Pfuhl, 2014). σ is approximately the orbital velocity. Together, the velocity dispersion and number density govern key physical processes like collisions because these properties determine the frequency of interactions between a star and its surrounding objects.

5.2.2 Direct Collisions

A star in the GC is expected to experience a collision over a characteristic timescale, t_{coll}. This timescale can be estimated using an $(n\sigma A)^{-1}$ rate calculation, where A is the cross-section of interaction and n and σ are determined by Eqs (5.1) and (5.3). The collision

timescale also has a weak dependence on eccentricity:

$$\begin{aligned} t_{\rm coll}^{-1} &= \pi n(a_\bullet)\sigma(a_\bullet) \\ &\times \left(f_1(e_\bullet) r_c^2 + f_2(e_\bullet) r_c \frac{2G(M_\odot + M)}{\sigma(a_\bullet)^2} \right) . \end{aligned} \tag{5.4}$$

where $f_1(e_\bullet)$ and $f_2(e_\bullet)$ are given by Rose et al. (2020), G is the gravitational constant, and r_c is the sum of the radii of the colliding stars.

We plot the collision timescale for different density profiles, spanning $\alpha = 1.25$ (dashed) to $\alpha = 1.75$ (solid), in red in the left bottom panel of Figure 5.1. In the left upper panel, we plot the number of collisions expected per star as a function of distance from the SMBH. The number of collisions per star are also plotted in red, with dashed and solid lines corresponding to the $\alpha = 1.25$ and $\alpha = 1.75$ density profiles, respectively. These curves assume a uniform population of solar mass stars. On the plot, we use grey vertical lines to mark the distance within which each star will experience at least one collision. This distance corresponds to where the collision timescale is equivalent to the main-sequence lifetime of a solar mass star. Outside of this distance, the number of collisions per star is less than one, indicating the probability that a single star will experience a collision or, equivalently, the fraction of the population that collides. In the upper panel, we also show the velocity dispersion as a function of distance from the SMBH in units of escape velocity from the star. Since we take the velocity dispersion to be the relative velocity of the two stars as they collide, this grey curve is a measure of how energetic each collision is. Where σ is greater than the escape speed from a solar mass star, we expect the collisions to be destructive, leading to mass loss. We discuss collision outcomes in greater detail in the next section.

In our simulations, we account for collisions using a statistical approach following Rose et al. (2022). Over a timestep Δt, the probability that a given BH will experience a collision is approximately $\Delta t / t_{\rm coll}$. We draw a random number between 0 and 1. If that number is less than or equal to the probability, we assume a collision has occurred. We adjust the mass of the star accordingly and repeat this process until the simulation has reached the desired

total time, 10 Gyr. As in Rose et al. (2022), we use a timestep of 1×10^6 yr.

5.2.3 Collision Outcomes

5.2.3.1 General Overview

The outcome of a direct collision between two stars depends on many factors, including the velocity dispersion, the impact parameter, and assumptions about the stellar structure (e.g., Lai et al., 1993; Freitag & Benz, 2005). Given the uncertain outcome of stellar collisions, especially at high velocities, we explore a range of possibilities, varying our treatment of the mass loss and merger products. Broadly, there are two possible outcomes of a collision.

1. **Merger:** In this case, the star in question gains a solar mass. We reiterate that in our toy model, the surrounding cluster contains only 1 $M_\odot$ stars, while the masses of our sample are drawn from a Kroupa IMF. From the merger product, some mass may be ejected depending on the nature of the collision. We estimate the final mass M_f of the star as $M_f = M_i + 1 - f_{ml}(M_i + 1)$, or $M_f = (1 - f_{ml})(M_i + 1)$, where M_i is the stellar mass before the collision took place and f_{ml} is the fractional mass loss caused by the collision, discussed in greater detail below.

2. **Mass Loss Only:** In the second case, there is no merger – the primary star fails to capture the collider – but the star still loses some fraction of its mass following the impact. Its final mass equals $(1 - f_{ml})M_i$.

In the following subsections, we detail different physically motivated approaches to estimating the fractional mass loss. Following a collision, we recalculate the radius of the star using its updated mass. The thermal timescale is short enough (10^7 yr or shorter) for us to take the radius of a main-sequence star, except for the low mass (< 1 $M_\odot$) stars. At 0.01 pc, approximately the innermost radius where we expect mergers to occur (see Figure 5.2), the collision timescale is more than ten times longer than a thermal timescale of 10^7 yr. As

the collision timescale is inversely proportional to R^2 and the Kelvin-Helmholtz timescale depends on $1/R$, the radius of the merged star must be inflated to ten times its initial value for these timescales to be comparable. Our default merger conditions require the relative velocity between the colliders to be less than the escape velocity from the star (see Section 5.2.3.3). For this reason, the degree of inflation post-collision should be not so extreme, and most of the star's mass should remain concentrated towards the center (e.g., Lai et al., 1993). We therefore conclude that the stars will have time to recollapse before they experience another collision. For the low-mass stars, however, the thermal timescale may be longer than the collision time, meaning the stars remain distended when the next collision occurs. The larger radius than accounted for in our model may hasten their destruction.

Irrespective of the specific prescription adopted for f_{ml}, we can make predictions about where in the GC certain outcomes are likely to occur. Figure 5.1, right panel, illustrates the parameter space in which different outcomes are expected. In particular, the right plot shows the collision timescale as a function of the star's mass at different distances from the SMBH. Each collision timescale curve is color-coded according to distance from the SMBH as indicated by the color bar on the left side of the plot. We also include the main-sequence lifetime as a function of stellar mass (solid black line) and the simulation time of 10 Gyr (dashed black line). The region highlighted in red represents a regime in which most stars will evolve off the main-sequence before a collision can occur. On the other hand, when the collision timescale is less than the main-sequence lifetime, stars may experience one or more collisions before evolving off the main sequence. The regime highlighted in dark blue in the right hand plot represents the scenario where the dispersion velocity on the onset of the collision is larger than the escape velocity of the two colliding stars (i.e., $\sigma > v_{\rm esc}$). Thus, we expect collisions to result in significant mass loss from the stars and no mergers to occur. However, in the small light blue wedge, the dispersion velocity is smaller than the escape velocity, and collisions may result in mergers and mass growth. As mentioned above, the details of the mass loss and growth are uncertain, and we consider several scenarios below.

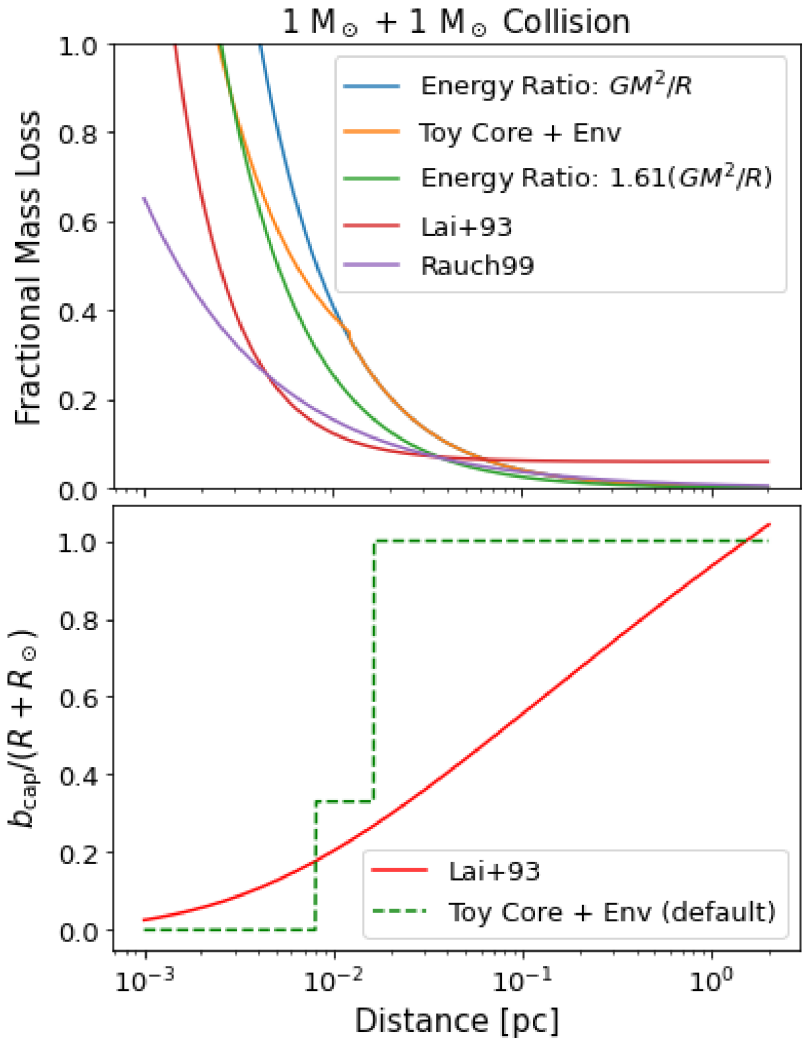

Figure 5.2: **Upper Panel:** The fractional mass loss expected from a head-on collision between two solar mass stars is plotted as a function of distance from the SMBH for different models. This is the maximum fractional mass loss that can be produced by a collision between Sun-like stars; an impact parameter larger than zero can only result in less mass loss. The blue line estimates the f_{ml} using Eq. 5.5, where the binding energy of the stars is approximated as GM^2/R. The green curve uses a similar estimate, but includes a prefactor in the binding energy to account for the fact that the stellar density increases near the core. The orange curve combines these two estimates to construct a toy model of the star: it has a loosely bound "envelope" containing about 30 % of the star's mass and a more tightly bound "core." The red and purple curves use the fitting formulae from Lai et al. (1993) and Rauch (1999), respectively. **Lower Panel:** Here we show the two different prescriptions we use to determine whether a merger occurs following a collision or, in other words, whether the stars manage to capture each other after impact. The red curve is based on the fitting formulae from Lai et al. (1993), while the green, dashed curve shows the toy model approach taken in most of our simulations. The latter model compares the escape speed from the "core" and surface of the star to the velocity dispersion in order to determine whether a merger occurs. This prescription is used in all simulations except those specifically labeled as "Lai+93".

5.2.3.2 Energy Ratio Estimate of the Mass Loss

The fractional mass loss can be approximated as the ratio of the kinetic energy to the binding energy of the two colliding stars:

$$f_{ml} = \frac{\mu\sigma^2}{GM_i^2/R_i + GM_\odot^2/R_\odot}, \tag{5.5}$$

where μ is the reduced mass of the two colliding stars and M_i and R_i are the mass and radius of the star from our sample population. This equation is roughly consistent with equations presented in the qualitative overview of collisions in Lai et al. (1993), with some adjustments to make the fractional mass-loss unitless. The aforementioned study includes a parameter β in the denominator of f_{ml}, a variable that accounts for the gas pressure in the star. While β is order unity for solar mass stars, radiation pressure becomes important for more massive stars; it is easier to unbind material from them during a collision (Lai et al., 1993). The main-sequence lifetime for these massive stars, however, is short compared to the collision timescale. Their low probability of experiencing a collision means that our assumption that $\beta = 1$ does not significantly impact our results.

Stars are not uniform density spheres; in fact, most of a star's mass is concentrated near its center, leading to a higher binding energy than the estimate in the denominator of Eq. 5.5 (e.g., Christensen-Dalsgaard et al., 1996). To illustrate this point, we plot of the mass enclosed as a function of radius within the Sun based on Christensen-Dalsgaard et al. (1996) in Figure 5.10 (see Appendix 5.9.1). A spherical object with this mass profile has binding energy $1.61GM^2/R$. For a slightly more accurate estimate of the fractional mass loss, we include this prefactor, 1.61, in Eq. 5.5. In Figure 5.2, we plot the fractional mass loss with and without the prefactor in green and blue, respectively, for a collision between two 1 $M_\odot$ stars. The fractional mass loss decreases with distance from the SMBH because it depends on the velocity dispersion.

In this prescription, if $\sigma < \sqrt{2GM/R}$, roughly the escape velocity from the stars, we assume that a merger occurs (see Figure 5.1). Otherwise, we calculate the final mass of the star as

$M_{\rm post} = M(1 - f_{ml})$. This prescription over-predicts the amount of mass lost for reasons discussed in Section 5.2.3.4.

5.2.3.3 Toy Core+Envelope Model

The purpose of this toy model is to provide physical insight into the outcome of stellar collisions. Most of a star's mass is concentrated at its center. As a result, the escape velocity from the surface of the star may be much lower than that from the core, a subtlety not fully encapsulated by the approximations in Section 5.2.3.2. Here we construct a more nuanced toy model based on the internal structure of the Sun (e.g., Christensen-Dalsgaard et al., 1996). Based on the mass enclosed, $M_{\rm enc}$, within a radius r in the Sun, we calculate the escape velocity from a sphere with equivalent mass and radius, $v_{\rm esc} = \sqrt{2GM_{\rm enc}/r}$, as a function of r. We determine that this $v_{\rm esc}$ reaches a maximum of about 800 km/s at $R = 0.33R_\odot$ (see Figure 5.10 and Appendix 5.9.1). This radius encloses almost exactly two thirds of the Sun's mass. We define this region as the "core," though we stress that it is not representative of the true core of the Sun; in our simple model, there is a tightly bound inner part of the star and a more loosely bound outer "envelope."

We calculate the fractional mass loss as follows. We begin by calculating the ratio of the kinetic energy to the binding energy of the stars as in Eq. (5.5). We then take the maximum between the corresponding change in mass and the mass of the "envelope," 0.33 $M_\odot$. If the kinetic energy is greater than the binding energy of the envelope, we assume the remaining kinetic energy can go into ejecting material from the more tightly bound "core." In other words, if the collision has enough energy to unbind more than the outer third of the star's mass, the total mass lost equals:

$$M_{\rm lost} = M_{\rm env} + \frac{\mu\sigma^2/2 - U_{\rm env}}{GM_{\rm core}^2/R_{\rm core}} \ , \tag{5.6}$$

for a collision between two 1 $M_\odot$ stars. As noted above, in this equation $M_{\rm core}$ is about 0.66 $M_\odot$ and $R_{\rm core}$ is about $0.33R_\odot$. In Figure 5.2, we plot the fractional mass loss in orange.

The main advantage of this prescription is that it can be expanded to account for an impact parameter. From a geometric standpoint, head-on collisions are unlikely. Collisions with a non-zero impact parameter result in less mass loss because only the outer envelopes of the stars interact, while most of the mass is concentrated in the core. Accounting for the impact parameter, b is therefore crucial in this work. We draw an impact parameter between zero (a head-on collision) and the sum of the two stellar radii in question, $R + R_\odot$ (a grazing collision) using a probability density that goes as $b^2/(R + R_\odot)^2$.

In our simple model, during a collision with $R_{\rm core} < b$, only the envelopes interact, and there cannot be any additional mass loss from the core. On the other hand, any collision with an impact parameter smaller than the core radius can result in mass loss from this region. Additionally, in this prescription, there are two sets of conditions that, when met, result in a merger: $b < 2R_{\rm core}$ and $\sigma < v_{\rm esc,core} \sim 800$ km/s, or $2R_{\rm core} < b < 2R_\odot$ and $\sigma < v_{\rm esc,surface} \sim 600$ km/s. Note that this formula for drawing the impact parameter does not account for gravitational focusing, which can make head-on collisions more likely and lead to slightly higher fractional mass loss.

In order to expand this approach to stars of different masses, we assume that all stars have a similar structure to our Sun, allowing us to scale the quantities described above. In other words, we calculate the binding energy of the star as $1.61GM^2/R$, and assume that about two thirds of the star's mass is concentrated in the inner one third of the radius. While the true structure of a star depends on its mass, which determines the convective regions, stars with $M \gtrsim 1$ M$_\odot$ have a similar structure. Massive stars ($M \gtrsim 10$ M$_\odot$) have convective cores. However, their shorter main-sequence lifetime coupled with their low abundances in our sample means that very few of them collide. Future work may consider a more accurate approach to stars of other masses, perhaps by using different polytropic indices as was done by Rubin & Loeb (2011), but for the purposes of this study, the approach detailed above provides a simple mass-loss recipe that complements the other prescriptions used in this

study (see Figure 5.2).

5.2.3.4 Fitting Formulae

In other simulations, we rely on fitting formulae from on smooth-particle hydrodynamics (SPH) studies of collisions at high velocities. Considering collisions in galactic nuclei, Lai et al. (1993) explores a wide variety of relative velocities, mass ratios, and impact parameters. This study provides a variety of fitting formulae, physically reasoned and based on their numerical results, that calculate the fractional mass-loss and determine whether or not a collision results in a merger. Specifically, we use their equations (4.4) and (4.8)-(4.10) and the fitting parameters in their Table 1. We label simulations that use these fitting formulae as "Lai+93".

As an alternative, we also use the fitting formulae in Appendix B of Rauch (1999). Based on a set of SPH simulations for high impact velocities by M. Davies, equation B1 relates the fractional mass loss of the two stars in question using their mass ratio, and equation B2 calculates the total fractional mass loss from the system in terms of the impact parameter, mass ratio, and relative velocity. The label "Rauch99" denotes simulations in this paper that use these equations.

In Figure 5.2, we plot the fractional mass loss expected from these fitting formulae for a head-on collision ($b = 0$) between two 1 $M_\odot$ stars as a function of distance from the SMBH. The equations from Rauch (1999) generally give a lower fractional mass loss than the other models used in this work.[2]. We note that both Rauch (1999) and Lai et al. (1993) assume that stars are polytropes, which may provide an incomplete picture of the full range of collision outcomes (Freitag & Benz, 2005). Additionally, Rauch (1999) note the difficulties in determining the post-collision radius of the star and approximate it as being equal to that

[2]For additional comparisons of these mass-loss predictions with other studies, please see figures 5 and 6 in Rubin & Loeb (2011) and figures 12 and 13 in Freitag & Benz (2005)

of a main-sequence star with the same mass, an approach that is consistent with ours.

In the bottom panel of Figure 5.2, we also plot the maximum impact parameter, $b_{\rm max}$, that will result in a merger as a function of distance from the SMBH, which acts as a proxy for the velocity dispersion. The red line uses the fitting formala provided in Lai et al. (1993), while the green dashed curve represents our simple toy model approach, used as the default in all of our other simulations. Unlike Lai et al. (1993), whose equations give the specific impact parameter needed to achieve a merger at a given impact velocity, Rauch (1999) use an escape velocity argument to determine whether or not a merger occurs, much like our own toy model. We therefore adopt the conditions described in Section 5.2.3.3 (green dashed line in the bottom panel of Figure 5.2) to determine whether or not a collision results in a merger in Rauch99 simulations. These conditions lead to more mergers overall than the Lai et al. (1993) fitting formula. However, as noted in Section 5.2.3.3, our formula for drawing the impact parameter does not account for gravitational focusing, which makes head-on collisions more likely. Our Lai+93 simulations may therefore underestimate the number of mergers because of the stricter $b_{\rm max}$ condition. Our Rauch99 simulations, which use the less restrictive $b_{\rm max}$ merger conditions, may provide a more accurate picture of mergers outside of 0.02 pc, where gravitational focusing becomes increasingly important.

5.2.4 Two-Body Relaxation

As a star orbits the SMBH, it will experience frequent weak gravitational interactions with passing objects. Over time, the small effects of these interactions accumulate, altering the star's orbit. This process is known as relaxation and acts over an associated timescale, $t_{\rm rlx}$, the amount of time needed for the star's orbital energy to change by order of itself (e.g., Binney & Tremaine, 2008):

$$t_{\rm rlx} = 0.34 \frac{\sigma^3}{G^2 \rho \langle M_* \rangle \ln \Lambda_{\rm rlx}} \ , \tag{5.7}$$

In Figure 5.1, the blue lines show this timescale as a function of distance from the SMBH for a range of stellar density profiles.

We simulate the effects of relaxation in our code. Over each timestep, we apply a small instantaneous velocity kick to the star, from which we calculate the new, slightly altered orbital parameters (see Lu & Naoz, 2019; Naoz et al., 2022, for the full set of equations). The velocity kick is drawn from a Gaussian distribution with a standard deviation $\Delta v_{rlx}/\sqrt{3}$, where $\Delta v_{rlx} = v_{\rm orbital}\sqrt{P_{\rm orbital}/t_{rlx}}$ (e.g., Bradnick et al., 2017; Rose et al., 2022; Naoz et al., 2022). Here, $v_{\rm orbital}$ and $P_{\rm orbital}$ are the orbital speed and period of the star in question. This prescription allows us to account for changes in the orbital parameters over time from interactions with the surrounding stars.

We note that we do not include resonant relaxation processes, which change the magnitude and orientation of an orbit's angular momentum vector (e.g., Rauch & Tremaine, 1996; Hopman & Alexander, 2006a; Kocsis & Tremaine, 2011). However, we do not consider any orbital inclinations as our models assume a spherically symmetric nuclear star cluster. Additionally, while scalar resonant relaxation may change the eccentricity of the orbit faster than standard two-body relaxation (e.g., Bar-Or & Fouvry, 2018), we show in Appendix 5.9.2 that the orbital eccentricities have a weak effect on the final simulation results.

5.2.5 Stopping Conditions

At each timestep in our code, we calculate the star's main-sequence lifetime, $t_{\rm MS}$, according to its present mass: $t_{\rm MS} = 10^{10}(M/M_\odot)^{-2.5}$. When a star's age exceeds its main-sequence lifetime, we terminate the simulation. In the case of a merger, we calculate the new age of the merged product using a "sticky-sphere model" (see, e.g., Kremer et al., 2020). Mixing during the collision and merger can introduce a fresh supply of hydrogen to the core, extending the lifetime of the merged star. The dimensionless parameter $f_{\rm rej}$, ranging from 0.1 to 1, quantifies the degree of mixing and therefore the degree of rejuvenation (e.g., Hurley et al.,

2002; Breivik et al., 2020). While the true value of $f_{\rm rej}$ is challenging to ascertain since it can depend on the details of each collision and stellar structure, we adopt the $f_{\rm rej} = 1$, the most conservative value. The new age of the star, $t_{\rm age,f}$, can be calculated as follows:

$$t_{\rm age,f} = f_{\rm rej} \frac{t_{\rm MS,M+M_\odot}}{M + M_\odot} \left(\frac{M \times t_{\rm age,i}}{t_{\rm MS,M}} + \frac{M_\odot \times t_{\rm sim}}{t_{\rm MS,\odot}} \right). \tag{5.8}$$

Above, $t_{\rm age,i}$ is the age of the star in question before it collides with a solar mass star – recall that we assume that solar mass stars comprise the surrounding cluster – and $t_{\rm MS,M}$ is its main-sequence lifetime. The star with which it collides has main-sequence lifetime $t_{\rm MS,\odot}$ and age equal to the time ellapsed in the simulation, $t_{\rm sim}$. $t_{\rm MS,M+M_\odot - M_{lost}}$ denotes the main-sequence lifetime of the merger product. Our simulations consider only one population of stars, whose age is set by the time elapsed in the simulation. However, in the actual nuclear star cluster, star formation episodes may replenish the stellar population. Observations suggest two major star formation episodes in the Galactic Center, separated by Gyrs (e.g., Chen et al., 2023). If a star from the older, evolving population collides with a younger star, as opposed to one from its own formation episode, the merger product will be even more rejuvenated. We may therefore be underestimating the degree of rejuvenation and new stellar lifetime in a small fraction of the collisions. These longer-lived stars may go on to experience more collisions.

In addition to the stellar age, we include two other stopping conditions in our code. Relaxation processes may drive a star's orbital eccentricity to high values, shrinking its pericenter passage to fall within the tidal radius of the SMBH. We include a stopping condition to account for these tidally disrupted stars:

$$a(1-e) < R(2M_\bullet/M)^{1/3}. \tag{5.9}$$

Lastly, some stars undergo significant mass loss through one or more collisions. The code terminates once the mass of a star falls below 0.1 $\rm M_\odot$.

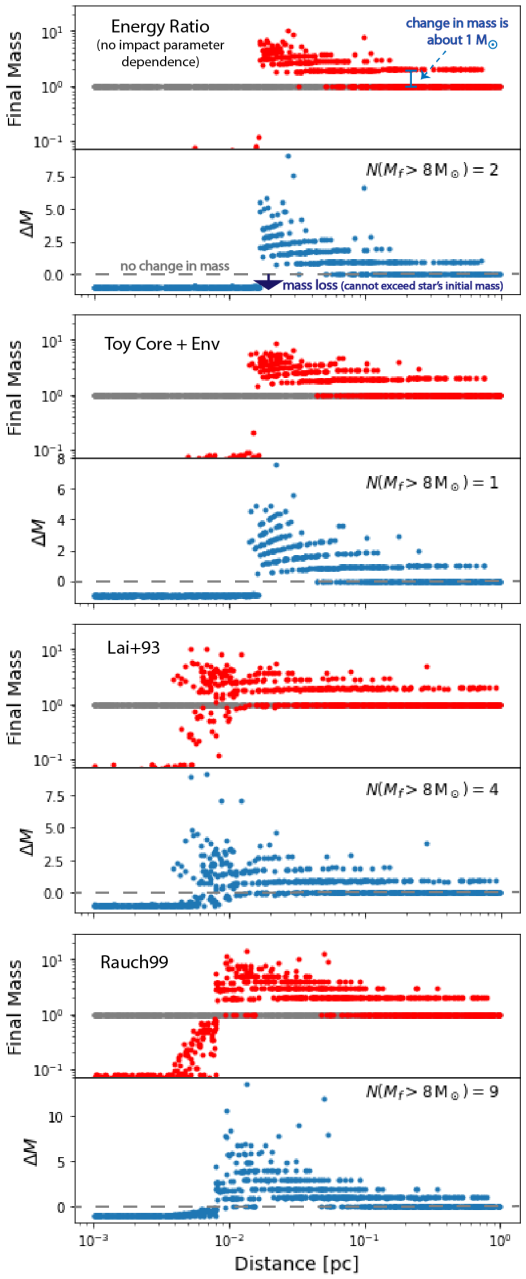

Figure 5.3: We compare simulated results for different fractional mass loss recipes. So that the differences are easy to discern, we do not include relaxation in these simulations. We begin with a uniform population of 1 $M_\odot$ stars distributed uniformly in log distance from the SMBH. Grey dots represent the initial masses and distances. From top to bottom, we show simulation results using an energy ratio estimate for the fractional mass loss (Section 5.2.3.2), a toy core plus envelope model for the stars (Section 5.2.3.3), and fitting formulae from comprehensive studies of collisions using SPH simulations (Section 5.2.3.4). The final masses are shown in red in the upper panels, and the blue dots in the lower panels represent the change in mass of each star.

5.3 Comparing Mass Loss Prescriptions: Low Mass Remnants and Massive Merger Products

We begin by comparing the different mass loss prescriptions detailed in Sections 5.2.3.2, 5.2.3.3, and 5.2.3.4. We therefore run several simulations with a sample population of only 1 $M_\odot$ stars and identical initial conditions, constraints we later relax in Section 5.5. At this stage, we do not include relaxation in order to build a clear picture of the differences between our mass loss prescriptions. Figure 5.3 juxtaposes the results. The initial conditions, 1000 solar mass stars distributed uniformly in log distance from the SMBH, are shown in grey, while red dots show the final masses versus distance from the SMBH. The blue dots show the total change in each star's mass over the simulation. Each row corresponds to a different mass loss prescription, indicated by the label in the left corner.

All of the mass loss prescriptions yield qualitatively similar results, consistent with the expectations from Figure 5.1. Close to the SMBH, collisions work to destroy the stars, while $\sim$ 1 pc from the SMBH few collisions occur. In between these two extremes, one or more collisions occur, and they result in mergers. Generally, our results suggest that multiple collisions between 1 $M_\odot$ stars can produce more massive stars. These massive products are localized between 0.01 and 0.1 pc from the SMBH. In this region, a few conditions must align to support the formation of massive stars. Firstly, the collision timescale is shorter, in some cases by an order of magnitude, than the main-sequence lifetime and several collisions can take place. Secondly, the velocity dispersion is small enough that stars can capture each other and the factional mass loss is low. The final mass of the stars formed through collisions therefore depends on the specific mass loss prescription adopted.

For these initial conditions, all of our mass loss prescriptions can produce a > 8 $M_\odot$ star. However, the Rauch99 prescription was the only one to do so consistently. This outcome is not surprising given that the Rauch99 equations result in less mass loss compared to the others (see Figure 5.2), producing more massive stars. Over several Rauch99 simulations with

1000 solar mass stars each, we find that a few stars out of the 1000 will exceed 10 $M_\odot$ through mergers with other low-mass stars. We scale this number using a realistic density profile normalized by the M-σ relation (Bahcall & Wolf, 1976; Tremaine et al., 2002). Accounting for the number of stars residing between 0.01 and 0.1 pc in the Galactic Center, we estimate that there may be more than $\sim$ 100 stars over 10 $M_\odot$ formed through collisions between lower mass stars. This estimate assumes that collisions tend to produce less mass loss, as in the Rauch99 prescription, and result in only moderate rejuvenation ($f_{\rm rej} = 1$ in Eq. 5.8). If mergers in the Galactic Center are more effective at rejuvenating stars, then collisional processes should lead to even more massive stars and in greater abundance.

Another difference between mass loss prescriptions is their ability to produce low mass remnants. Often, a collision within $\sim$ 0.01 pc of the SMBH, where the velocity dispersion is high, will only remove the outer layers of a star. This outcome is common because most collisions have a non-zero impact parameter (see also discussion in Rauch, 1999). The contrast between the upper row and last two rows in Figure 5.3 illustrate the importance of the impact parameter. The upper row does not include an impact parameter dependence, and as a result it overestimates the number of stars that are destroyed. Rauch99, on the other hand, predicts many low-mass collision remnants, a result discussed in their original study, Rauch (1999). The evolution of these remnants post-collision is uncertain. However, from a dynamical standpoint, these objects may be long-lived. Their small cross-section leads to a longer collision timescale, making it less likely that they will undergo another destructive encounter.

5.4 The Effect of Relaxation

In the previous section, we demonstrate that the general collision outcome trends described in Figure 5.1 hold. Relaxation has the potential to complicate the physical picture, however, by allowing stars to diffuse into different regions from the SMBH. We show the effects of this

dynamical process in Figure 5.4. The simulations shown in the Figure use identical initial conditions as those in last two rows of Figure 5.3, except with the addition of relaxation. One main difference is that due to two-body relaxation, low mass remnants can migrate out of the region in which they form, around 0.01 pc, to larger distances from the SMBH. We therefore predict a diffuse population of peculiar low-mass stars throughout the GC. In contrast, stars that experience the most mass growth are still localized to 0.01-0.1 pc from the SMBH. These stars must form in this region because otherwise either the collision timescale is too long to achieve multiple mergers, or the collisions are destructive in nature. Additionally, as a star grows in mass, its main-sequence lifetime becomes short compared to the relaxation timescale (Figure 5.1). As a result, the most massive stars have insufficient time to diffuse out of the region in which they form. We therefore expect massive stars formed through stellar collisions to be limited within $\lesssim 0.1$ pc from the SMBH.

5.5 Stellar Demographics

Thus far, we have considered only uniform populations of 1 $M_\odot$ stars. In this section, we use a Kroupa IMF to generate our initial conditions and explore general trends in the stellar mass distributions. We consider two mass-loss prescriptions, Lai+93 and Rauch99, because they encapsulate the range of results in Figure 5.3. Recall that Rauch99 favors mergers with minimal mass loss, while the Lai+93 equations lead to greater mass loss and have a stricter merger condition.

Figure 5.5 shows the results of two simulations, Rauch99 on the left and Lai+93 on the right, with the aforementioned initial conditions. In the bottom row, we plot the final masses and semimajor axes of the stars in red and the initial masses and semimajor axes in grey. The bottom row also shows the change in mass of each star versus its initial position. For effective visualization, we divide the nuclear star cluster into three regions that roughly correspond to different collision outcomes based on Figure 5.1. The regimes are:

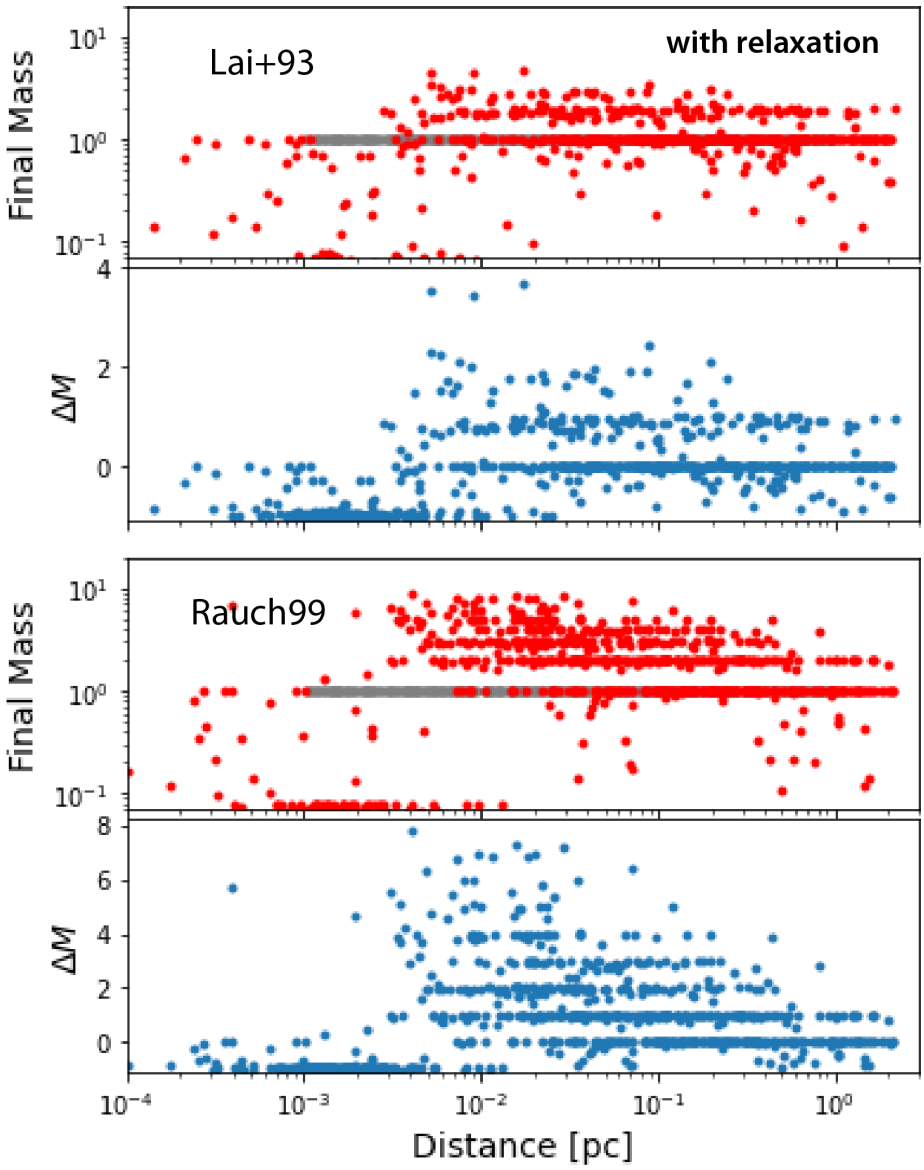

Figure 5.4: The same as the third and fourth row of Figure 5.3, but with the addition of relaxation. We begin with a uniform stellar population of solar mass stars distributed uniformly in log distance from the SMBH.

- $r < 0.01$ pc (top row, light blue border), where the velocity dispersion is high and we expect repeated collisions lead to mostly destruction of stars.

- $0.01 < r < 0.1$ pc (middle row, dark blue border), where the velocity dispersion and relatively short collision timescale allows mergers to take place.

- $0.1 < r < 2$ pc (third row, red border). In this regime, while the velocity dispersion allows mergers to take place, the collision timescale is longer than the stellar lifetimes. The number of collisions is therefore low.

These three rows in Figure 5.5 depict the the number of stars within a certain mass range as a function of time. The solid lines represent the expectation in the absence of collisions. The solid lines decrease when stars within each mass range reach the end of their main-sequence lifetimes. The symbols show stellar abundances when collisions are included in the simulation. In the bottom row of the figure, we also include plots in the style of Figure 5.4 with the different regimes highlighted to guide the eye.

In the first region (top row), the populations of all the low mass stars decline over time. Collisions destroy these stars before the can evolve off the main-sequence. However, multiple collisions are required in order to destroy the stars. As can be observed in the figure, it takes about one billion years to halve the population of low-mass stars in both the Rauch99 and Lai+93 simulations. This half-life is about an order of magnitude longer than the collision timescale. We attribute this longevity to the fact that most collisions are not head-on and therefore less destructive. Additionally, stars losing mass through collisions can temporarily increase the number of stars in a lower mass range. For example, as 1-1.5 $M_\odot$ stars lose mass, they will temporarily increase stars in the 0.5-1 $M_\odot$ mass range.

Between 0.01 and 0.1 pc, the number of stars in the ranges $M < 1$ $M_\odot$ and 1-1.5 $M_\odot$ still decrease. However, while some of these stars may undergo destructive collisions, it is apparent from the final masses, as shown in the last row of the figure, that their changes in

number are due mostly to mergers. This can be seen most clearly in the Rauch99 simulation, where there is a visible increase in the number of 1.5-3 $M_\odot$ stars such that they outnumber the 1-1.5 $M_\odot$ stars. Additionally, increasing the mass of the stars even slightly causes the stars to evolve off the main-sequence more quickly. As a result, the red symbols, for example, decrease more quickly compared to the expectation based on the original population (solid line). The Lai+93 prescription leads to more moderate mass growth than the Rauch99 one. As a result, the faster decline of the 1-1.5 $M_\odot$ stars than expected is likely due to accelerated evolution, not stars leaving this mass range entirely. Lastly, in the $0.1 < r < 2$ pc, similar effects from mergers are present, but to a far lesser degree.

We suggest that collisions may result in more massive, young-seeming stars. In particular, because collisions need time to act, a massive stellar population may emerge after about a Gyr. This emergent population skews towards higher masses, yielding a mass function that resembles a top heavy one. This behaviour is depicted in Figure 5.6, which shows stellar mass distribution for a few representative snapshots in time. In this Figure, we again show our two main simulations, also depicted in Figures 5.4 and 5.5, in the left and right columns. The simulation shown in the middle column is identical to the Rauch99 simulation on the left, except the initial distances from the SMBH of the 1000 stars are drawn from a Bahcall-Wolf distribution ($\alpha = 1.75$). This initial condition does not adequately sample stars close to the SMBH. However, this simulation provides a check on mass functions from the other two simulations, which over represent stars close to the SMBH in population demographics because most of the stars in the nuclear star cluster are located further from the SMBH. Each subplot shows the mass function expected at a specific age for the population based on a Kroupa IMF in grey. The red dashed line shows the mass function at a given time for the entire cluster. The blue dash-dotted and green dashed lines show the mass distributions for the stars internal to 0.1 and 0.01 pc, respectively. We do not show the latter for the middle simulation because stars within this region are not adequately sampled for any meaningful result. While Figure 5.4 shows snapshots at only four different times,

the expanded Figures 5.12 and 5.13 in the Appendix display the full evolution of the mass function.

As shown in Figure 5.4, the Rauch99 model, which favors mergers with minimal mass loss, leads to an excess of more massive stars in the inner 0.1 pc (see bottom two rows of the left and middle columns). The Lai+93 column exhibits a similar effect, though to a lesser degree. These stars may appear rejuvenated and younger, especially compared to the surrounding cluster. Interestingly, the IMF of the young stars within $\sim$ 0.5 pc of the SMBH has been suggested to be top heavy, with an excess of massive stars (e.g., Paumard et al., 2006; Bartko et al., 2010; Lu et al., 2009, 2013). Furthermore, the origins of young massive stars in the nuclear star cluster remain an open question; it remains uncertain whether they could have formed in situ in the extreme gravitational potential of the SMBH (e.g., Morris, 1993; Jackson et al., 1993; Gerhard, 2001; Ghez et al., 2003; Genzel et al., 2003; Levin & Beloborodov, 2003; Christopher et al., 2005; Davies & King, 2005; Paumard et al., 2006; Montero-Castaño et al., 2009, see Genzel et al. (2010) section 6 and Alexander (2005) section 7 for a review). It has been suggested that stellar collisions and mergers may instead create these massive stars, explaining the so-called "paradox of youth" of the S-star cluster (e.g., Ghez et al., 2003; Genzel et al., 2003; Antonini et al., 2010; Stephan et al., 2016, 2019). Our findings are consistent with a collisional formation scenario.

5.6 Dust-Enshrouded G Objects

Given the abundance of collisions within 0.1 pc, here we consider what the merger products might look like post-collision, before the stellar object, a newly merged star, has had time to recollapse over a Kelven-Helmholtz timescale. In particular, these merged stars may have connections to gas and dust-enshrouded stellar objects, or G objects, observed in the GC (see Ciurlo et al., 2020). Several works in the literature have addressed the mysterious origin of the G object population (e.g., Murray-Clay & Loeb, 2012; Schartmann et al., 2012;

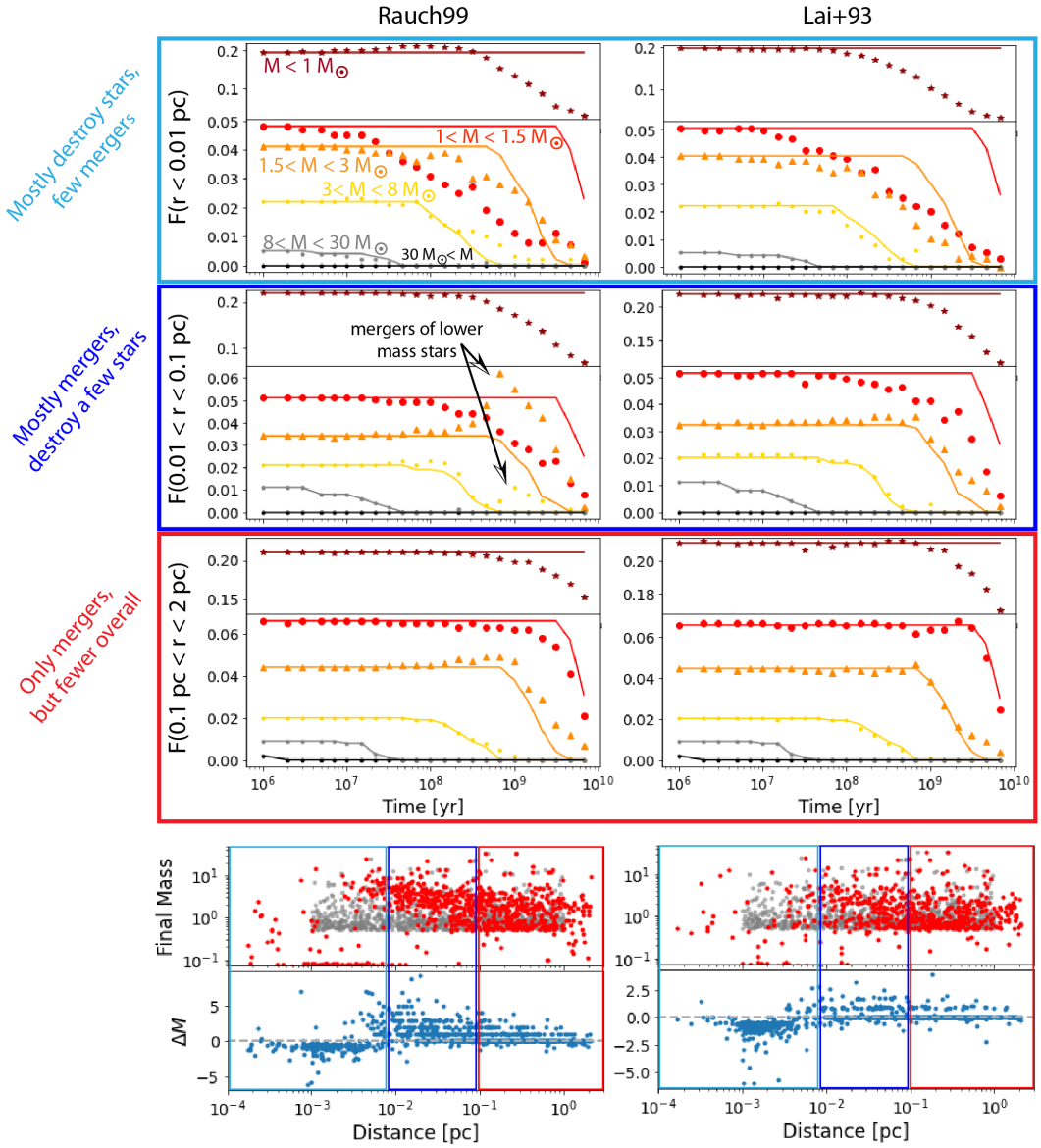

Figure 5.5: This figure juxtaposes the results for two different simulations, one that uses the equations from Rauch99 and the other, Lai+93. These simulations include relaxation, and the initial stellar masses are drawn from a Kroupa IMF. We assume a Bahcall-Wolf density profile for the surrounding stars. The first row shows the fraction of stars in each mass range as a function of time for the population within 0.01 pc of the SMBH. The solid lines represent the expectation in the absence of collisions and relaxation. In other words, the solid lines decrease when stars within each mass range reach the end of their main-sequence lifetimes. The symbols show the simulated results. For example, as can be seen from the positions of the symbols relative to the curves, collisions destroy stars between 1 and 3 $M_\odot$ before they can evolve off the main-sequence. The second and third rows in the figure do the same for 0.01-0.1 pc and 0.1-2 pc from the SMBH. The last row shows the final masses and semimajor axes of the stars in red compared to the initial conditions, in grey, and the change in mass for the stars in blue. For a shallower profile ($\alpha = 1.25$), see Figure 5.15 in Appendix 5.9.4.

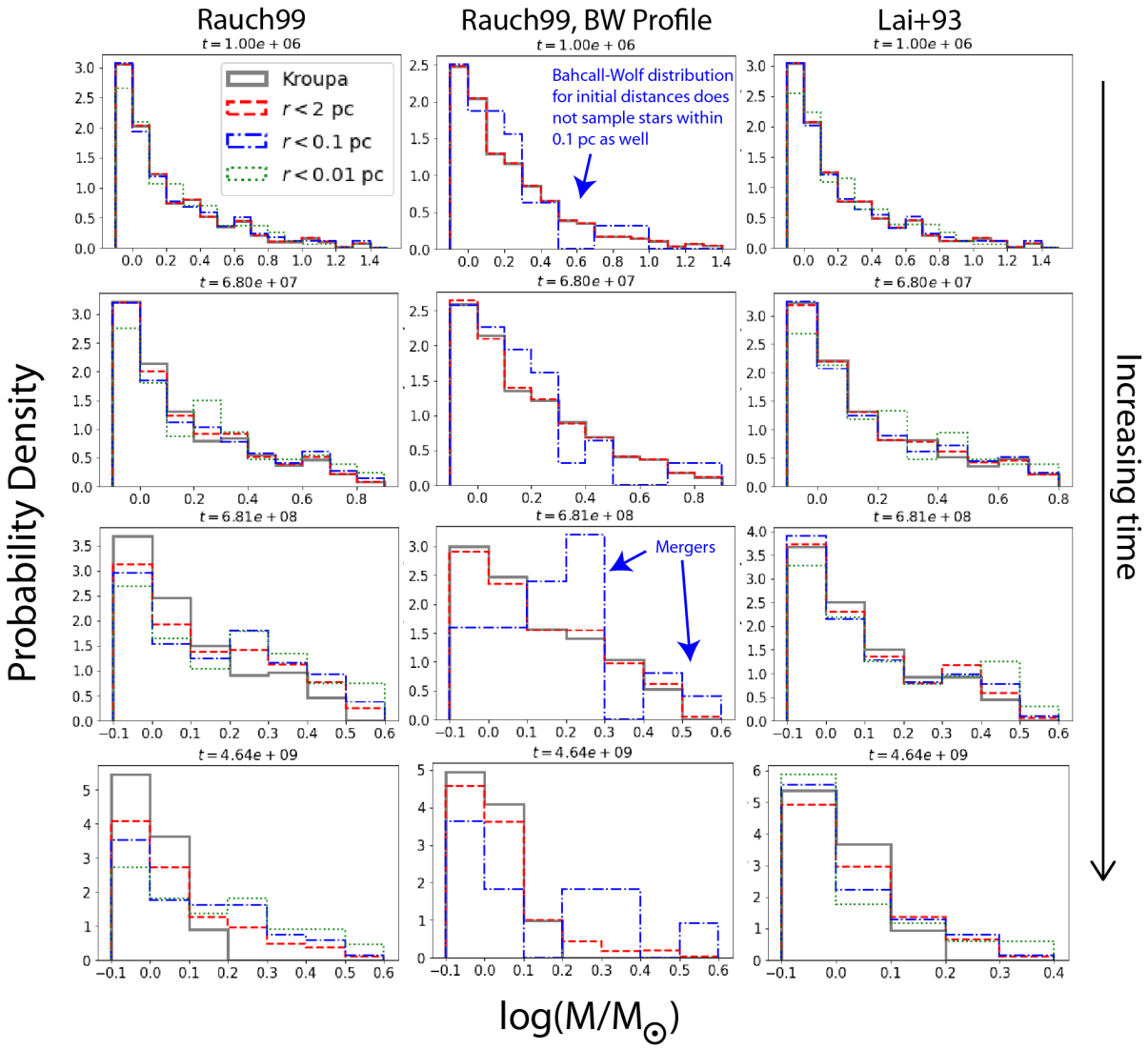

Figure 5.6: This figure shows the simulated stellar population's distribution of masses at a given time, noted in years at the top of each subplot. Each column corresponds to a different simulation, ordered chronologically from top to bottom. The right and left columns are from the same simulations shown in Figure 5.5. The middle column shows the results of a simulation identical to the one on the left except the stars are sampled from a Bahcall-Wolf distribution; they are not distributed uniformly in log distance. The grey histograms show the expected surviving stars from a population that started with a Kroupa IMF. The red dashed, blue dash-dotted, and green dotted histograms correspond to the stars internal to 2, 0.1, and 0.01 pc respectively.

Burkert et al., 2012; Zajaček et al., 2017; Madigan et al., 2017; Owen & Lin, 2023). For example, stellar mergers from binary systems may explain the presence of these distended stellar objects (e.g., Witzel et al., 2014; Prodan et al., 2015; Stephan et al., 2016, 2019). In the nuclear star cluster, gravitational perturbations from the SMBH on a stellar binary's orbit can drive the binary to merge (e.g., Antonini & Perets, 2012; Prodan et al., 2015; Stephan et al., 2016, 2019). Collisions between other species like compact objects and RGs have also been invoked to explain the formation of G objects (Mastrobuono-Battisti et al., 2021).

We estimate the number of G objects from main-sequence stellar collisions in the GC in Figure 5.7. We begin by calculating the number of collisions that occur per year at each distance from the SMBH. A post-collision merger product remains puffy and extended for a thermal timescale (see Stephan et al., 2016, 2019).[3] Therefore, the number of G-type objects visible at a given distance from the SMBH is equal to the collision rate times 10^7 yr, plotted in the second row of the Figure. The last row shows the cumulative number of G objects as a function of distance from the SMBH for three different stellar density profiles, $\alpha = 1.25$, 1.5, and 1.75. This analytic calculation assumes a uniform population of solar mass stars. We do not include collisions internal to about 0.008 pc, based on Figures 5.4 and 5.5, because collisions in this region are largely destructive and do not result in mergers. For the least cuspy of the profiles considered, $\alpha = 1.25$, we expect approximately 10 G objects, a number consistent with the current G object populations (Ciurlo et al., 2020). For the other two steeper density profiles, $\alpha = 1.5$ and 1.75, G objects should number in the tens and hundreds, respectively. The density profile in the Galactic Center in present day appears to be shallower than a Bahcall-Wolf profile, lying between about $\alpha = 1.25$ and 1.5 (e.g., Genzel et al., 2003; Gallego-Cano et al., 2018).

[3]The time it takes for two merging stars to appear as a single, non-distended object is uncertain and may be shorter than the thermal timescale, 10^7 yr (e.g., COSMIC package from Breivik et al., 2020; Ivanova, 2011; Ivanova et al., 2013). However, a more detailed analysis is beyond the scope of this paper.

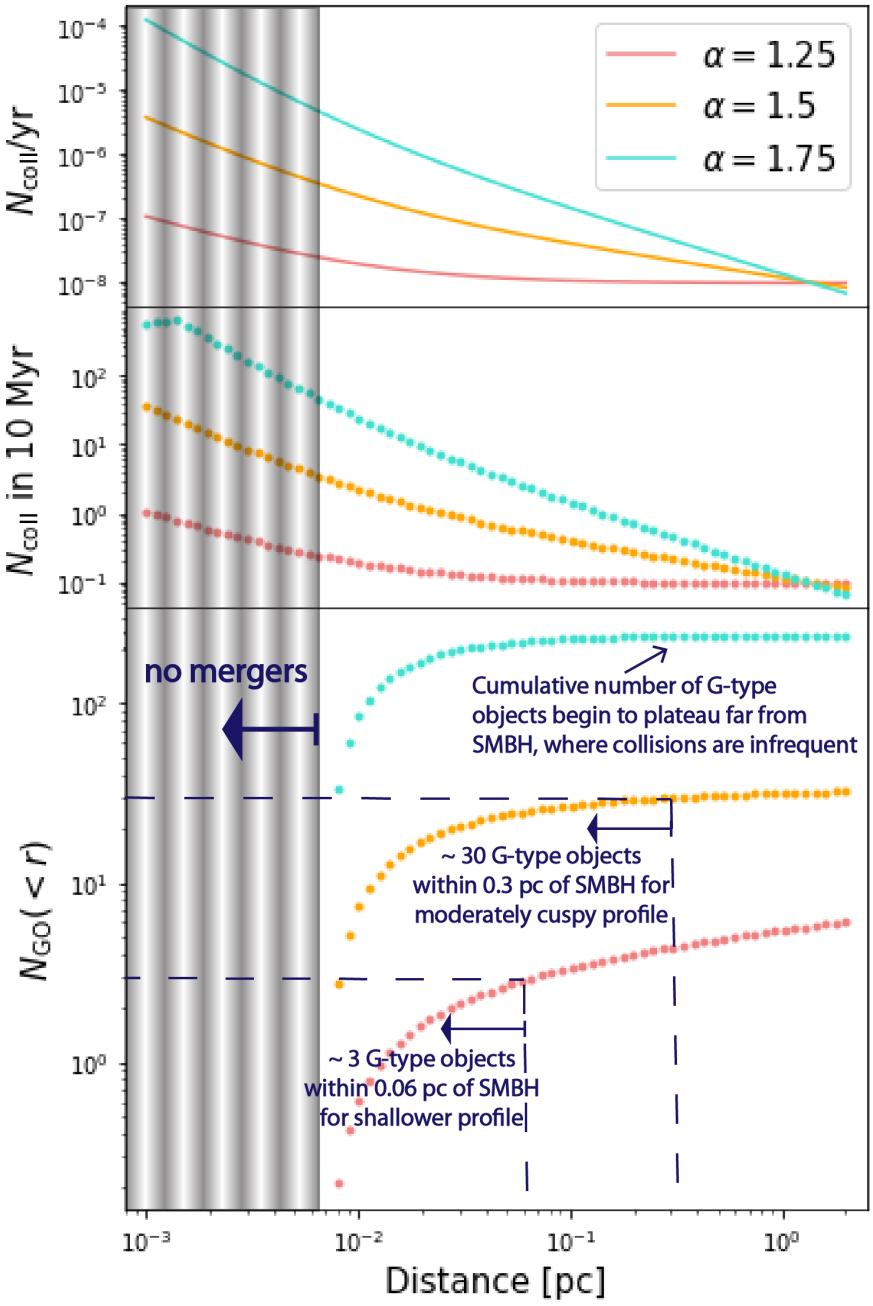

Figure 5.7: Here we provide predictions for the number of G-type objects in the nuclear star cluster formed through main-sequence stellar collisions. The uppermost panel shows the total number of stellar collisions per year as a function of distance from the SMBH for different density profiles. The second row shows the total number of collisions at each distance that occurs within 10 Myr, the approximate thermal or Kelvin-Helmholtz timescale of a Sun-like star. The last row shows the cumulative number of G-type objects within a given distance from the SMBH. An annotation is provided on the Figure to demonstrate how to interpret these curves.

5.7 Implications for the Red Giant Population

Observations of the nuclear star cluster indicate that the surface number density of RGs plateaus within about 0.3 pc of the SMBH (e.g., Genzel et al., 1996; Buchholz et al., 2009; Do et al., 2009; Gallego-Cano et al., 2018; Baumgardt et al., 2018; Habibi et al., 2019). This plateau diverges from the cusp-like density profile expected for an older, evolved stellar population (e.g., Bahcall & Wolf, 1976; Linial & Sari, 2022, see the latter for the distribution expected from steady-state scatterings). The observed missing RG cusp has motivated several proposed mechanisms to destroy RGs near the SMBH, many of which have been unable to completely explain the phenomenon (Davies et al., 1998; Alexander, 1999; Bailey & Davies, 1999; Dale et al., 2009; Zajaček et al., 2020). Of the proposed mechanisms, the most promising relies on interactions between the RGs and a gaseous disk in the GC, which strip the RGs of their outer layers (Amaro-Seoane & Chen, 2014; Amaro-Seoane et al., 2020), though we also note that the missing cusp may have a dynamical explanation, without requiring the destruction of the individual RGs (e.g., Merritt, 2010; Antonini, 2014). Here, we explore the possibility that main-sequence stellar collisions contribute to the dearth of RGs. As shown in Figure 5.1, 1-3 $M_\odot$ stars within ~ 0.1 pc of the SMBH are likely to experience a collision before evolving off the main-sequence. To ensure a deficit in RGs, these stars must lose significant mass – or be completely destroyed – before they can evolve off the main-sequence, or mergers may accelerate their evolution off the main-sequence.

Recently, Mastrobuono-Battisti et al. (2021) undertook a comprehensive N-body study of collisions between many different species in the GC and comment on a variety of applications, including the missing RGs. Their results suggest that collisions between main-sequence stars cannot explain the underabundance of RGs in the GC. They assume that the stars merge with no mass loss when the velocity dispersion is between 100 and 300 km/s, as is the case in their model. However, a velocity dispersion of 300 km/s corresponds to a distance of about 0.07 pc from the SMBH. Furthermore, a 1 $M_\odot$ star may diffuse into regions of

larger velocity dispersion over its main-sequence lifetime, which is longer than the ~ 1 Gyr relaxation timescale. In this section, motivated by Figures 5.5 and 5.6, we assess whether collisions closer to the SMBH can affect the RG count in the GC.

We generate RG surface density profiles at different snapshots in time from our fiducial Rauch99 simulation, shown for example in the left column of Figure 5.5. For adequate resolution, we increase the number of stars in our sample from 1000 to 4000. Only a subset of this population will be RGs at any given time. The RGs used to generate the surface density profiles shown in Figure 5.8 number at about 100 each. We bin the number of RGs by distance from the SMBH. We then take the number of RGs formed per star and scale it by the number of stars expected at that distance, normalized using the M-σ relation (Tremaine et al., 2002). Figure 5.8 shows the results at three different ages for the stellar population, 3, 4, and 8 Gyr in grey, peach, and red, respectively. We compare these results to data from figure 9 of Gallego-Cano et al. (2018), represented by the blue star-shaped dots. Extinction may explain the dip in the RG count data at 0.2 pc (Buchholz et al., 2009; Gallego-Cano et al., 2018). We have scaled our simulated results to coincide roughly with the number of observed RGs at 1 pc. In each panel, we also include a Bahcall-Wolf profile to guide the eye.

Both our simulated results and the observed profile lack a cusp internal to about 0.1 pc. In this region, mergers occur. As a result, these stars evolve off the main-sequence more rapidly. This process can boost the number of RGs at earlier times. The timing at which these stars evolve off the main-sequence has a radial dependence, based on the collision timescale. A population over a few Gyr old may have already experienced this accelerated boost of RGs, leading to a deficit in present time. Additionally, in this region, where multiple collisions are possible, many stars may undergo enough mergers to exceed 3 $M_\odot$ (see also the last panel of Figure 5.4). Lastly, more massive stars spend less time as RGs, so merging 1 $M_\odot$ stars into 2 $M_\odot$ stars, for example, reduces the chances of catching and observing them as RGs.

The discussion above pertains to stars outside ~ 0.01 pc, the innermost distance from the

SMBH included in Figure 5.8. However, as seen in Figure 5.5, stellar collisions destroy most low-mass ($\lesssim$ 3 $M_\odot$) stars within $\sim$ 0.01 pc of the SMBH before they can evolve off the main-sequence. Thus, we also expect a clear RG deficit in this region. We note that it remains uncertain whether stellar collisions, even at extremely high velocities, can destroy stellar cores. The first one or few collisions in this $\lesssim$ 0.01 pc region can easily remove that outer layers of a star. In our simulations, later collisions can go on to destroy the low-mass collision remnants. However, if these stellar cores prove more resilient against collisions, our results may need to be revisited.

We stress that the simulated curves in Figure 5.8 should not be used as predictions for the number of RGs at a given distance from the SMBH. This exercise is meant to draw attention to the general shape of the RG surface density profile based on our results. The actual RG density is likely a composite of several of these theoretical curves. The GC contains populations of different ages and its star formation history remains an open area of research (e.g., Pfuhl et al., 2011; Schödel et al., 2020; Nogueras-Lara et al., 2021; Chen et al., 2023). Additionally, our simulations consider an evolving sample of stars embedded in a fixed, unchanging cluster. In an actual stellar cluster, a merger between two stars results in a single object. Each collision should therefore reduce the number of particles in the system. In our simulations, however, the number of particles, or stars, remains the constant in our sample. Our final numbers may therefore over count by a factor of two. Lastly, in addition to the caveats mentioned above, we also assume an initial Bahcall-Wolf profile ($\alpha = 1.75$) for the stars. Two-body scattering in the presence of a black hole population in the nuclear star cluster may instead cause the stars to settle on a slightly shallower ($\alpha = 1.5$) profile within a critical radius from the SMBH (Linial & Sari, 2022). A shallower initial profile leads to a longer collision timescale, lessening the impact of this dynamical process on the density profile within 0.1 pc (Rose & MacLeod, in prep.).

We also note that the number of RGs depends on the interplay between distance from

the SMBH and time. The profile's shape is determined by when mergers occur at a given distance from the SMBH and how many mergers are possible before the star evolves off the main sequence; It is sensitive to both the destruction and formation of RG progenitors via collisions. For example, in Figure 5.5, mergers produce an abundance of RG progenitors at about 1 Gyr. Figure 5.9 presents two examples of RG profiles that lack an apparent plateau within 0.1 pc. In conjunction, Figures 5.8 and 5.9 show that collisions can produce both cuspy and core-like RG density profiles depending on the age of the population. Interestingly, the density profiles in the latter figure still lack RGs within $\sim$ 0.03 pc. We speculate that this dearth occurs for two reasons: collisions begin to become destructive for the lowest mass stars in this region, while stars that are not destroyed instead experience multiple mergers. In other words, RG progenitors are not being replenished at the rate they are being eliminated.

Gallego-Cano et al. (2018) and Schödel et al. (2018) find that only the brightest giants exhibit a flattening of their profile within $\sim$ 0.1 pc, while observations of the less bright main-sequence stars and subgiants are consistent with a cusp. Schödel et al. (2018) note that the type of stars being observed and the degree of contamination from young, unrelaxed stellar populations are uncertain, especially as they rely on diffuse light to probe the stellar profile. However, their results imply that the mechanism destroying the RGs must act after the stars have ascended the giant branch. The mechanism we discuss here, main-sequence stellar collisions, would deplete the RG progenitors before they evolve off the main-sequence. Our results do not necessarily contradict the observations for the reasons discussed above: the RG density profile depends on the age of the parent population(s) and the initial density profile assumed for the stars. We reserve a more thorough examination of the surface density profile for future work. However, our results suggest that main-sequence stellar collisions merit further consideration in the context of the evolved population.

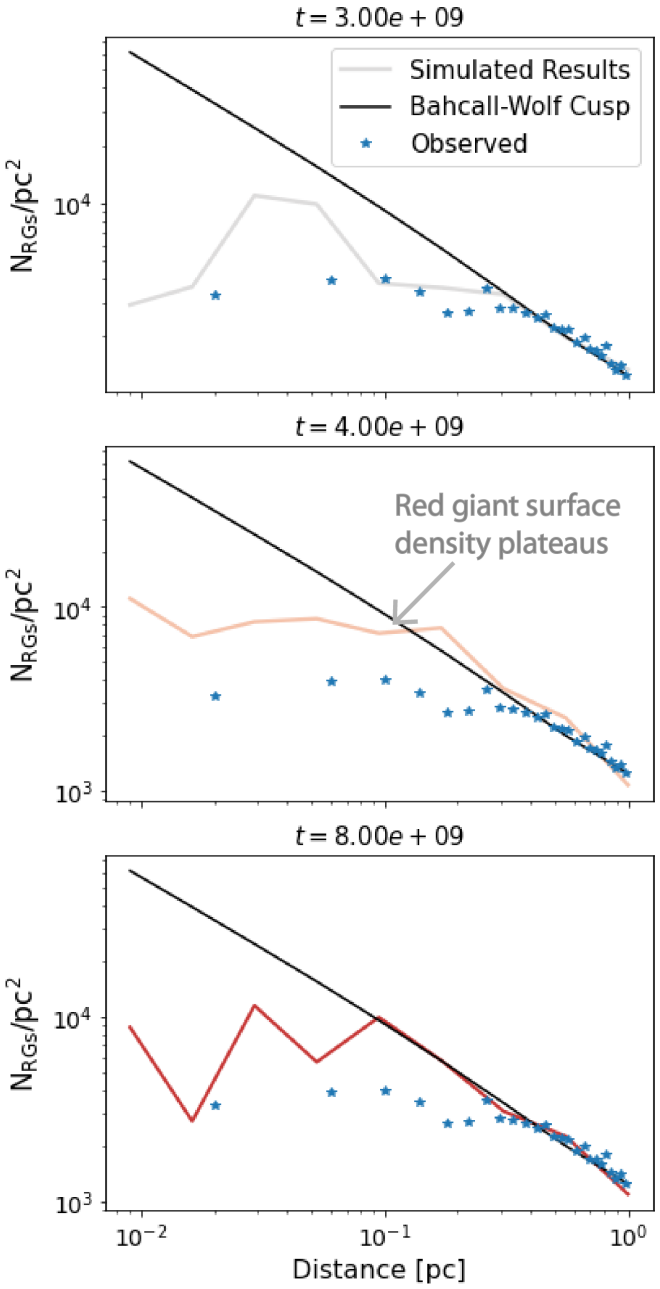

Figure 5.8: We generate surface density profiles for the RGs from our fiducial Rauch99 simulation, depicted in the left column of Figure 5.5, for example. This figure shows examples of the simulated RG surface density at three different times: 3 Gyr in grey in the top panel, 4 Gyr in peach in the second panel, and 8 Gyr in red in the bottom panel. The black line depicts a Bahcall-Wolf profile, the theoretical prediction for an old population (Bahcall & Wolf, 1976). The blue stars show the observed RG surface density from Gallego-Cano et al. (2018) figure 9. We scale our simulated profiles to roughly match the observed number of RGs at 1 pc. The simulated RG surface densities, similar to the data, plateau within ~ 1 pc from the SMBH, diverging from the predicted cusp.

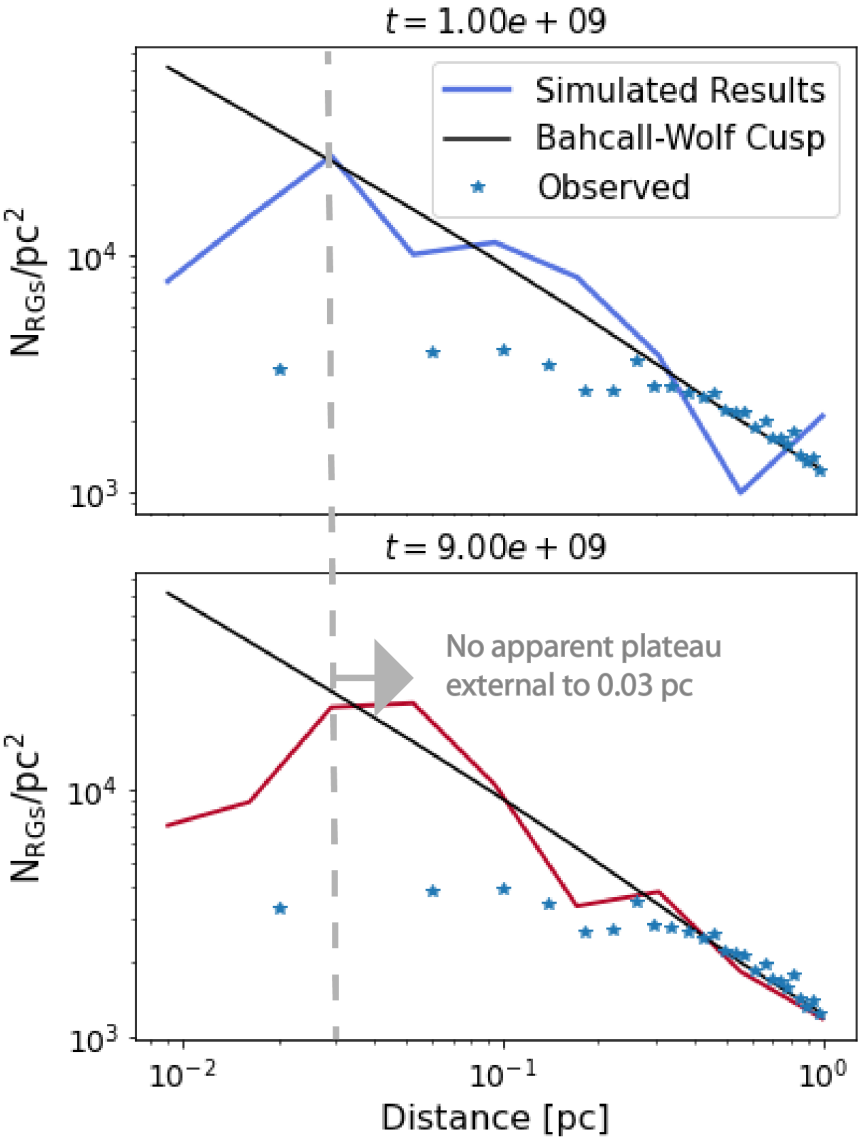

Figure 5.9: Here we show two additional RG surface density profiles, at 1 and 9 Gyr, from our fiducial Rauch99 simulation. The black line shows an $\alpha = 1.75$ profile to guide the eye (Bahcall & Wolf, 1976), while blue stars show the observed bright RGs from Gallego-Cano et al. (2018) figure 9. We again scale our simulated profiles to roughly match the observed number of RGs at 1 pc. Unlike Figure 5.8, these density profiles do not show any plateau at 0.1 pc. Rather, there is only a clear plateau within about 0.03 pc.

5.8 Summary

Collisions that take place in the dense nuclear star cluster surrounding our galaxy's central SMBH can shape the stellar population. Within about 0.1 pc, every star undergoes at least one collision during its lifetime. More generally, within the inner 1 pc, we estimate that 10% of the stellar population will experience at least one collision while on the main-sequence. In this study, we characterize the outcomes of these collisions as a function of distance from the SMBH. In particular, we consider three regimes: (1) within $\sim$ 0.01 pc of the SMBH, where the velocity dispersion is large and collisions are destructive, (2) 0.01-0.1 pc, where collisions are common and result in stellar mergers, and (3) outside of $\sim$ 0.1 pc, where collisions do not occur very frequently, but always result in mergers. The details of each collision, specifically the amount of mass ejected during the collision, are more difficult to determine. In particular, the mass lost from the stars depends on their relative velocity, mass ratio, structure, and impact parameter (e.g., Lai et al., 1993; Freitag & Benz, 2002). We adopt different prescriptions to treat the mass loss, including a few based on fitting formulae from SPH studies (Lai et al., 1993; Rauch, 1999). Our models also account for two-body relaxation, which works to change the semimajor axes and eccentricities of the stellar orbits in the GC over time. We find the following:

(i) *The Formation of Massive Stars:* The mass loss prescriptions all lead to qualitatively similar results, consistent with our expectations for the different regimes. In particular, in the 0.01-0.1 pc regime, stars with mass greater than ~ 8 $M_\odot$ can form from mergers between 1 $M_\odot$ stars. Furthermore, in the case that collisions result in only moderate mass loss even at high impact velocities, as is the case for the Rauch99 equations, repeated collisions between low-mass can consistently form massive ($\gtrsim 10$ $M_\odot$) stars. These massive products are mainly localized within the $\sim$ 0.01-0.1 pc region, as there is insufficient time for them to diffuse to distances $\sim$ 1 pc from the SMBH. However, as can be seen in Figures 5.4 and 5.5, significant mass growth through mergers remains possible, albeit less probable, at $\lesssim$ 1 pc from the

SMBH. We predict that there should be at least 100 massive stars formed from lower mass stars in this region. Generally, mergers may cause the mass function of the population to appear top-heavy (see Figure 5.6, in keeping with observations of this region (e.g., Paumard et al., 2006; Bartko et al., 2010; Lu et al., 2009, 2013).

(ii) *A Diffuse Population of Low Mass Remnants:* Collisions can divest many main-sequence stars of their outer layers, creating a low-mass stellar object. This result is consistent with previous studies (Rauch, 1999). These collision remnants can migrate through relaxation processes from their place of formation, $\lesssim 0.01$ pc, to greater distances from the SMBH. We therefore predict a population of low-mass peculiar stars throughout the GC. Additionally, the mass ejected through grazing or off-axis collisions may produce gas and dust features in the Galactic Center, like the observed X7 (e.g., Ciurlo et al., 2023), whose distance from the SMBH is comparable to where σ becomes $\lesssim v_{esc}$ (see Figure 5.1).

(iii) *The Survival of Low-Mass Stars within* 0.01 *pc:* While collisions within 0.01 pc tend to be very destructive for the stars, our results suggest that their populations may persist for longer than expected based on the collision timescale alone, similar to findings in other studies (e.g., Rauch, 1999). In fact, it takes ~ 1 Gyr to halve the populations of low-mass ($\lesssim 3$ $M_\odot$) stars. This timescale is the same order of magnitude as the relaxation timescale in this region (Figure 5.1). Episodes of star formation, not included in this study, may therefore help replenish the stellar population in this region. Depending on the age of the population, there may be an undetected population of low-mass stars and collision remnants in the innermost region of the nuclear star cluster.

(iv) *G Objects:* Collisions between main-sequence stars may have connections to the G objects, stellar objects enshrouded in gas and dust observed in the GC (e.g., Ciurlo et al., 2020). A merger between two collided stars may produce a puffy G-like object that recollapses over the thermal timescale of a solar mass star, 10^7 yr (similarly, for binary mergers, see e.g., Stephan et al., 2019). We provide predictions for the number of G type objects expected

in the GC from stellar collisions given different stellar density profiles. For a stellar density profile with index α between 1.25 and 1.5, there may be $\sim$ 10 G objects observable in the inner parsec of the GC.

(v) *Connections to the Missing Red Giants:* Observations of the GC indicate a deficit of RGs within about $\sim$ 0.3 pc of the SMBH (e.g., Genzel et al., 1996; Buchholz et al., 2009; Do et al., 2009; Gallego-Cano et al., 2018; Habibi et al., 2019). We consider whether main-sequence stellar collisions may help explain this observational puzzle. We find that within $\sim$ 0.01 pc of the SMBH, stellar collisions destroy most low-mass stars before they can evolve off the main-sequence (see Figure 5.5). Thus, we expect a lack of RGs in this region. Further from the SMBH, between $\sim$ 0.01-0.1 pc, mergers can result in fewer RGs. As seen in Figure 5.8, the RG surface density profile plateaus in this region, an effect similar to what is observed in the GC. Both the profiles from our models and observations diverge from the density cusp expected for an old, dynamically relaxed population: $\alpha = 1.75$ in Eq. 5.1.

Collisions play a crucial role in shaping the stellar populations in the inner parsec of the GC. We show that this dynamical channel leads to a number of interesting observables, including rejuvenated, massive stars near the SMBH, G objects, and missing evolved stars. Our simulations focus on the dynamics of this dense environment using a statistical approach. We leverage previous SPH studies (e.g., Lai et al., 1993) and intuitive toy models. However, our results highlight the need for future work to explore the rich interplay between hydrodynamics, stellar evolution, and collisions in these dense, dynamic environments.

Acknowledgments

We thank Anna Ciurlo, Cheyanne Shariat, Jessica Lu, Mark Morris, Morgan MacLeod, Ylva Gotberg, and Enrico Ramirez-Ruiz for helpful discussion. SR thanks the Charles E. Young Fellowship, the Dissertation Year Fellowship, and the Thacher Fellowship for support. SR,

SN, and RS acknowledge the partial support of the NSF-AST 2206428 grant. SR and SN acknowledge the partial support from NASA ATP 80NSSC20K0505. SN thanks Howard and Astrid Preston for their generous support.

5.9 Appendix

5.9.1 The Structure of Our Sun: Basis for the Toy Core + Envelope Model

We base our toy "core + envelope" model on the structure of the Sun as described in Christensen-Dalsgaard et al. (1996).[4] The lower panel of Figure 5.10 shows the mass enclosed within a given radius. Based on the mass enclosed within a given radius r, we calculate the escape velocity from a sphere with equivalent mass and radius, $v_{\rm esc} = \sqrt{2GM_{\rm enc}/r}$. Note that this quantity is not the true escape velocity from some point r within the Sun as that would require integrating from r to infinity to account for the outer layers. We plot this quantity as a function of distance from the center of the Sun all the way to the surface in the upper panel of Figure 5.10. Because most of the Sun's mass is concentrated at its center, this quantity peaks at 0.33 $R_\odot$, a radius which encloses 66% of the Sun's mass. We define the "core" of the star such that its radius coincides with this point. The "envelope" comprises the material external to this point, which is more loosely bound. Assuming that all stars have a similar structure, we scale this model to all star's within our considered mass range; we take 66% of the star's mass to be within $0.33 \times R_{\rm star}$ of the star's center and define this region as the "core". We then calculate collision outcomes as detailed in Section 5.2.3.3. This approach gives a straightforward, intuitive way of calculating the fractional mass loss and determining the outcome of a collision.

[4] https://users-phys.au.dk/~jcd/solar_models/cptrho.l5bi.d.15c

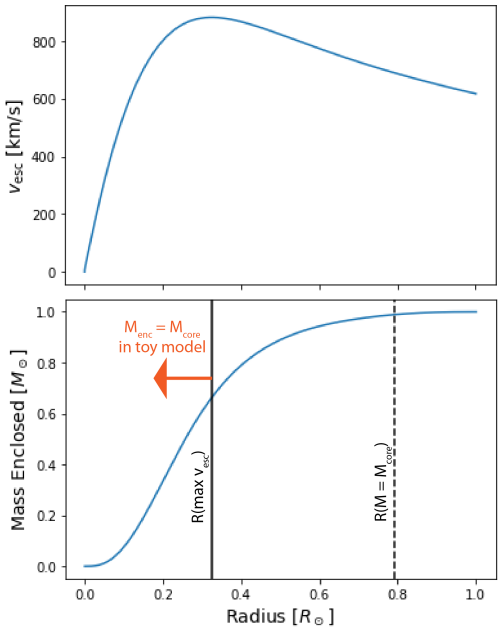

Figure 5.10: We base our toy "core" and "envelope" model on the structure of the Sun and generalize it to all stars. Above we show the escape speed as a function of radius within the star in the upper panel. It peaks around 0.33 $R_\odot$ because most of the mass is concentrated at the center, as can be seen in the lower panel which plots mass enclosed versus radius. We define this radius as the extent of the "core" in our toy model, containing about 66% of the mass. We mark this radius with a solid black vertical line. Additionally, we show the radius of a 0.66 $M_\odot$ main-sequence star, which will be the new radius of a solar mass star if it is completely divested of its "envelope" in a collision.

5.9.2 Dependence on the Eccentricity Distribution

In this Appendix, we relax the assumption that the orbital eccentricities of the stars are on a thermal distribution, in which the probability density $f(e)$ is proportional to e. We test two other initial eccentricity distributions. Firstly, we test a uniform initial distribution, in which all eccentricities are equally likely. The average eccentricity for this population is 0.5, as opposed to ~ 0.67 for a thermal distribution. We also test a distribution with the form $f(e) \propto e^{0.5}$, which favors low eccentricities. The results of these simulations are shown in Figure 5.11. For ease of comparison to Figure 5.3, they do not include relaxation. Other than the eccentricity distribution, the initial conditions are identical to the simulation shown in the las row of Figure 5.3.

The first and second rows of Figure 5.11 show simulations that use $f(e) \propto e^{0.5}$ and a uniform eccentricity distribution, respectively. The results are qualitatively similar to Figure 5.3. While the less eccentric initial conditions result in fewer massive stars, their formation is still likely. This result is expected based on Rose et al. (2020), who find that the collision timescale of a very eccentric orbit ($e > 0.95$) and a circular orbit differ by a factor of two.

5.9.3 Expanded Stellar Mass Function History Plots

In this section of the Appendix, we show expanded versions of Figure 5.6, including more time steps to detail the evolution. Figure 5.12 shows stellar mass distributions before a Gyr. Figure 5.13 shows snapshots from a Gyr onward. Together, they provide a more detailed evolution of the mass function. Mergers skew the mass function toward higher masses, giving it a slightly top-heavy appearance.

5.9.4 Other Stellar Density Profiles

Our simulations assume a background population of stars with some density profile that remains fixed. However, ovetime, we expect stellar collisions to modify the distribution, in

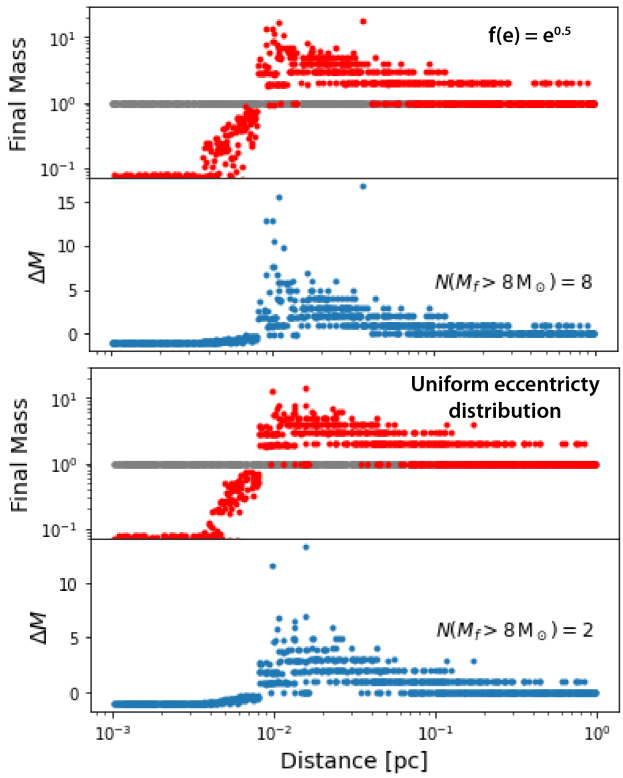

Figure 5.11: Here we show a figure in the style of Figure 5.3. We use the Rauch99 collision prescription for a direct comparison to the last subplot of Figure 5.3, which as mentioned above uses a thermal eccentricity distribution, the only difference between that simulation and those shown in this Appendix.

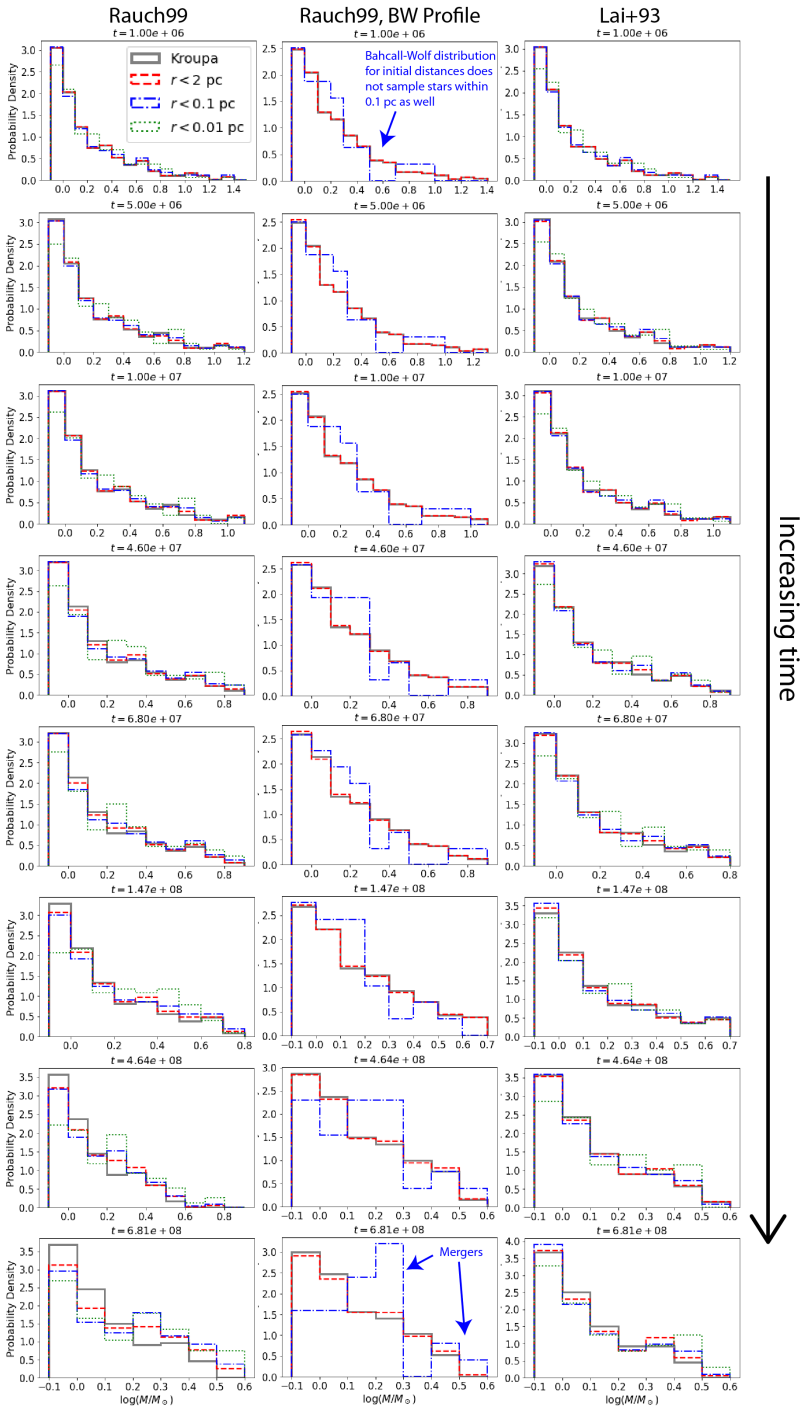

Figure 5.12: This Figure shows an expanded version of Figure 5.6 up to a Gyr. Each row corresponds to a snapshot in time, noted in years at the top of each plot. The left and right columns correspond to our Rauch99 and Lai+93 simulations, respectively. The middle panel shows results from a Rauch99 simulation that samples stars from a Bahcall-Wolf distribution ($\alpha = 1.75$).

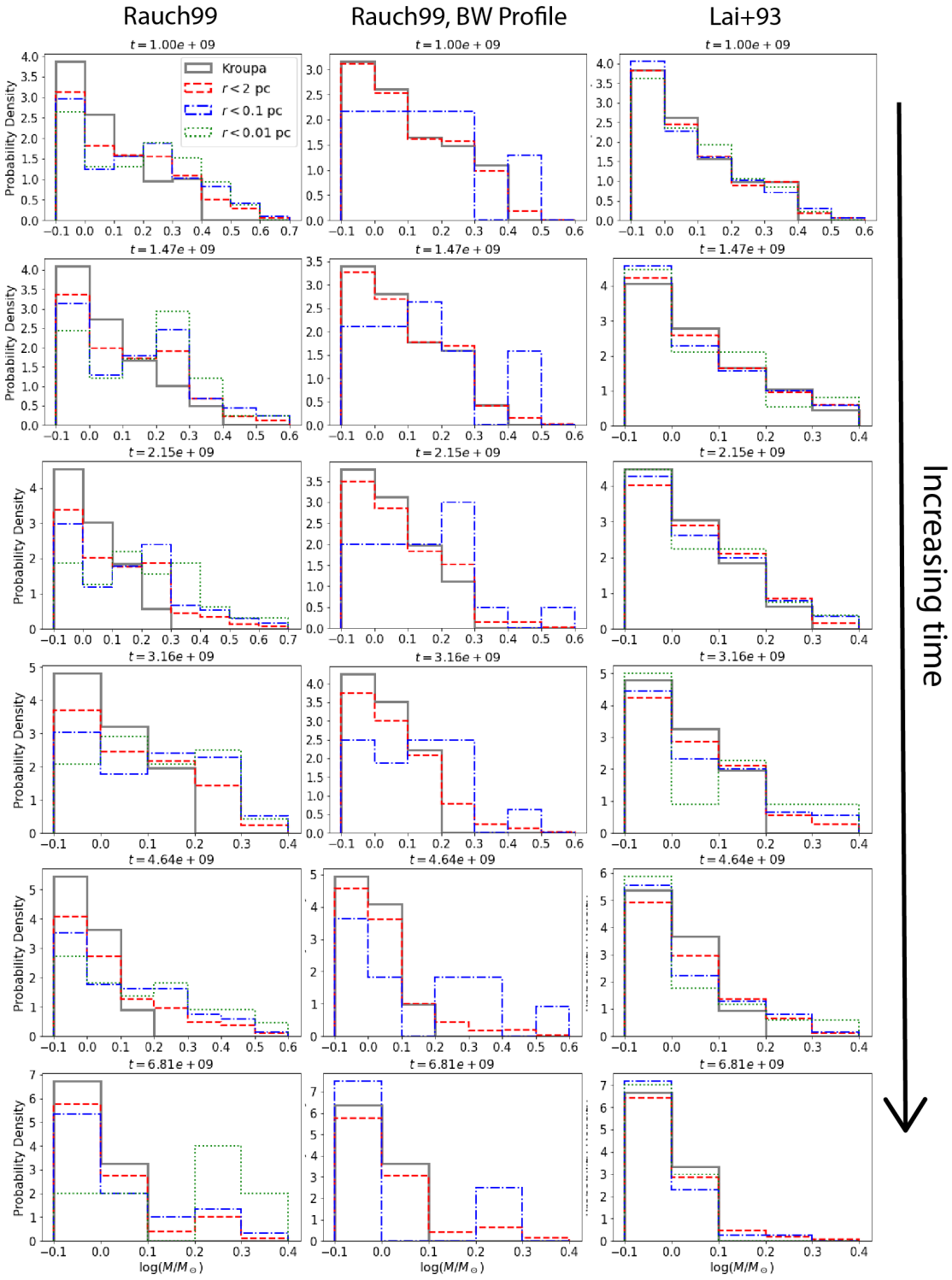

Figure 5.13: Showing stellar mass distributions from a Gyr onward, this figure is a continuation of Figure 5.12.

particular by eroding the cusp near the SMBH. In the absence of star formation, the new, shallower density profile can only lead to a lower collision rate. As a result, our predictions of the rate of destruction of stars may be overpredicting their decline in population. Additionally, two-body scattering with a population of heavier black holes may cause the stars to lie on a profile with index $\alpha = 1.25$ (Linial & Sari, 2022), and observations of the GC's nuclear star cluster suggest that the profile may be shallower (e.g., Genzel et al., 2003; Gallego-Cano et al., 2018). Therefore, we are including a version of the Rauch99 simulation with an $\alpha = 1.25$ density profile for the surrounding star cluster, as opposed to our default $\alpha = 1.75$. The most realistic picture probably lies between the $\alpha = 1.75$ and $\alpha = 1.25$ cases.

We show results in the same style as Figures 5.3 and 5.5. In Figure 5.14, we plot the results of a Rauch99, $\alpha = 1.25$ that does not include the effects of relaxation. There are fewer mergers due to the shorter collision timescale. The merger products are therefore less massive compared to the $\alpha = 1.75$ case. Additionally, the stars are not destroyed as efficiently. As can be seen in the upper panel of Figure 5.14, the low-mass collision remnants persist for longer closer to the SMBH.

In a similar fashion, Figure 5.15 is identical to the left column of Figure 5.5 except for the assumed density profiles. More massive stars are still formed through collisions, but they are generally limited to less than 3 $M_\odot$ because fewer collisions occur. For the same reason, the decline of the low-mass stars occurs more gradually than in the $\alpha = 1.75$ case.

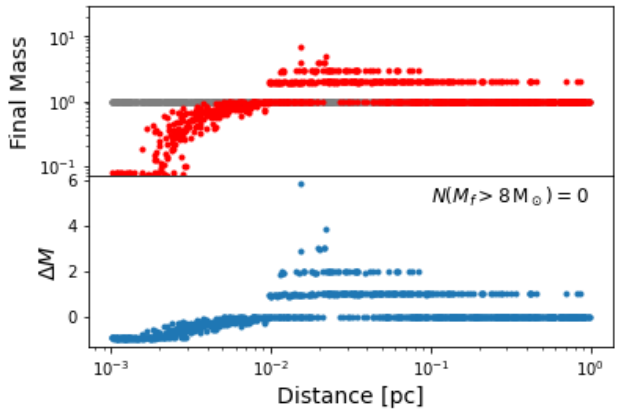

Figure 5.14: This figure shows the results of a Rauch99 simulation with a shallower $\alpha = 1.25$ density profile for the surrounding stars. Other than the density profile, this simulation has identical conditions to the one depicted in the last row of Figure 5.3: a uniform population of solar mass stars and no relaxation processes included. The initial conditions are shown in grey in the top panel, while the red points show the final masses of the stars and the blue points, their total change in mass over the course of the simulation.

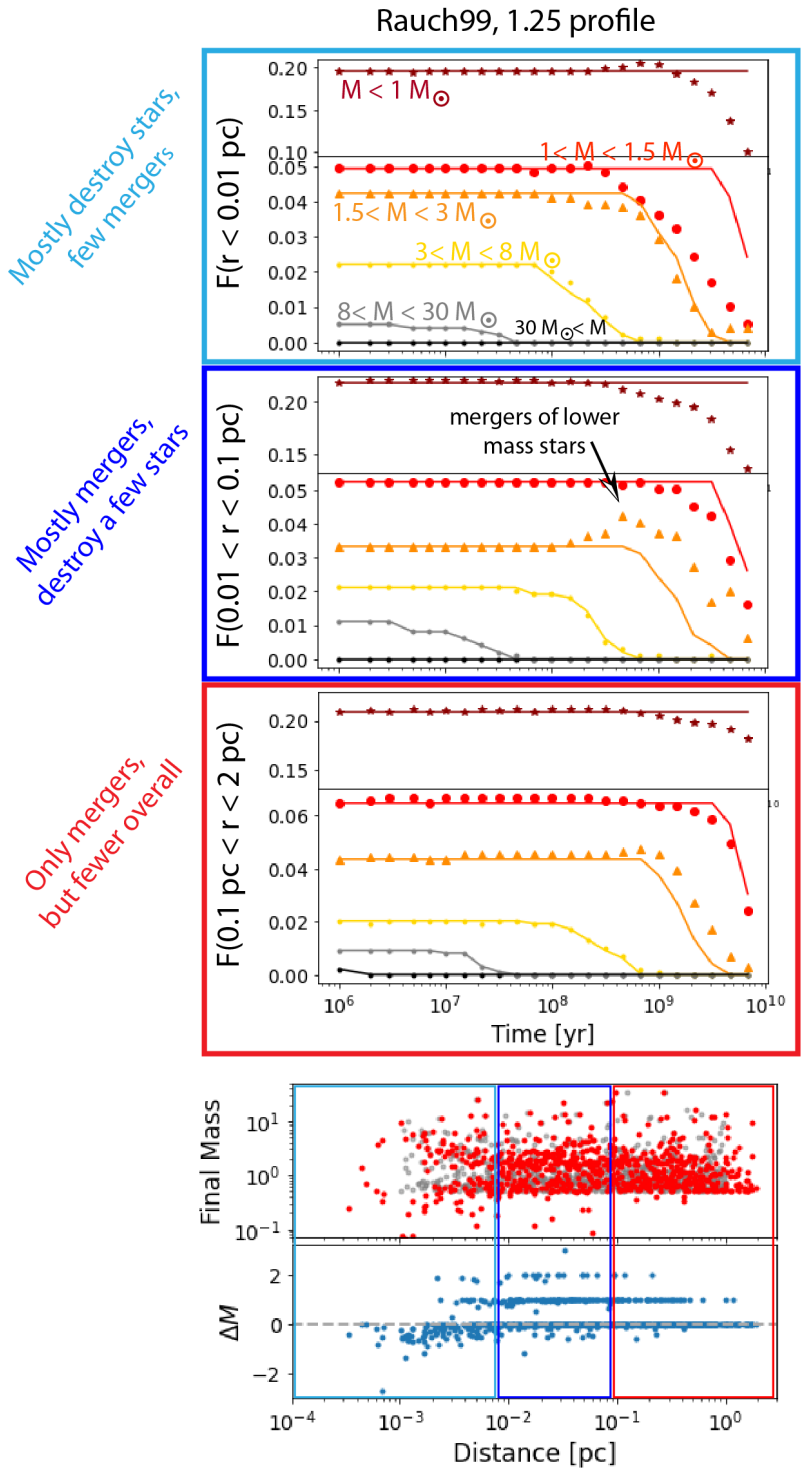

Figure 5.15: This figure has the same format as Figure 5.5. The simulation used is identical to the left column of the aforementioned figure, except it uses a shallower $\alpha = 1.25$ density profile for the surrounding stars.

CHAPTER 6

Conclusion

Almost every galaxy has a 10^{6-9} $M_\odot$ SMBH at its center (e.g., Ferrarese & Ford, 2005), and the closest SMBH to Earth resides at the center of our galaxy (e.g. Ghez et al., 2005). Observations suggest that the binary fraction in the Milky Way's GN is comparable to that of young stellar clusters (e.g., Ott et al., 1999). Furthermore, any binary in the GN is in fact in a triple system, where the third body is the SMBH. In this configuration, coherent gravitational perturbations from the outer body, the SMBH, influence the long-term evolution of the binary. In particular, these perturbations cause the orbital eccentricity and inclination to oscillate in time, a dynamical process known as the EKL Mechanism (e.g., Naoz, 2016).

In Rose et al. (2019), focusing on young stellar clusters, I examine the signatures of triple body dynamics in the inner binary properties. In this study, the tertiary body is another star on a wide orbit instead of a SMBH, however the physics is similar. Many massive stars reside in triples (Raghavan et al., 2010; Moe & Di Stefano, 2017). While the birth orbital configurations of massive binaries remain uncertain, observations have constrained the properties of older populations, in particular their orbital eccentricity and period distributions (e.g., Sana et al., 2012). The objective of Rose et al. (2019) is to determine the manner in which the final property distributions of these systems map back onto their initial conditions. Running 38 sets of Monte-Carlo numerical simulations with 1000 systems each, I tested a range of initial distributions to identify traces of the initial conditions in the simulated final results. I

found that the period distribution for wide orbits is preserved despite 10 Myr of EKL-driven evolution. I also found that the final eccentricity distribution is an excellent indicator of the birth distribution regardless of other initial conditions. Lastly, perturbations from the third body may drive the inner binary eccentricity extreme values, causing it to merge (e.g. Hoang et al., 2018; Rose et al., 2019). My work predicts many such mergers.

Rose et al. (2019) demonstrate how initial conditions inform the final property distributions of stellar binaries, assuming all of the binaries actually reside in triples. However, other dynamical processes complicate the physical picture in the GN. In this dense environment, a binary frequently interacts with neighboring objects. Systems that are more loosely bound than the average kinetic energy of their surroundings, or soft binaries, widen over time due to weak interactions with passing objects until they eventually unbind (e.g., Heggie, 1975). The associated timescale to unbind the binary is called the evaporation time (Binney & Tremaine, 2008). Additionally, a star in the binary can collide with a passing object, an occurrence that may also unbind the system (e.g., Sigurdsson & Phinney, 1993). The collision and evaporation timescales both depend on the density of the system's environment. Therefore, the detection of a soft binary with known properties can be used to constrain the density.

I illustrate this procedure in Rose et al. (2020). The age of the detected binary sets a lower limit on the evaporation and collision timescales of the system. A lower limit on the timescale leads to an upper limit on the density in the binary's vicinity: if the surroundings are too dense, the binary would have already unbound. Using this procedure, observed binaries in the GC can further our understanding of their environment. In particular, a binary can probe the number of dense stellar remnants in its vicinity, such as black holes (BHs), which are expected to concentrate in the central pc of the GN (e.g., Shapiro & Marchant, 1978; Morris, 1993; Miralda-Escudé & Gould, 2000). Using a similar method, I show that the reverse is also true: assumptions about the GN's density can be used to find the maximum orbital separation a binary can have at a given age.

Generally, the dynamical processes endemic to a GN mean that the binary population there dwindles over time, either because the SMBH's gravity drives them to merge or because interactions with surrounding objects pull them apart. As a result, single objects should dominate an older population. Dynamical processes will continue to shape the population of singles. In particular, collisions may explain the origins of some puzzling observational discoveries, such as a BH above ~ 50 $M_\odot$. Theoretical models suggest that such massive BHs cannot form from stellar evolution (e.g., Heger et al., 2003). In Rose et al. (2022), I explore BH growth through repeated collisions with stars using a semianalytic model. During each BH-star collision, a stellar-mass BH can accrete a small fraction of the star's mass, growing incrementally in size. Over many collisions, it can grow substantially in mass. I have shown that this channel can produce BHs above the maximum mass predicted by stellar evolution models from an initial population of stellar mass BHs. BH-star collisions therefore represent a promising mechanism to modify the BH mass distribution in a GN.

Lastly, just as collisions with stars can produce more massive BHs, collisions between main-sequence stars can create more massive stars. In Rose et al. (2023), I show that the outcome of a collision depends on the region in which a star resides. Within 0.01 pc of the SMBH, for example, collisions occur at high relative velocities and result in mass loss. We find that the stellar population within 0.01 pc is halved within about a Gyr because of destructive collisions. Additionally, we predict a diffuse population of peculiar low-mass stars in the GC. These stars have been divested of their outer layers in the inner 0.01 pc before migrating to larger distances from the SMBH. Between 0.01 and 0.1 pc, however, collisions result in stellar mergers. These merged stars may appear younger than the surrounding population, offering a possible explanation for the observation of young-seeming, massive stars close to the SMBH (e.g., Genzel et al., 2010). We estimate that there may be ~ 100 stars over 10 $M_\odot$ residing in this region that are produced through collisions between lower mass stars. We discuss possible connections between main-sequence stellar collisions and the population of G objects, or dust and gas enshrouded stellar objects, in the GC, as well as missing red

giants near the SMBH.

The proximity of the Milky Way's GN presents a unique opportunity to study the physical processes unfolding in the centers of galaxies. Under the influence of the SMBH's extreme gravity, the stellar, binary, and compact object populations in the nuclear star cluster differ from others in our galaxy. This thesis examines how three-body and cluster dynamics shapes these populations. The centers of galaxies are factories for extreme events such as stellar mergers, compact object mergers, and EMRIs. As electromagnetic and GW observational campaigns continue to yield rich observations of the GN, understanding the progenitor populations, their demographics and properties, and the forces shaping them becomes crucial.

Bibliography

Abbott B. P., et al., 2016, Phys. Rev. Lett., 116, 241102

Abbott B. P., et al., 2017a, Phys. Rev. Lett., 118, 221101

Abbott B. P., et al., 2017b, Phys. Rev. Lett., 119, 141101

Aharon D., Perets H. B., 2016, ApJ, 830, L1

Alexander T., 1999, ApJ, 527, 835

Alexander T., 2005, Phys. Rep., 419, 65

Alexander T., Hopman C., 2009, ApJ, 697, 1861

Alexander T., Pfuhl O., 2014, ApJ, 780, 148

Ali B., et al., 2020, ApJ, 896, 100

Almeida L. A., et al., 2017, A&A, 598, A84

Amaro-Seoane P., 2018, Living Reviews in Relativity, 21, 4

Amaro Seoane P., 2023, arXiv e-prints, p. arXiv:2302.00014

Amaro-Seoane P., Chen X., 2014, ApJ, 781, L18

Amaro-Seoane P., Preto M., 2011, Classical and Quantum Gravity, 28, 094017

Amaro-Seoane et al. 2017, arXiv e-prints, p. arXiv:1702.00786

Amaro-Seoane P., Chen X., Schödel R., Casanellas J., 2020, MNRAS, 492, 250

Antognini J. M. O., 2015, MNRAS, 452, 3610

Antonini F., 2014, ApJ, 794, 106

Antonini F., Perets H. B., 2012, ApJ, 757, 27

Antonini F., Faber J., Gualandris A., Merritt D., 2010, ApJ, 713, 90

Antonini F., Lombardi James C. J., Merritt D., 2011, ApJ, 731, 128

Antonini F., Murray N., Mikkola S., 2014, ApJ, 781, 45

Arca Sedda M., 2020, ApJ, 891, 47

Arca Sedda M., Mapelli M., Benacquista M., Spera M., 2023, MNRAS, 520, 5259

Armitage P. J., 2007, preprint, pp astro–ph/0701485 (arXiv:astro-ph/0701485)

Bahcall J. N., Wolf R. A., 1976, ApJ, 209, 214

Baibhav V., Gerosa D., Berti E., Wong K. W. K., Helfer T., Mould M., 2020, Phys. Rev. D, 102, 043002

Bailey V. C., Davies M. B., 1999, MNRAS, 308, 257

Baker et al. 2019, arXiv e-prints, p. arXiv:1907.06482

Balberg S., Sari R., Loeb A., 2013, MNRAS, 434, L26

Bar-Or B., Fouvry J.-B., 2018, ApJ, 860, L23

Bar-Or B., Kupi G., Alexander T., 2013, ApJ, 764, 52

Bartko H., et al., 2009, ApJ, 697, 1741

Bartko H., et al., 2010, ApJ, 708, 834

Bataille M., Libert A.-S., Correia A. C. M., 2018, MNRAS, 479, 4749

Baumgardt H., Makino J., Ebisuzaki T., 2004, ApJ, 613, 1143

Baumgardt H., Gualandris A., Portegies Zwart S., 2006a, MNRAS, 372, 174

Baumgardt H., Hopman C., Portegies Zwart S., Makino J., 2006b, MNRAS, 372, 467

Baumgardt H., Amaro-Seoane P., Schödel R., 2018, A&A, 609, A28

Begelman M. C., 1979, MNRAS, 187, 237

Begelman M. C., 2012a, MNRAS, 420, 2912

Begelman M. C., 2012b, ApJ, 749, L3

Begelman M. C., Volonteri M., Rees M. J., 2006, MNRAS, 370, 289

Belczynski K., et al., 2020, ApJ, 890, 113

Benz W., Hills J. G., 1987, ApJ, 323, 614

Bertone G., Fornasa M., Taoso M., Zentner A. R., 2009, New Journal of Physics, 11, 105016

Binney J., Tremaine S., 1987, Galactic dynamics

Binney J., Tremaine S., 2008, Galactic Dynamics: Second Edition

Blaes O., Lee M. H., Socrates A., 2002, ApJ, 578, 775

Blandford R. D., Begelman M. C., 1999, MNRAS, 303, L1

Blandford R. D., Znajek R. L., 1977, MNRAS, 179, 433

Blecha L., Ivanova N., Kalogera V., Belczynski K., Fregeau J., Rasio F., 2006, ApJ, 642, 427

Bondi H., 1952, MNRAS, 112, 195

Bondi H., Hoyle F., 1944, MNRAS, 104, 273

Bonnell I. A., Davies M. B., 1998, MNRAS, 295, 691

Bouvier J., 2013, in Hennebelle P., Charbonnel C., eds, EAS Publications Series Vol. 62, EAS Publications Series. pp 143–168 (arXiv:1307.2891), doi:10.1051/eas/1362005

Bradnick B., Mandel I., Levin Y., 2017, MNRAS, 469, 2042

Breivik K., et al., 2020, ApJ, 898, 71

Brennan R., Choi E., Somerville R. S., Hirschmann M., Naab T., Ostriker J. P., 2018, ApJ, 860, 14

Bringmann T., Huang X., Ibarra A., Vogl S., Weniger C., 2012, J. Cosmology Astropart. Phys., 2012, 054

Buchholz R. M., Schödel R., Eckart A., 2009, A&A, 499, 483

Burkert A., Schartmann M., Alig C., Gillessen S., Genzel R., Fritz T. K., Eisenhauer F., 2012, ApJ, 750, 58

Centrella J., Baker J. G., Kelly B. J., van Meter J. R., 2010, Reviews of Modern Physics, 82, 3069

Chen X., Han W.-B., 2018, Communications Physics, 1, 53

Chen X., Liu F. K., 2013, ApJ, 762, 95

Chen Z., et al., 2023, ApJ, 944, 79

Cheng Z., Li Z., Xu X., Li X., 2018, ApJ, 858, 33

Cheng Z., Mu H., Li Z., Xu X., Wang W., Li X., 2020, ApJ, 892, 16

Chernov S. V., 2017, Astronomy Letters, 43, 429

Choi J.-H., Shlosman I., Begelman M. C., 2015, MNRAS, 450, 4411

Christensen-Dalsgaard J., et al., 1996, Science, 272, 1286

Christopher M. H., Scoville N. Z., Stolovy S. R., Yun M. S., 2005, ApJ, 622, 346

Chu D. S., et al., 2018, ApJ, 854, 12

Ciurlo A., et al., 2020, Nature, 577, 337

Ciurlo A., et al., 2023, ApJ, 944, 136

Claret A., Cunha N. C. S., 1997, A&A, 318, 187

Cohn H., Kulsrud R. M., 1978, ApJ, 226, 1087

Dale J. E., Davies M. B., 2006, MNRAS, 366, 1424

Dale J. E., Davies M. B., Church R. P., Freitag M., 2009, MNRAS, 393, 1016

Dall'Amico M., Mapelli M., Di Carlo U. N., Bouffanais Y., Rastello S., Santoliquido F., Ballone A., Arca Sedda M., 2021, MNRAS, 508, 3045

Das A., Schleicher D. R. G., Leigh N. W. C., Boekholt T. C. N., 2021a, MNRAS, 503, 1051

Das A., Schleicher D. R. G., Basu S., Boekholt T. C. N., 2021b, MNRAS, 505, 2186

David L. P., Durisen R. H., Cohn H. N., 1987a, ApJ, 313, 556

David L. P., Durisen R. H., Cohn H. N., 1987b, ApJ, 316, 505

Davies M. B., King A., 2005, ApJ, 624, L25

Davies M. B., Blackwell R., Bailey V. C., Sigurdsson S., 1998, MNRAS, 301, 745

De Villiers J.-P., Hawley J. F., Krolik J. H., Hirose S., 2005, ApJ, 620, 878

Demircan O., Kahraman G., 1991, Ap&SS, 181, 313

Di Carlo U. N., Giacobbo N., Mapelli M., Pasquato M., Spera M., Wang L., Haardt F., 2019, MNRAS, 487, 2947

Di Carlo U. N., et al., 2021, MNRAS, 507, 5132

Do T., Ghez A. M., Morris M. R., Lu J. R., Matthews K., Yelda S., Larkin J., 2009, ApJ, 703, 1323

Do T., Lu J. R., Ghez A. M., Morris M. R., Yelda S., Martinez G. D., Wright S. A., Matthews K., 2013a, ApJ, 764, 154

Do T., et al., 2013b, ApJ, 779, L6

Do T., et al., 2019, Science, 365, 664

Dong H., et al., 2017a, MNRAS, 470, 3427

Dong H., et al., 2017b, MNRAS, 471, 3617

Duchêne G., Kraus A., 2013, ARA&A, 51, 269

Duncan M. J., Shapiro S. L., 1983, ApJ, 268, 565

Ebisuzaki T., et al., 2001, ApJ, 562, L19

Eda K., Itoh Y., Kuroyanagi S., Silk J., 2013, Phys. Rev. Lett., 110, 221101

Edgar R., 2004, New A Rev., 48, 843

Eggleton P. P., 1983, ApJ, 268, 368

Eggleton P. P., Kiseleva-Eggleton L., 2001, ApJ, 562, 1012

Eggleton P. P., Kiseleva L. G., Hut P., 1998, ApJ, 499, 853

Eggleton P. P., Kisseleva-Eggleton L., Dearborn X., 2007, in Hartkopf W. I., Harmanec P., Guinan E. F., eds, IAU Symposium Vol. 240, Binary Stars as Critical Tools Tests in Contemporary Astrophysics. pp 347–355, doi:10.1017/S1743921307004280

Escala A., 2021, ApJ, 908, 57

Fabrycky D., Tremaine S., 2007, ApJ, 669, 1298

Fabrycky D. C., Johnson E. T., Goodman J., 2007, ApJ, 665, 754

Feldmeier-Krause A., et al., 2015, A&A, 584, A2

Ferrara A., Salvadori S., Yue B., Schleicher D., 2014, Monthly Notices of the Royal Astronomical Society, 443, 2410

Ferrarese L., Ford H., 2005, Space Sci. Rev., 116, 523

Fishbach M., Farr W. M., Holz D. E., 2020, ApJ, 891, L31

Ford E. B., Rasio F. A., 2006, ApJ, 638, L45

Ford E. B., Kozinsky B., Rasio F. A., 2000, ApJ, 535, 385

Fragione G., 2018, MNRAS, 479, 2615

Fragione G., 2019, arXiv e-prints, p. arXiv:1903.03117

Fragione G., Antonini F., 2019, MNRAS, 488, 728

Fragione G., Gualandris A., 2018, MNRAS, 475, 4986

Fragione G., Loeb A., 2019, MNRAS, 486, 4443

Fragione G., Sari R., 2018, ApJ, 852, 51

Fragione G., Grishin E., Leigh N. W. C., Perets H. B., Perna R., 2018, arXiv e-prints, p. arXiv:1811.10627

Fragione G., Loeb A., Kremer K., Rasio F. A., 2020a, ApJ, 897, 46

Fragione G., Loeb A., Rasio F. A., 2020b, ApJ, 902, L26

Fragione G., Kocsis B., Rasio F. A., Silk J., 2021, arXiv e-prints, p. arXiv:2107.04639

Fregeau J. M., Rasio F. A., 2007, ApJ, 658, 1047

Fregeau J. M., Joshi K. J., Portegies Zwart S. F., Rasio F. A., 2002, ApJ, 570, 171

Fregeau J. M., Cheung P., Portegies Zwart S. F., Rasio F. A., 2004, MNRAS, 352, 1

Freitag M., Benz W., 2002, A&A, 394, 345

Freitag M., Benz W., 2005, MNRAS, 358, 1133

Freitag M., Amaro-Seoane P., Kalogera V., 2006, ApJ, 649, 91

GRAVITY Collaboration et al., 2020, A&A, 636, L5

Gallego-Cano E., Schödel R., Dong H., Nogueras-Lara F., Gallego-Calvente A. T., Amaro-Seoane P., Baumgardt H., 2018, A&A, 609, A26

Gallego-Cano E., Schödel R., Nogueras-Lara F., Dong H., Shahzamanian B., Fritz T. K., Gallego-Calvente A. T., Neumayer N., 2020, A&A, 634, A71

Gautam A. K., et al., 2019, ApJ, 871, 103

Geller A. M., de Grijs R., Li C., Hurley J. R., 2013, ApJ, 779, 30

Geller A. M., Leigh N. W. C., Giersz M., Kremer K., Rasio F. A., 2019, ApJ, 872, 165

Generozov A., Madigan A.-M., 2020, ApJ, 896, 137

Generozov A., Stone N. C., Metzger B. D., Ostriker J. P., 2018, MNRAS, 478, 4030

Genzel R., Thatte N., Krabbe A., Kroker H., Tacconi-Garman L. E., 1996, ApJ, 472, 153

Genzel R., et al., 2003, ApJ, 594, 812

Genzel R., Eisenhauer F., Gillessen S., 2010, Reviews of Modern Physics, 82, 3121

Gerhard O., 2001, ApJ, 546, L39

Ghez A. M., et al., 2003, ApJ, 586, L127

Ghez A. M., Salim S., Hornstein S. D., Tanner A., Lu J. R., Morris M., Becklin E. E., Duchêne G., 2005, ApJ, 620, 744

Ghez A. M., et al., 2008, ApJ, 689, 1044

Gieles M., Heggie D. C., Zhao H., 2011, MNRAS, 413, 2509

Gillessen S., Eisenhauer F., Trippe S., Alexand er T., Genzel R., Martins F., Ott T., 2009, ApJ, 692, 1075

Gillessen S., et al., 2017, ApJ, 837, 30

Ginsburg I., Loeb A., 2007, MNRAS, 376, 492

Gnedin O. Y., Ostriker J. P., Tremaine S., 2014, ApJ, 785, 71

Gondán L., Kocsis B., Raffai P., Frei Z., 2018, ApJ, 860, 5

González E., Kremer K., Chatterjee S., Fragione G., Rodriguez C. L., Weatherford N. C., Ye C. S., Rasio F. A., 2021, ApJ, 908, L29

Grellmann R., Preibisch T., Ratzka T., Kraus S., Helminiak K. G., Zinnecker H., 2013, A&A, 550, A82

Griffin R. F., 2012, Journal of Astrophysics and Astronomy, 33, 29

Gualandris A., Merritt D., 2009, ApJ, 705, 361

Gürkan M. A., Rasio F. A., 2005, ApJ, 628, 236

Gürkan M. A., Fregeau J. M., Rasio F. A., 2006, ApJ, 640, L39

Habibi M., et al., 2017, ApJ, 847, 120

Habibi M., et al., 2019, ApJ, 872, L15

Hailey C. J., Mori K., Bauer F. E., Berkowitz M. E., Hong J., Hord B. J., 2018, Nature, 556, 70

Hamers A. S., Samsing J., 2019, MNRAS, 487, 5630

Hamers A. S., Bar-Or B., Petrovich C., Antonini F., 2018, ApJ, 865, 2

Hansen B. M. S., Milosavljević M., 2003, ApJ, 593, L77

Harrington R. S., 1969, Celestial Mechanics, 1, 200

Heger A., Fryer C. L., Woosley S. E., Langer N., Hartmann D. H., 2003, ApJ, 591, 288

Heggie D. C., 1975, MNRAS, 173, 729

Heggie D. C., Hut P., 1993, ApJS, 85, 347

Heggie D. C., Rasio F. A., 1996, MNRAS, 282, 1064

Heinke C. O., Ruiter A. J., Muno M. P., Belczynski K., 2008, in Bandyopadhyay R. M., Wachter S., Gelino D., Gelino C. R., eds, American Institute of Physics Conference Series Vol. 1010, A Population Explosion: The Nature & Evolution of X-ray Binaries in Diverse Environments. pp 136–142 (arXiv:0801.1279), doi:10.1063/1.2945021

Hills J. G., 1975, AJ, 80, 809

Hills J. G., 1988, Nature, 331, 687

Hoang B.-M., Naoz S., Kocsis B., Rasio F. A., Dosopoulou F., 2018, ApJ, 856, 140

Hoang B.-M., Naoz S., Kocsis B., Farr W. M., McIver J., 2019, ApJ, 875, L31

Hoang B.-M., Naoz S., Kremer K., 2020, ApJ, 903, 8

Hopman C., 2009, ApJ, 700, 1933

Hopman C., Alexander T., 2005, ApJ, 629, 362

Hopman C., Alexander T., 2006a, ApJ, 645, 1152

Hopman C., Alexander T., 2006b, ApJ, 645, L133

Hosek Matthew W. J., Lu J. R., Anderson J., Najarro F., Ghez A. M., Morris M. R., Clarkson W. I., Albers S. M., 2019, ApJ, 870, 44

Hurley J. R., Tout C. A., Pols O. R., 2002, MNRAS, 329, 897

Igumenshchev I. V., 2008, ApJ, 677, 317

Igumenshchev I. V., Narayan R., Abramowicz M. A., 2003, ApJ, 592, 1042

Ivanova N., 2011, ApJ, 730, 76

Ivanova N., et al., 2013, A&A Rev., 21, 59

Jackson J. M., Geis N., Genzel R., Harris A. I., Madden S., Poglitsch A., Stacey G. J., Townes C. H., 1993, ApJ, 402, 173

Jiang Y.-F., Stone J. M., Davis S. W., 2014, ApJ, 796, 106

Johnson J. L., Bromm V., 2007, Monthly Notices of the Royal Astronomical Society, 374, 1557

Katz B., Dong S., 2012, arXiv e-prints, p. arXiv:1211.4584

Keshet U., Hopman C., Alexander T., 2009, ApJ, 698, L64

Kiseleva L. G., Eggleton P. P., Mikkola S., 1998, MNRAS, 300, 292

Kobulnicky H. A., et al., 2014, ApJS, 213, 34

Kocsis B., Tremaine S., 2011, MNRAS, 412, 187

Kormendy J., 2004, in Ho L. C., ed., Coevolution of Black Holes and Galaxies. p. 1 (arXiv:astro-ph/0306353)

Kormendy J., Ho L. C., 2013, ARA&A, 51, 511

Kozai Y., 1962, AJ, 67, 591

Kremer K., et al., 2020, ApJ, 903, 45

Kremer K., Lu W., Piro A. L., Chatterjee S., Rasio F. A., Ye C. S., 2021, ApJ, 911, 104

Kremer K., Lombardi J. C., Lu W., Piro A. L., Rasio F. A., 2022, ApJ, 933, 203

Kroupa P., Subr L., Jerabkova T., Wang L., 2020, MNRAS, 498, 5652

Lai D., Rasio F. A., Shapiro S. L., 1993, ApJ, 412, 593

Langer N., 2009, A&A, 500, 133

Leigh N. W. C., Antonini F., Stone N. C., Shara M. M., Merritt D., 2016, MNRAS, 463, 1605

Leigh N. W. C., et al., 2018, MNRAS, 474, 5672

Levin Y., Beloborodov A. M., 2003, ApJ, 590, L33

Li G., Ginsburg I., Naoz S., Loeb A., 2017, ApJ, 851, 131

Lidov M. L., 1962, planss, 9, 719

Limongi M., Chieffi A., 2018, ApJS, 237, 13

Linial I., Sari R., 2022, ApJ, 940, 101

Lithwick Y., Naoz S., 2011, ApJ, 742, 94

Löckmann U., Baumgardt H., 2008, MNRAS, 384, 323

Lombardi James C. J., Warren J. S., Rasio F. A., Sills A., Warren A. R., 2002, ApJ, 568, 939

Lu C. X., Naoz S., 2019, MNRAS, 484, 1506

Lu J. R., Ghez A. M., Hornstein S. D., Morris M. R., Becklin E. E., Matthews K., 2009, ApJ, 690, 1463

Lu J. R., Do T., Ghez A. M., Morris M. R., Yelda S., Matthews K., 2013, ApJ, 764, 155

Madau P., Rees M. J., 2001, ApJ, 551, L27

Madigan A.-M., McCourt M., O'Leary R. M., 2017, MNRAS, 465, 2310

Magorrian J., Tremaine S., 1999, MNRAS, 309, 447

Maillard J. P., Paumard T., Stolovy S. R., Rigaut F., 2004, A&A, 423, 155

Malkov O. Y., Tamazian V. S., Docobo J. A., Chulkov D. A., 2012, A&A, 546, A69

Mapelli M., Bouffanais Y., Santoliquido F., Arca Sedda M., Artale M. C., 2021a, arXiv e-prints, p. arXiv:2109.06222

Mapelli M., et al., 2021b, MNRAS, 505, 339

Mardling R. A., Aarseth S. J., 2001, MNRAS, 321, 398

Martin R. G., Nixon C., Lubow S. H., Armitage P. J., Price D. J., Doğan S., King A., 2014, ApJ, 792, L33

Martins F., et al., 2006, ApJ, 649, L103

Mastrobuono-Battisti A., Church R. P., Davies M. B., 2021, MNRAS, 505, 3314

Mathieu R. D., Latham D. W., 1986, AJ, 92, 1364

Mazeh T., Shaham J., 1979, A&A, 77, 145

McKinney J. C., 2006, MNRAS, 368, 1561

McKinney J. C., Gammie C. F., 2004, ApJ, 611, 977

McKinney J. C., Tchekhovskoy A., Sadowski A., Narayan R., 2014, MNRAS, 441, 3177

Mei et al. 2020, Progress of Theoretical and Experimental Physics, 2021

Merritt D., 2006, Reports on Progress in Physics, 69, 2513

Merritt D., 2010, ApJ, 718, 739

Michaely E., Perets H. B., 2014, ApJ, 794, 122

Michaely E., Perets H. B., 2019, ApJ, 887, L36

Miralda-Escudé J., Gould A., 2000, ApJ, 545, 847

Moe M., Di Stefano R., 2017, ApJS, 230, 15

Moe M., Kratter K. M., 2018, ApJ, 854, 44

Montero-Castaño M., Herrnstein R. M., Ho P. T. P., 2009, ApJ, 695, 1477

Morris M., 1993, ApJ, 408, 496

Muno M. P., Pfahl E., Baganoff F. K., Brandt W. N., Ghez A., Lu J., Morris M. R., 2005, ApJ, 622, L113

Muno M. P., Bauer F. E., Bandyopadhyay R. M., Wang Q. D., 2006, ApJS, 165, 173

Muno M. P., et al., 2009, ApJS, 181, 110

Murphy B. W., Cohn H. N., Durisen R. H., 1991, ApJ, 370, 60

Murray-Clay R. A., Loeb A., 2012, Nature Communications, 3, 1049

Murray N., Quataert E., Thompson T. A., 2005, ApJ, 618, 569

Mylläri A., Valtonen M., Pasechnik A., Mikkola S., 2018, MNRAS, 476, 830

Naoz S., 2016, ARA&A, 54, 441

Naoz S., Fabrycky D. C., 2014, preprint, (arXiv:1405.5223)

Naoz S., Silk J., 2014, ApJ, 795, 102

Naoz S., Farr W. M., Lithwick Y., Rasio F. A., Teyssandier J., 2013a, MNRAS, 431, 2155

Naoz S., Kocsis B., Loeb A., Yunes N., 2013b, ApJ, 773, 187

Naoz S., Fragos T., Geller A., Stephan A. P., Rasio F. A., 2016, ApJ, 822, L24

Naoz S., Ghez A. M., Hees A., Do T., Witzel G., Lu J. R., 2018, ApJ, 853, L24

Naoz S., Silk J., Schnittman J. D., 2019, ApJ, 885, L35

Naoz S., Will C. M., Ramirez-Ruiz E., Hees A., Ghez A. M., Do T., 2020, ApJ, 888, L8

Naoz S., Rose S. C., Michaely E., Melchor D., Ramirez-Ruiz E., Mockler B., Schnittman J. D., 2022, ApJ, 927, L18

Narayan R., Igumenshchev I. V., Abramowicz M. A., 2003, PASJ, 55, L69

Narayan R., Chael A., Chatterjee K., Ricarte A., Curd B., 2022, MNRAS, 511, 3795

Nogueras-Lara F., et al., 2019, Nature Astronomy, 4, 377

Nogueras-Lara F., Schödel R., Neumayer N., 2021, ApJ, 920, 97

O'Leary R. M., Rasio F. A., Fregeau J. M., Ivanova N., O'Shaughnessy R., 2006, ApJ, 637, 937

O'Leary R. M., Kocsis B., Loeb A., 2009, MNRAS, 395, 2127

Ohsuga K., Mori M., Nakamoto T., Mineshige S., 2005, ApJ, 628, 368

Ostriker J. P., Choi E., Ciotti L., Novak G. S., Proga D., 2010, ApJ, 722, 642

Ott T., Eckart A., Genzel R., 1999, ApJ, 523, 248

Owen J. E., Lin D. N. C., 2023, MNRAS, 519, 397

Park M.-G., Ostriker J. P., 2001, ApJ, 549, 100

Paumard T., et al., 2006, ApJ, 643, 1011

Pejcha O., Antognini J. M., Shappee B. J., Thompson T. A., 2013, MNRAS, 435, 943

Perets H. B., 2009a, ApJ, 690, 795

Perets H. B., 2009b, ApJ, 698, 1330

Perets H. B., Fabrycky D. C., 2009, ApJ, 697, 1048

Perets H. B., Hopman C., Alexander T., 2007, ApJ, 656, 709

Perets H. B., Li Z., Lombardi James C. J., Milcarek Stephen R. J., 2016, ApJ, 823, 113

Peters P. C., Mathews J., 1963, Physical Review, 131, 435

Pfuhl O., et al., 2011, ApJ, 741, 108

Pfuhl O., Alexander T., Gillessen S., Martins F., Genzel R., Eisenhauer F., Fritz T. K., Ott T., 2014, ApJ, 782, 101

Portegies Zwart S. F., McMillan S. L. W., 2000, ApJ, 528, L17

Portegies Zwart S. F., McMillan S. L. W., 2002, ApJ, 576, 899

Portegies Zwart S. F., Baumgardt H., Hut P., Makino J., McMillan S. L. W., 2004, Nature, 428, 724

Preibisch T., Weigelt G., Zinnecker H., 2001, in Zinnecker H., Mathieu R., eds, IAU Symposium Vol. 200, The Formation of Binary Stars. p. 69 (arXiv:astro-ph/0008014)

Preto M., Amaro-Seoane P., 2010, ApJ, 708, L42

Pribulla T., Rucinski S. M., 2006, AJ, 131, 2986

Prodan S., Antonini F., Perets H. B., 2015, ApJ, 799, 118

Rafelski M., Ghez A. M., Hornstein S. D., Lu J. R., Morris M., 2007, ApJ, 659, 1241

Raghavan D., et al., 2010, ApJS, 190, 1

Rashkov V., Madau P., 2014, ApJ, 780, 187

Rasio F. A., Heggie D. C., 1995, ApJ, 445, L133

Rauch K. P., 1999, ApJ, 514, 725

Rauch K. P., Tremaine S., 1996, New A, 1, 149

Rees M. J., 1988, Nature, 333, 523

Renzo M., Farmer R., Justham S., Götberg Y., de Mink S. E., Zapartas E., Marchant P., Smith N., 2020, A&A, 640, A56

Rizzuto F. P., Naab T., Spurzem R., Arca-Sedda M., Giersz M., Ostriker J. P., Banerjee S., 2022, MNRAS,

Robson T., Cornish N. J., Liu C., 2019, Classical and Quantum Gravity, 36, 105011

Rodriguez C. L., Chatterjee S., Rasio F. A., 2016, Phys. Rev. D, 93, 084029

Rodriguez C. L., Amaro-Seoane P., Chatterjee S., Rasio F. A., 2018, Phys. Rev. Lett., 120, 151101

Rodriguez C. L., Zevin M., Amaro-Seoane P., Chatterjee S., Kremer K., Rasio F. A., Ye C. S., 2019, Phys. Rev. D, 100, 043027

Rodriguez C. L., et al., 2022, ApJS, 258, 22

Rose S. C., Naoz S., Geller A. M., 2019, MNRAS, 488, 2480

Rose S. C., Naoz S., Gautam A. K., Ghez A. M., Do T., Chu D., Becklin E., 2020, ApJ, 904, 113

Rose S. C., Naoz S., Sari R., Linial I., 2022, ApJ, 929, L22

Rose S. C., Naoz S., Sari R., Linial I., 2023, arXiv e-prints, p. arXiv:2304.10569

Rubin D., Loeb A., 2011, Advances in Astronomy, 2011, 174105

Ruge J. P., Wolf S., Uribe A. L., Klahr H. H., 2013, A&A, 549, A97

Sakstein J., Croon D., McDermott S. D., Straight M. C., Baxter E. J., 2020, Phys. Rev. Lett., 125, 261105

Sakurai Y., Yoshida N., Fujii M. S., Hirano S., 2017, MNRAS, 472, 1677

Samsing J., Venumadhav T., Dai L., Martinez I., Batta A., Lopez M., Ramirez-Ruiz E., Kremer K., 2019, Phys. Rev. D, 100, 043009

Sana H., Evans C. J., 2011, in Neiner C., Wade G., Meynet G., Peters G., eds, IAU Symposium Vol. 272, Active OB Stars: Structure, Evolution, Mass Loss, and Critical Limits. pp 474–485 (arXiv:1009.4197), doi:10.1017/S1743921311011124

Sana H., et al., 2012, Science, 337, 444

Sana H., et al., 2013, A&A, 550, A107

Sana H., Ramírez-Tannus M. C., de Koter A., Kaper L., Tramper F., Bik A., 2017, A&A, 599, L9

Sari R., Fragione G., 2019, ApJ, 885, 24

Schartmann M., Burkert A., Alig C., Gillessen S., Genzel R., Eisenhauer F., Fritz T. K., 2012, ApJ, 755, 155

Schneider R., Ferrara A., Natarajan P., Omukai K., 2002, The Astrophysical Journal, 571, 30

Schnittman J. D., Buonanno A., 2007, ApJ, 662, L63

Schödel R., Genzel R., Ott T., Eckart A., 2003, Astronomische Nachrichten Supplement, 324, 535

Schödel R., Najarro F., Muzic K., Eckart A., 2010, A&A, 511, A18

Schödel R., Feldmeier A., Kunneriath D., Stolovy S., Neumayer N., Amaro-Seoane P., Nishiyama S., 2014, A&A, 566, A47

Schödel R., Gallego-Cano E., Dong H., Nogueras-Lara F., Gallego-Calvente A. T., Amaro-Seoane P., Baumgardt H., 2018, A&A, 609, A27

Schödel R., Nogueras-Lara F., Gallego-Cano E., Shahzamanian B., Gallego-Calvente A. T., Gardini A., 2020, A&A, 641, A102

Shapiro S. L., Marchant A. B., 1978, ApJ, 225, 603

Shappee B. J., Thompson T. A., 2013, ApJ, 766, 64

Shima E., Matsuda T., Takeda H., Sawada K., 1985, MNRAS, 217, 367

Shlosman I., Choi J.-H., Begelman M. C., Nagamine K., 2016, MNRAS, 456, 500

Sigurdsson S., Phinney E. S., 1993, ApJ, 415, 631

Sills A., Lombardi James C. J., Bailyn C. D., Demarque P., Rasio F. A., Shapiro S. L., 1997, ApJ, 487, 290

Sills A., Faber J. A., Lombardi James C. J., Rasio F. A., Warren A. R., 2001, ApJ, 548, 323

Spera M., Mapelli M., 2017, MNRAS, 470, 4739

Spitzer L., 1987, Dynamical evolution of globular clusters

Stephan A. P., Naoz S., Ghez A. M., Witzel G., Sitarski B. N., Do T., Kocsis B., 2016, MNRAS, 460, 3494

Stephan A. P., et al., 2019, ApJ, 878, 58

Stone N. C., Metzger B. D., 2016, MNRAS, 455, 859

Stone N. C., Küpper A. H. W., Ostriker J. P., 2017, MNRAS, 467, 4180

The LIGO Scientific Collaboration et al., 2020a, Phys. Rev. Lett., 125, 101102

The LIGO Scientific Collaboration et al., 2020b, ApJ, 900, L13

Thompson T. A., 2011, ApJ, 741, 82

Tokovinin A. A., 1997, Astronomy Letters, 23, 727

Tokovinin A., 2008, MNRAS, 389, 925

Toonen S., Perets H. B., Igoshev A. P., Michaely E., Zenati Y., 2018, A&A, 619, A53

Torricelli-Ciamponi G., Foellmi C., Courvoisier T. J. L., Paltani S., 2000, A&A, 358, 57

Tremaine S., et al., 2002, ApJ, 574, 740

Umbreit S., Fregeau J. M., Chatterjee S., Rasio F. A., 2012, ApJ, 750, 31

Valiante R., Schneider R., Volonteri M., Omukai K., 2016, Monthly Notices of the Royal Astronomical Society, 457, 3356

Vink J. S., Higgins E. R., Sander A. A. C., Sabhahit G. N., 2021, MNRAS, 504, 146

Wang J., Merritt D., 2004, ApJ, 600, 149

Wang H., Stephan A. P., Naoz S., Hoang B.-M., Breivik K., 2021, ApJ, 917, 76

Witzel G., et al., 2014, ApJ, 796, L8

Witzel G., et al., 2017, ApJ, 847, 80

Woosley S. E., 2017, ApJ, 836, 244

Yelda S., Ghez A. M., Lu J. R., Do T., Meyer L., Morris M. R., Matthews K., 2014, ApJ, 783, 131

Yoon S.-C., Woosley S. E., Langer N., 2010, ApJ, 725, 940

Young S., Hamers A. S., 2020, arXiv e-prints, p. arXiv:2006.15023

Yu Q., Tremaine S., 2002, MNRAS, 335, 965

Yu Q., Tremaine S., 2003, ApJ, 599, 1129

Yuan F., Wu M., Bu D., 2012, ApJ, 761, 129

Yue B., Ferrara A., Salvaterra R., Xu Y., Chen X., 2014, Monthly Notices of the Royal Astronomical Society, 440, 1263

Zahn J.-P., 1977, A&A, 57, 383

Zajaček M., et al., 2017, A&A, 602, A121

Zajaček M., Araudo A., Karas V., Czerny B., Eckart A., 2020, ApJ, 903, 140

Zheng X., Lin D. N. C., Mao S., 2020, arXiv e-prints, p. arXiv:2011.04653

Zhu Z., Li Z., Morris M. R., 2018, ApJS, 235, 26

Zinnecker H., Yorke H. W., 2007, ARA&A, 45, 481

de Grijs R., Li C., Zheng Y., Deng L., Hu Y., Kouwenhoven M. B. N., Wicker J. E., 2013, ApJ, 765, 4

von Fellenberg S. D., et al., 2022, ApJ, 932, L6